LA-12942-MS

UC-700 and UC-703
Issued: June 1995

Comparison of Chemical and Nuclear Explosions: Numerical Simulations of the Non-Proliferation Experiment

James R. Kamm
Randy J. Bos

Los Alamos
NATIONAL LABORATORY
Los Alamos, New Mexico 87545

DISCLAIMER

Portions of this document may be illegible in electronic image products. Images are produced from the best available original document.

Contents

List of Figures

List of Tables

COMPARISON OF CHEMICAL AND NUCLEAR EXPLOSIONS: NUMERICAL SIMULATIONS OF THE NON-PROLIFERATION EXPERIMENT

by

James R. Kamm and Randy J. Bos

ABSTRACT

In this paper we discuss numerical simulations of the Non-Proliferation Experiment (NPE), which was an underground explosion conducted in September 1993 in the volcanic tuff of the Nevada Test Site. The NPE source consisted of 1.29×10^6 kg of ANFO-emulsion blasting agent, with the approximate energy of 1.1 kt, emplaced 389 m beneath the surface of Rainier Mesa. We compare detailed numerical simulations of the NPE with data collected from that experiment, and with calculations of an equally energetic nuclear explosion in identical geology. Calculated waveforms, at ranges out to approximately 1 km, agree moderately well in the time domain with free-field data, and are in qualitative agreement with free-surface records. Comparison of computed waveforms for equally energetic chemical and nuclear sources reveals relatively minor differences beyond the immediate near-source region, with the chemical source having an ~25% greater seismic moment but otherwise indistinguishable (close-in) seismic source properties.

1 Introduction

In this paper we discuss numerical simulations of buried, tamped chemical and nuclear explosions. Specifically, we consider simulations of the Non-Proliferation Experiment (NPE), in which 1.29×10^6 kg of ANFO-emulsion blasting agent, with the approximate energy of 1.1 kt, was detonated at a nominal depth of 389 m. This experiment, performed in the volcanic tuff of N-Tunnel in Area 12 of the Nevada Test Site in September 1993, was conducted with the intention of quantifying the effects of an *in situ* chemical explosion of magnitude comparable to that of nuclear explosions. Denny [1] provides a comprehensive review of all aspects of this unique and well-instrumented experiment.

The purpose of the present investigation is to compare detailed numerical simulations of the NPE with data collected from the experiment, and with comparable calculations of an equally energetic nuclear explosion in identical media. Specifically, we seek to determine what, if any, differences are present in the computed signatures of these explosions.

Calculated waveforms for the NPE source are found to agree reasonably well in the time domain with experimental free-field data at ranges out to $\sim$1 km; free-surface vertical velocity waveforms agree moderately well at surface ground zero (SGZ) and are in approximate qualitative agreement at greater ranges. Comparison of computed waveforms for the equally energetic chemical and nuclear sources reveals only minor differences; primarily, the peak waveform amplitudes for the chemical source are slightly greater than those of the nuclear source. Computed close-in seismic source functions show that the chemical source has an approximately 25% greater seismic moment but otherwise indistinguishable properties. These calculational results suggest that equally energetic nuclear and chemical (specifically, ANFO) sources are essentially identical up to a multiplicative factor of 1.25 in effective yield at scaled ranges up to $\sim$1 km/kt$^{1/3}$. This chemical-nuclear equivalency factor is somewhat smaller than the value of 1.5 suggested by Rimer *et al.* [2], who performed a series of 1-D simulations of the NPE; our result, however, falls between the value of unity obtained by Killian *et al.* [3] from a series of 1-D calculations in various media, and the widely espoused value of two, forwarded, e.g., by Burton *et al.* [4], who base their conclusions on numerical simulations of cratering in shale. We also compare computed results of the chemical source in both layered and uniform geologies. For these calculations, computed close-in seismic source function properties are very similar, with the exception of the RVP spectrum overshoot, which is significantly greater in the layered case.

This report is structured as follows. In Section 2, we provide details of the modeling assumptions made in the numerical simulations of the NPE and comparable nuclear explosion. The results of the calculations and the comparisons with experimental data are presented in Section 3, which also contains a discussion of the chemical-nuclear equivalency issue. We conclude in Section 4 with a summary of our findings.

2 Numerical Simulation of the NPE

The numerical simulation of the NPE was performed with the Los Alamos National Laboratory SMC-123 code [5]. SMC-123 is a one-, two-, or three-dimensional, Lagrangian, multimaterial stress-wave propagation code that is designed to simulate the response of porous geologic materials to impulsive energy releases. In the present study, two-dimensional, cylindrically symmetric calculations of the explosions were performed. In this section we discuss the models of the local geology, the rock material response, and the chemical and nuclear sources that were used in the numerical simulations.

Shown in Figure 1 is a tunnel-level map of the NPE area. As indicated in this diagram, the NPE was located close to three previous nuclear events: MISTY ECHO (ME), MINERAL QUARRY (MQ), and HUNTERS TROPHY (HT). The model of the local stratigraphy was inferred from the geologic cross section analysis compiled by Raytheon Services Nevada (RSN) and the Defense Nuclear Agency (DNA) [6] specifically for the NPE; the information contained in that study is based largely on data from vertical drill hole UE12n#14 (located ~300 m south of the NPE working point [WP]), vertical drill hole UE12n#1 (located ~260 m west of the NPE WP), and horizontal core hole UE12n.23 UG-1 (which passes within ~20 m of the NPE WP). Although there is dip present in the local rock strata, for modeling purposes we assume that the materials are layered exactly horizontally. Figure 2 shows the "best guess" stratigraphic model used in two-dimensional, cylindrically symmetric NPE simulation.

Previous numerical simulations of the aforementioned nuclear events [7] led to the development of material response models for the rock in the vicinity of the NPE, all of which are volcanic tuffs (with the exception of the Paleozoic basement). The material in the vicinity of the blasting agent is porous, well-saturated, zeolitized tuff. Table 1 contains the values ascribed to the material properties of the media in the various layers near the NPE. There is significant uncertainty in many of these values, given the scatter in the measured and computed quantities from which they were inferred.

The corresponding mechanical properties of the materials used in the calculations are provided in Table 2. The numerical simulations were performed using an elastic-plastic description of the geologic materials in which the material response is assumed elastic (with prescribed constant Poisson's ratio ν) up to the yield point, beyond which the standard Prandtl-Reuss plastic flow assumption applies. The flow stress Y (i.e., the maximum deviatoric stress difference at yielding) is assumed to obey an exponential pressure-induced reduction according to the following relation:

$$Y = Y_0 - Y_1 \exp\left(-P/Y_2\right) , \tag{1}$$

where Y_0, Y_1, and Y_2 all have the units of stress, and P is the mean stress. The shear strength of the near-source material is assumed to decrease with

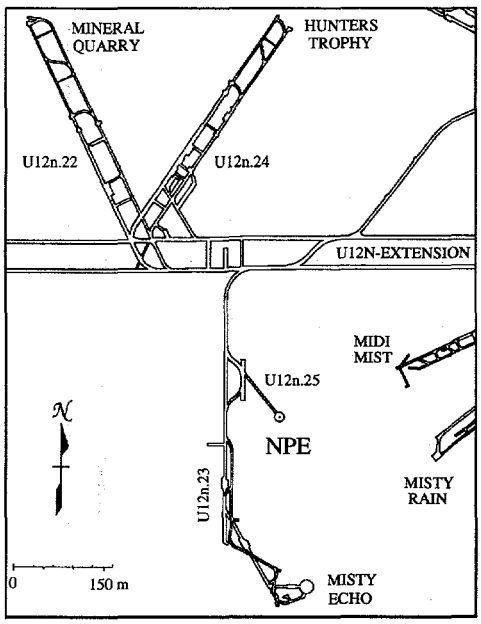

Figure 1: Map of NTS Area 12 in the vicinity of the NPE. The NPE was sited approximately 250 m from the location of MISTY ECHO, approximately 600 m from the location of HUNTERS TROPHY, and approximately 700 m from the location of MINERAL QUARRY.

accumulated inelastic shear strain; specifically, a damaged flow stress Y_D is defined as

$$Y_D = Y_0 - Y_{1,D} \exp\left(-P/Y_{2,D}\right) . \tag{2}$$

The value of the flow stress Y_{up} used to update the stress deviators is taken as the value that is linearly interpolated between Y and Y_D as a function of accumulated inelastic shear strain between prescribed minimum and maximum values, i.e.,

$$Y_{up} = Y - (Y - Y_D) \cdot \min\left\{1, \max\left\{0, \frac{\varepsilon_p - \varepsilon_{min}}{\varepsilon_{min} - \varepsilon_{min}}\right\}\right\} . \tag{3}$$

In this expression, the inelastic shear strain ε_p is updated for each zone at each time step as

$$\varepsilon_p^{n+1} = \varepsilon_p^n + \frac{1}{2\mu} |J_{2,old}^{n+1} - J_{2,new}^{n+1}| , \tag{4}$$

where J_2 denotes the second invariant of the deviatoric stress tensor, and the subscripts *old* and *new* indicate the values before and after returning the stress

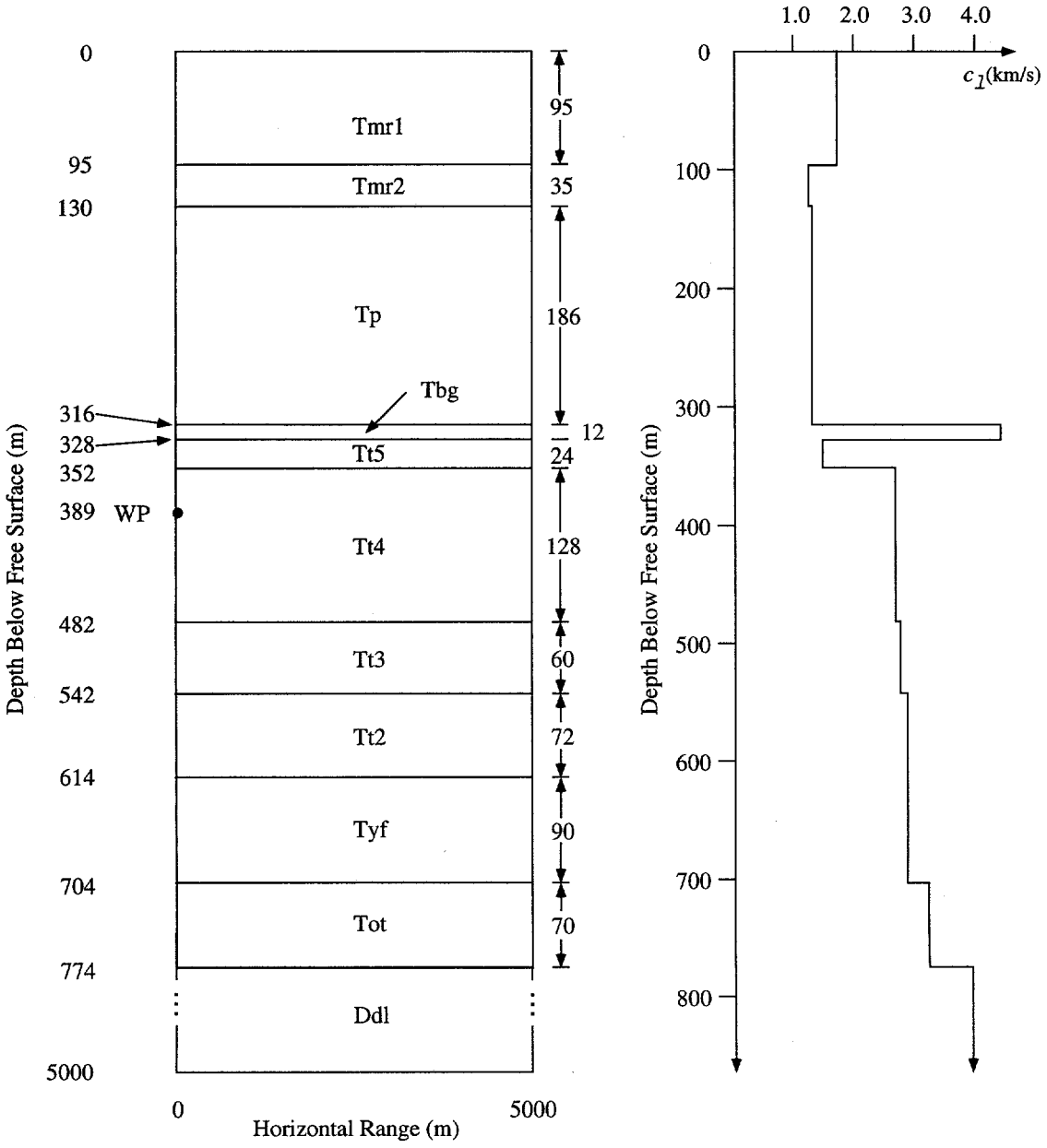

Figure 2: Layering model for the NPE simulations. Depicted are the stratigraphic model (left) and velocity profile (right) used in the two-dimensional, cylindrically symmetric NPE simulations. The material properties ascribed to the media in the various layers are catalogued in Tables 1 and 2. In this figure, distances are in m and velocities are in km/s. There are notable impedance mismatches around the thin Tbg layer, and at the zeolitization boundary between the Tt4 and Tt5 units.

Selected Rock Properties Used in the NPE Simulations

Depth (m)	*Material*	ρ_B (kg/m^3)	ρ_G (kg/m^3)	W	S	ϕ	ψ
0–95	Tmr1	2360	2520	0.04	0.94	0.10	6.6×10^{-3}
95–130	Tmr2	1700	2410	0.27	0.94	0.48	0.029
130–316	Tp	1700	2410	0.27	0.94	0.48	0.029
316–328	Tbg	2190	2480	0.07	0.86	0.18	0.025
328–352	Tt5	1700	2370	0.29	0.98	0.49	9.8×10^{-3}
352–482	Tt4	1970	2510	0.18	0.98	0.35	6.6×10^{-3}
482–542	Tt3	1850	2450	0.22	0.97	0.41	0.011
542–614	Tt2	1810	2390	0.22	0.97	0.41	0.011
614–704	Tyf	1850	2450	0.21	0.98	0.41	9.1×10^{-3}
704–774	Tot	1850	2450	0.22	1.00	0.41	0.0
774→	Ddl	2780	2800	4.0×10^{-3}	1.00	1.1×10^{-2}	0.0

Table 1: Listed are the material depth below the free surface, the material, the bulk density (ρ_B), the grain density (ρ_G), the weight-fraction of water (W), the saturation (S), the total porosity (ϕ), and the gas-filled porosity (ψ) for the materials used in the NPE simulations. These values are based on RSN/DNA data [6] and values used in numerical simulations of the HEARTS [8] and MISTY ECHO [7] events.

state to the yield surface (if required). The values of the mechanical properties used in the specification of the materials used in the simulations are also catalogued in Table 2.

The initial values of these properties were based on the aforementioned calculations and RSN and DNA data [6]. Comparison of the waveforms computed with these values with the close-in velocity and stress data, however, led to modification of the initial material properties to those tabulated above; we make no claim that the *ad hoc* iterative process by which these values were obtained led us to a description of the material response that is unique (much less optimal) within model constraints. The values we chose for the longitudinal elastic wave speed (c_ℓ) and the Poisson's ratio (ν) of the working point material, which is the best characterized of all units in the calculation, differ from those obtained in the laboratory by RSN; we attribute this discrepancy, as well as the other material property modifications, to inhomogeneities in the *in situ* rock masses as well as to the limitations imposed by the computational material models. Table 2 contains three notable impedance mismatches above the working point: (1) the boundary between the zeolitized (Tt4 and below) and vitric tuffs (Tt5 and above), across which the ascribed differences may well be unphysically large,[1] (2) on either side of the stiff albeit thin Tbg layer, and (3) between the upper (densely welded) part of the Tmr layer and the lower (partially welded) portion.

[1]Rimer *et al.* [2] ascribe somewhat different values to the WP tuff properties in their numerical simulations, which were conducted *before* the actual NPE shot.

Selected Mechanical Properties Used in the NPE Simulations

Material	ρ_B (kg/m^3)	ν	c_ℓ (km/s)	Y_0 (GPa)	Y_1 (GPa)	Y_2 (GPa)	$Y_{1,D}$ (GPa)	$Y_{2,D}$ (GPa)
Tmr1	2360	0.30	1.73	0.10	0.076	0.110	–	–
Tmr2	1700	0.30	1.25	0.02	0.014	0.048	–	–
Tp	1700	0.30	1.33	0.02	0.014	0.048	–	–
Tbg	2190	0.30	4.52	0.025	0.016	0.042	–	–
Tt5	1700	0.30	1.51	0.09	0.080	0.350	0.09	1.40
Tt4	1970	0.30	2.73	0.09	0.080	0.350	0.09	1.40
Tt3	1850	0.30	2.80	0.09	0.080	0.350	0.09	1.40
Tt2	1810	0.30	2.90	0.09	0.080	0.350	0.09	1.40
Tyf	1850	0.33	2.90	0.10	0.090	0.350	0.10	1.40
Tot	1850	0.33	3.27	0.10	0.090	0.350	0.10	1.40
Ddl	2780	0.33	4.00	0.16	0.160	0.560	0.16	1.18

Table 2: Listed are the material, the bulk density (ρ_B), Poisson's ratio (ν), the longitudinal elastic wave speed (c_ℓ), the maximum stress difference supported by the material (i.e., the flow stress) (Y_0), the flow stress decrement (Y_1), the pressure-softening exponent (Y_2), and the flow stress decrement ($Y_{1,D}$) and pressure-softening exponent ($Y_{2,D}$) for the yield surface of the fully damaged material. There is a notable change in material properties between the zeolitized and vitric tuffs, which we locate at the interface between the Tt4 and Tt5 units. A simple damage model is incorporated into the simulated material behavior, with shear failure governed by a value of the flow stress interpolated between the yield surface of the undamaged and damaged material as a linear function of the accumulated inelastic shear strain (see Eqs. 1–4 in the text).

In addition to the mechanical properties of these materials, equation of state models are required. The equation of state data for the rock material are divided into two regimes: (i) at pressures below 10 GPa, the Butkovich model [9] was used to provide the pressure-volume response of the porous, water-bearing material, while (ii) for pressures above 10 GPa, a Sesame table [10] for tuff was used (Sesame material 71243). (Sesame tables are EOS data available for a wide range of materials; often, these data are more accurate at higher pressures.) The Butkovich model is an analytic representation for the volumetric response of a mixture of rock, water, and gas based upon comparison with experimental data; the input data prescribed are the grain density, the bulk density, the mass-fraction of water, and two elastic constants. These low-pressure response curves for the materials used in these simulations is shown in Figure 3. In these simulations there is no modeling of the interaction between the shear response (described by Eqs. 1–4 with the Prandtl-Reuss flow rule) and the volumetric response (given the P-μ curves of Fig. 3). Preliminary calculations with an effective stress treatment for the working point material suggest that the physics afforded by that model, which includes shear-volume coupling, captures some

elements of the near-in waveforms lacking in the present total-stress model results.

The blasting agent used in the NPE is described by Souers *et al.* [11]. The equation of state of this ANFO-emulsion mixture in the calculations is based on the JWL approximation [12] using a programmed burn model for detonation. The JWL EOS prescribes the pressure of the detonation products as a function of the nondimensional specific volume V ($\equiv v/v_0$, v = specific volume) and specific internal energy E of the chemical explosive as

$$P(V,E) = A\left(1-\frac{\omega}{R_1V}\right)\exp(-R_1V) + B\left(1-\frac{\omega}{R_2V}\right)\exp(-R_2V) + \frac{\omega E}{V}. \tag{5}$$

The three addends in this expression characterize, respectively, the highly compressed, moderately compressed to moderately expanded, and greatly expanded states of the material. The values of the parameters in this expression for the ANFO-emulsion mixture used in the experiment were determined experimentally [11, 13]. Post-shot examination of the CORRTEX data collected within the blasting agent [14] suggests that density stratification of the ANFO-emulsion mixture had occurred between emplacement and detonation,[2] as discussed by Souers *et al.* [11] and McKown [14], which may have induced to nonideal behavior of the blasting agent. We follow the inferences of these researchers and model the blasting agent as consisting of three layers, each of which has different JWL coefficients; these values, as well as the corresponding detonation velocities, the initial energy densities, and C-J parameters are given in Table 3.

In the actual experiment, the ANFO mixture was emplaced in a cylindrical cavity of nominal height 5.2 m and diameter 15.2 m, corresponding to an approximate volume of 940 m^3; the center of the cavity, i.e., the NPE working point, was located 389 m below the free-surface and 1853 m above mean sea level [6]. In the calculation the blasting agent chamber was assigned the height of 5.2 m and radius 7.6 m for a volume of 944 m^3, which provided a computational yield of 1.05 kt. Following the experimental configuration [14], in the calculation the blasting agent was initiated at three points along the axis of symmetry of the initially cylindrical charge; the numerical simulation used a programmed burn model in which the detonation proceeded according to the detonation velocities given in Table 3. In the simulation of the comparable nuclear explosion, the total yield energy is deposited at initial time into a spherical volume of working point material corresponding to the mass that would be vaporized by a device of the prescribed yield; with the assumption that 70 Mg of material is vaporized per kt of device energy [15], the initial 1.05 kt source is assigned to a vaporization radius of 2 m.

The size of the initial radial and axial computational zones in the neighbor-

[2]Two possible causes of the density stratification have been suggested: (1) gravitational settling of the blasting agent, and (2) entrainment of air into the upper level of the blasting agent, which was augered in the chamber.

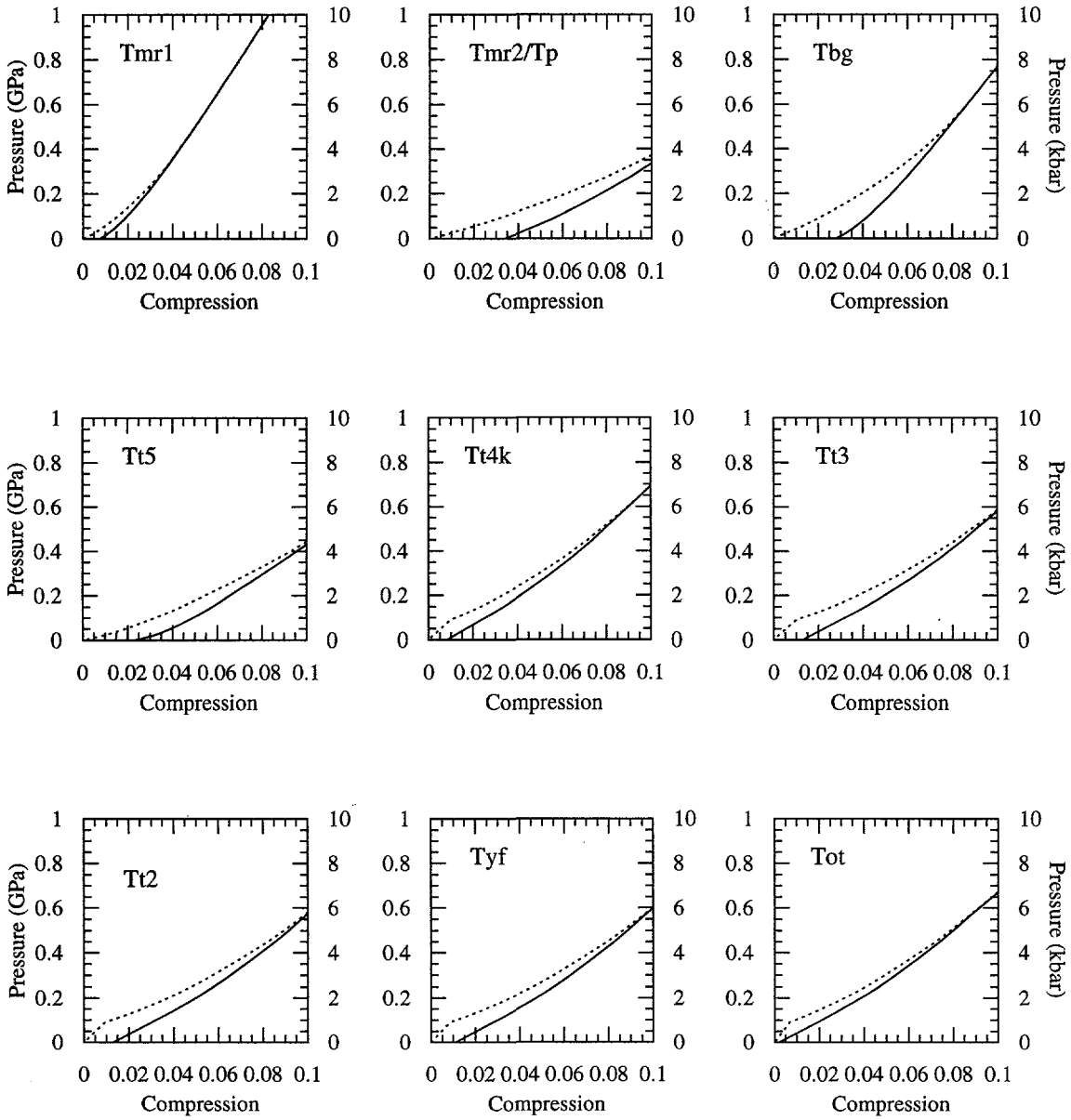

Figure 3: Pressure-volume relationship for NPE geologic materials. Shown are the pressure (GPa) vs. compression ($\mu \equiv (\rho/\rho_0) - 1$) curves for the various geologic materials used in the two-dimensional, cylindrically symmetric NPE simulations. The upper curve in each plot depicts the crush-up response of the virgin material, while the lower curve gives the behavior of the completely crushed rock.

JWL Parameters of the NPE Blasting Agent

Property	*Lower*	*Middle*	*Upper*
$z_{\min}$ (m)	-391.6	-389.9	-388.1
$z_{\max}$ (m)	-389.9	-388.1	-386.4
ρ_0 (Mg/m^3)	1.384	1.308	1.219
A (GPa)	407.1	407.1	407.1
B (GPa)	5.625	5.625	5.625
ω	0.450	0.450	0.450
R_1	4.463	4.722	5.067
R_2	1.001	1.060	1.137
D (m/s)	7.160×10^3	6.850×10^3	6.460×10^3
E_0 (J/kg)	3.561×10^6	3.561×10^6	3.561×10^6
$\gamma_{\rm CJ}$	3.043	3.043	3.043
$P_{\rm CJ}$ (GPa)	17.55	15.18	12.58
$V_{\rm CJ}$ (m^3/kg)	0.535×10^{-3}	0.570×10^{-3}	0.617×10^{-3}

Table 3: Listed above are the layer location ($z_{\min}$, $z_{\max}$), the initial density ρ_0, the JWL coefficients (see Eq. 5), the detonation velocity (D), the initial internal energy (E_0), the ratio of specific heats at the CJ point (γ_{CJ}), the pressure at the CJ point (P_{CJ}), and the volume at the CJ point (V_{CJ}) for each of the assumed layers of the blasting agent used in NPE simulations [11, 13].

hood of the source was set to the value of $\Delta r = \Delta z = 0.1$ m for the first few ms of the calculation. The solution was subsequently remapped onto progressively larger grids with bigger zones as the calculation progressed; at the latest times of the calculation, the nominal zone size within ~400 m (axially or radially) of the working point was 5 m, which increased geometrically (at a 1% rate) to a maximum of ~40 m at the grid boundary, located at a depth and range of ~5 km. The final mesh admitted 2 s of simulated ground motion at ranges of over 1 km from the source.

The initial stress state for the material was assigned in compliance with the Poisson effect and with no overburden-induced compression. Due to the presence of the cavity, the initial stress state was not an exact equilibrium solution; however, the outgoing pulse from the blasting agent quickly overtakes and dominates the elastic stress wave emanating from the cavity edge.

3 Results of the NPE Simulations

In this section, we compare experimental data with results of the chemical explosive (CE) and analogous nuclear explosive (NE) simulations. We also examine other characteristics of the computations, and draw some general inferences on the relationship between chemical and nuclear explosions.

As previously mentioned, the NPE was a very well instrumented experiment. Table 4 is a list of the near-shot-point gage locations at which data were collected and computed results were compiled. The organizations fielding these gages are Sandia National Laboratories-Albuquerque (SNLA), Lawrence Livermore National Laboratory (LLNL), and two groups from Los Alamos National Laboratory: the Geophysics Group (LANL EES-3) and the Explosion Effects Physics Project (LANL P-15). A more extensive rundown of institutions and the experiments they fielded on the NPE is given in Denny [1]. Figure 4 shows a plan view of the locations of the gages listed in Table 4; the distances in this figure are relative to the NPE SGZ. The depths for the LANL P-15 free-field gages (stations 14 and 20–41) were assigned in the simulations by using the surveyed invert depth and collar location and assuming the gage was grouted in 6 m below the invert; the horizontal locations for these gages were obtained from information contained in the LANL NTS Ground Motion Database [16] for the NPE. The locations of the LLNL surface gages were obtained from data in the SAC files[3] made available by LLNL. The ranges of the LANL surface gages were computed from information contained in the LANL NTS Ground Motion Database [16] for the NPE. The variation in elevation of the surface gages was not accounted for in the calculations, in which the surface gages were located in the topmost computational zone.

3.1 Free-Field Characteristics

The close-in free-field data collected on the NPE allow preliminary "ground truthing" of the calculations. For the NPE, the experimental records nearest the source are the CORRTEX data collected within the blasting agent and out into the surrounding rock; the furthest free-field gage was located approximately 1 km from the working point.

One measure of the effect of the blasting agent in the immediate vicinity of the chamber is shown in Figure 5, which depicts the shock range (in m) from the cavity centerline as a function of arrival time (in ms). The computational results are shown as the solid line, which gives the first-arrival time of the 1 kb pressure at a given location; these computed values are valid only out to a range of ~45 m. The dashed line in this figure represents the data from LANL CORRTEX cable K-3 [14], emplaced in drill hole KH-1 in the WP medium; this drill hole exited the NPE chamber radially in a direction roughly perpendicular to the access

[3] SAC (Seismic Analysis Code) is a general purpose interactive data analysis program developed by LLNL and widely used in the seismology community.

Gage Locations Used in the NPE Simulations

Station #	*Range* (m)	*Azimuth*	*Elevation* (m)	*Organization*	*Gage ID*
11	15.3	351	1853	SNLA	1YR
12	21.5	344	1853	SNLA	2YR
13	40.3	336	1853	SNLA	3YR,3YT,3AR,3AT
14	54.2	321	1846	LANL P-15	TM31
15	55.1	332	1853	SNLA	4YR,4YT,4AR
18	69.8	330	1853	SNLA	5YR,5YT,5AR,5AT,5AV
20	84.6	321	1846	LANL P-15	TM32
21	98.3	321	1846	LANL P-15	TM33
22	114	320	1846	LANL P-15	TM34
67	191	314	1841	SNLA	IH6
68	201	316	1841	SNLA	IH7
23	228	2	1842	LANL P-15	TM7
24	392	27	1842	LANL P-15	TM9
25	384	315	1843	LANL P-15	TM5
28	406	341	1846	LANL P-15	TM26
29	438	36	1835	LANL P-15	TM8
30	451	348	1846	LANL P-15	TM25
31	460	327	1846	LANL P-15	TM13
32	475	351	1846	LANL P-15	TM24
34	504	30,354	1840,1846	LANL P-15	TM14,TM23
35	512	328	1841	LANL P-15	TM1
36	676	38	1848	LANL P-15	TM10
38	724	51	1847	LANL P-15	TM12
39	758	15	1849	LANL P-15	TM11
40	1099	74	1843	LANL P-15	TM15
42	0	45	Surface	LLNL	GZ
44	171	101	Surface	LLNL	E4
45	261	168,289	Surface	LLNL	E1, H8
46	294	341	Surface	LLNL	Q4
64	337	9	Surface	LLNL	H7
65	356	64	Surface	LLNL	H6
66	409	23	Surface	LLNL	H3
48	442	90	Surface	LANL EES-3	S11P
47	458	285	Surface	LLNL	H9A, H9B
49	502	117	Surface	LANL EES-3	S11A
50	558	104	Surface	LLNL	E10
51	663	199	Surface	LANL EES-3	S6A
52	671	168	Surface	LLNL	E6
53	689	171	Surface	LANL EES-3	S10P
54	728	310	Surface	LLNL	Q5
56	789	156	Surface	LANL EES-3	S10A
55	800	217	Surface	LANL EES-3	S6P
57	821	359	Surface	LLNL	Q3
58	868	248	Surface	LANL EES-3	S4A
59	920	67	Surface	LANL EES-3	S12P
60	1045	254	Surface	LANL EES-3	S4P
61	1265	268	Surface	LANL EES-3	S2A
62	1237	185	Surface	LANL EES-3	S8A
63	1475	275	Surface	LANL EES-3	S2P

Table 4: Listed are the calculation station number, the horizontal range (m) from the working point, the source-to-station azimuth (degrees East of North), gage elevation (m above mean sea level), the fielding organization, and that organization's gage ID for the gage locations used in the NPE simulations.

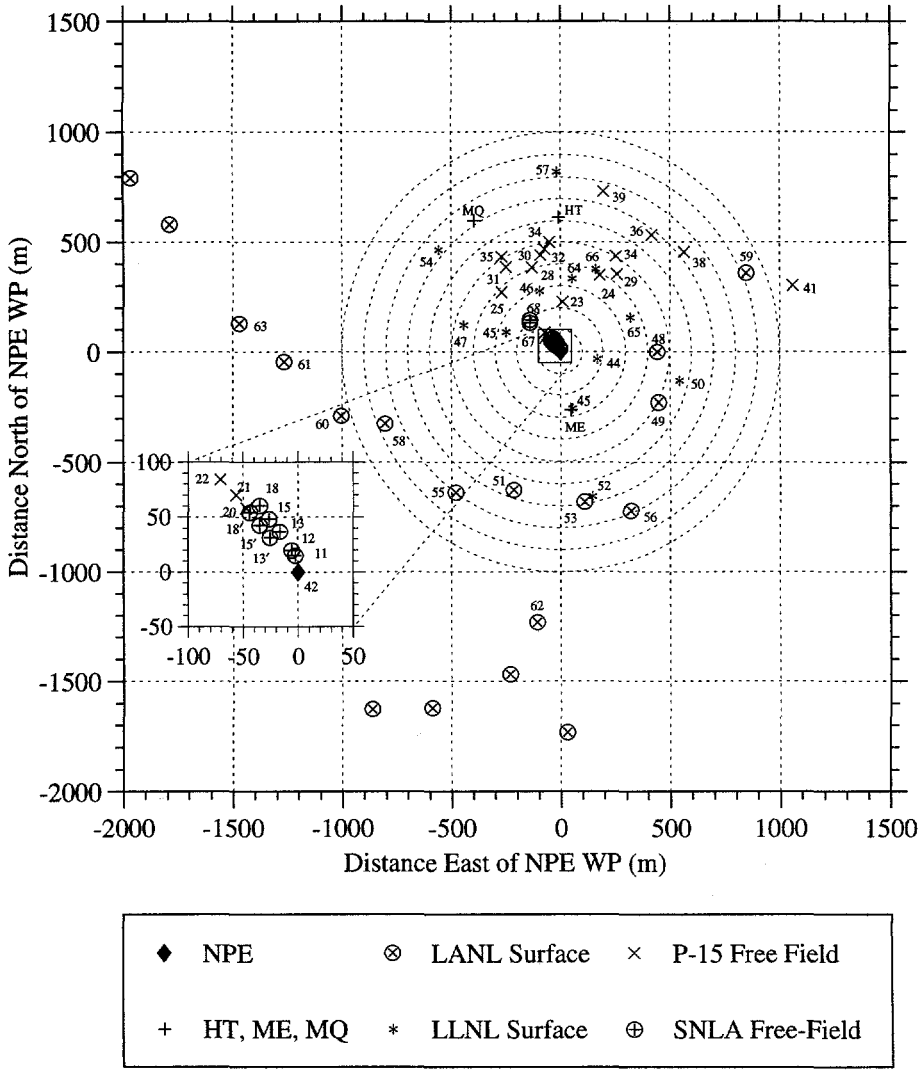

Figure 4: Plan view of the NPE gage locations. The gage locations shown are listed in Table 4 for the NPE shot and simulations. Distances are given in m relative to the NPE SGZ. The dashed circles surrounding SGZ have radii increasing in 100 m increments.

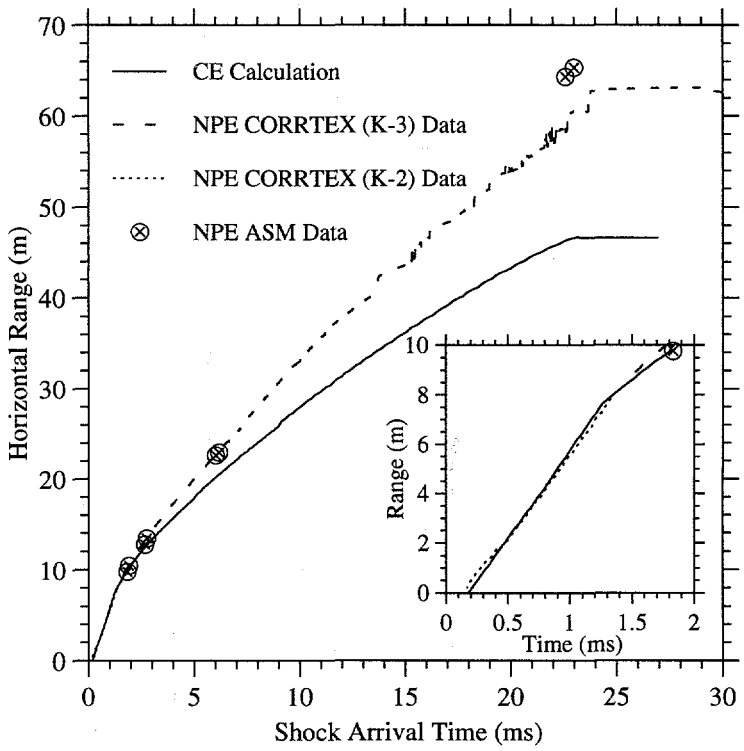

Figure 5: Shock arrival time near the NPE WP. The shock range (m) from the center of the cavity in and around the NPE blasting agent is plotted as a function of arrival time (ms). The solid line denotes the CE calculation 1 kb locus; the dashed line represents the data from LANL CORRTEX cable K-3 [14], emplaced in drill hole KH-1 in the WP medium, which exited the NPE chamber roughly perpendicular to the access drift; the dotted line (see inset) represents the data from LANL CORRTEX cable K-2 [14], located horizontally along the centerline in the NPE chamber; TOA data from LANL ASM gages [17] are denoted $\otimes$. The inset shows the early-time, close-in response. This figure shows that the blasting agent burn was modeled well, while the shock speed in the experiment was somewhat higher than in the calculation.

drift. The dotted line (see inset) represents the data from LANL CORRTEX cable K-2 [14], which was emplaced horizontally in the NPE chamber, approximately halfway between the back and invert. Denoted by $\otimes$ are the time of arrival (TOA) data according to axisymmetric magnetic (ASM) gages [17] that were sited in CORRTEX drill holes. The slight "knee" in the curves at ~8 m (see inset) corresponds to the edge of the NPE chamber, demonstrating the difference in shock velocity between the blasting agent and the surrounding tuff. The degradation of the CORRTEX cable data at ranges greater than ~40 m reflects the decreased sensitivity of that cable to the lower peak pressures at those ranges. The inset shows the nonzero initiation time for the blasting agent in the data and in the calculation. McKown [14] suggests that this offset in the data may be related to finite distance between the CORRTEX cables and the detonation boosters (which were not located exactly on the chamber centerline). In the calculation, the initiation times of the three detonation points were adjusted so that the computed shock arrival times at the edge of the chamber approximated the data at the three vertical CORRTEX levels; the final values determined for these delays were: $\Delta t_{\text{init}}^{\text{bottom}} = 0.3$ ms, $\Delta t_{\text{init}}^{\text{middle}} = 0.2$ ms, $\Delta t_{\text{init}}^{\text{top}} = 0.15$ ms. This figure shows that the simulated burn within the chamber was reasonably well modeled, while the shock propagation into the surrounding rock was somewhat slower in the calculation than the experiment, suggesting that the equation of state for the working point tuff was not entirely accurate.

The material response of close-in free-field gages is shown in Figs. 6–10, in which the data collected by C. W. Smith of SNLA [18] are compared with calculations. In these figures, only the first 100 ms of the waveforms are shown, and the termination of the experimental data is associated with the time of gage failure. At the two closest stations (Figs. 6 and 7) only radial stress data were collected, while at the more distant stations the experimental data consisted of radial (rr) and tangential (zz) stresses and radial (r) and tangential (z) accelerations; the other quantities are derived from these data, e.g., velocities are integrated accelerations, and pressure is mean stress ($p = -1/3(\sigma_{rr} + 2\sigma_{zz})$). Figures 6–10 contain plots of radial acceleration (m/s^2) vs. time (s), radial velocity (m/s) vs. time (s), tangential acceleration (m/s^2) vs. time (s), tangential velocity (m/s) vs. time (s), pressure (GPa) vs. time (s), stress difference (GPa) (i.e., $|\sigma_{rr} - \sigma_{zz}|$) vs. pressure (GPa) for the CE simulation (solid line), the NE simulation (long dashed line), and the SNLA data (short dashed line). The experimental stress curves in these plots have been vertically offset to match the undisturbed stress level in the simulations. At the ranges of stations 13 (40 m), 15 (55 m), and 18 (70 m) two sets of gages were sited: one set in drill holes in the rock, the other in the grouted access drift (see Fig. 4); in Figs. 8–10 we compare calculated results with the former, as the waveforms from the latter exhibited somewhat different characteristics that are likely related to the material response of the grout [19]. This SNLA data set is exceptionally valuable in that both radial and tangential stress data were collected at several locations; the stress differences constructed from these data are particularly illuminating

insofar as they reveal shear failure behavior of the material.

Comparing the computed and experimental radial stress at 15 m and 21 m (Figs. 6 and 7), the most notable aspects are the slightly sooner arrival of the shock and the somewhat greater peak in the experimental data. These data also appear to contain some structure in the unload that is qualitatively captured in the calculations, but the early gage failure time (~10 ms) precludes any meaningful comparison.[4] The CE calculations at these stations exhibit peak radial velocity and stress higher than the NE calculations, which, at these close ranges, is probably related to the greater initial cavity extent in the CE case (i.e., these stations are closer to the edge of the source in the CE simulation than in the NE calculation). By 40 m range (Fig. 8), the apparently higher sound speed of the *in situ* rock is still evident in the experimental records.

The computed pressure and velocity waveforms at 55 m and 70 m (Figs. 9 and 10) exhibit a distinct "knee" in the initial wavefront at ~20 MPa; this feature, which occurs at a pressure somewhat higher than that of incipient shear failure (as inferred from the stress difference vs. pressure plots), appears to be related to a contemporaneous trough in acceleration. Similarly, the slight knees in the experimental radial velocity data at these stations are temporally coincident with troughs in the radial acceleration records. The slight knee at ~95 MPa in the 55 m experimental axial stress plot (Fig. 9), and reflected in the pressure plot, does not appear to be attributable to shear failure phenomena. The knee at ~40 MPa in the 70 m experimental pressure plot (Fig. 10) occurs simultaneously with similar features in the radial velocity, radial stress, and axial stress records (the last two are not depicted); although the features in the radial velocity and radial stress may be suggestive of, e.g., pore crush phenomena, the slope discontinuity exhibited in the axial stress is possibly suggestive of a gage inclusion effect [19]. Despite the differences between specific features of the computed pressure and velocity profiles and those of the experimental data in this highly inelastic region, key waveform characteristics (peak, unload, width) are reasonably well matched.

Figure 11 depicts the stress difference vs. mean stress inferred from the data at 40, 55, and 70 m together with the shear failure curve used in the calculations. This diagram, together with the plots of stress difference vs. pressure shown in Figures 9–10, illustrate clearly our assumption that the working point material is significantly weaker in shear failure than the data suggest, i.e., we assume that inelastic processes in the material commence at a lower shear strength. We, as well as other investigators [20], found such an assumption necessary to obtain the heuristically acceptable correspondence between computed waveforms and experimental stress and velocity data (using the experimental data as a starting point). The reason for this is unclear: on similar calculations for nearby nuclear events, similar (low) shear strength values are required for reasonable waveform

[4] Indeed, since only early-time radial stress data were available at these two stations, these waveforms were not used in the *ad hoc* iterative waveform matching process by which material properties were modified.

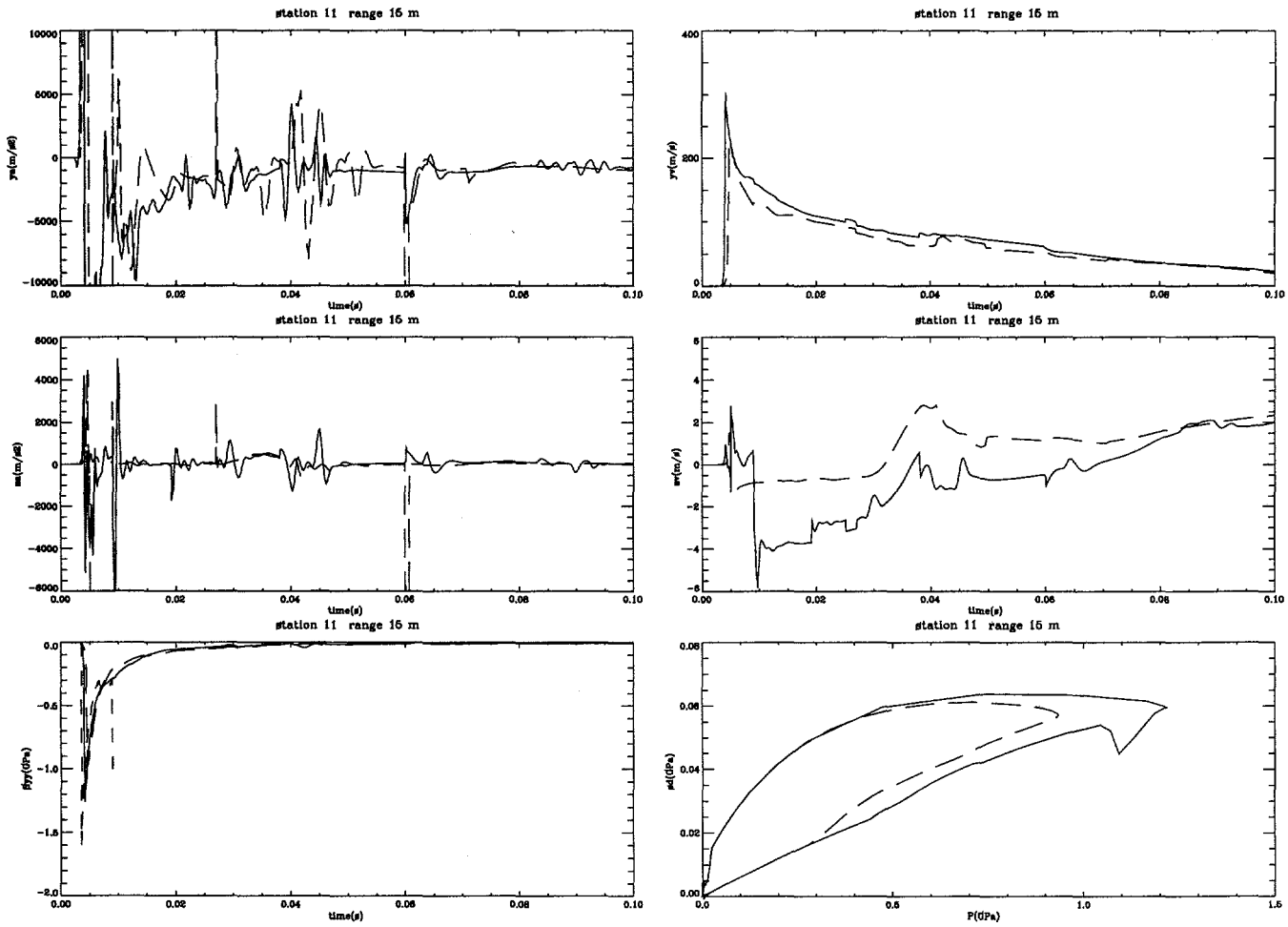

Figure 6: Experimental and computational free-field results at 15 m. Shown are the radial acceleration (m/s^2), radial velocity (m/s), tangential acceleration (m/s^2), tangential velocity (m/s), and radial stress (GPa) vs. time (s), and stress difference (GPa) (i.e., absolute value of radial stress minus tangential stress) vs. pressure (GPa) at shot depth and 15 m range from the NPE WP. Only the first 100 ms of the calculated results are depicted. The solid lines denote the CE simulations; the long dashed lines represent the NE simulations; the short dashed line (radial pressure only) represents the NPE data collected by SNLA [18], gage 1YR (see Table 4).

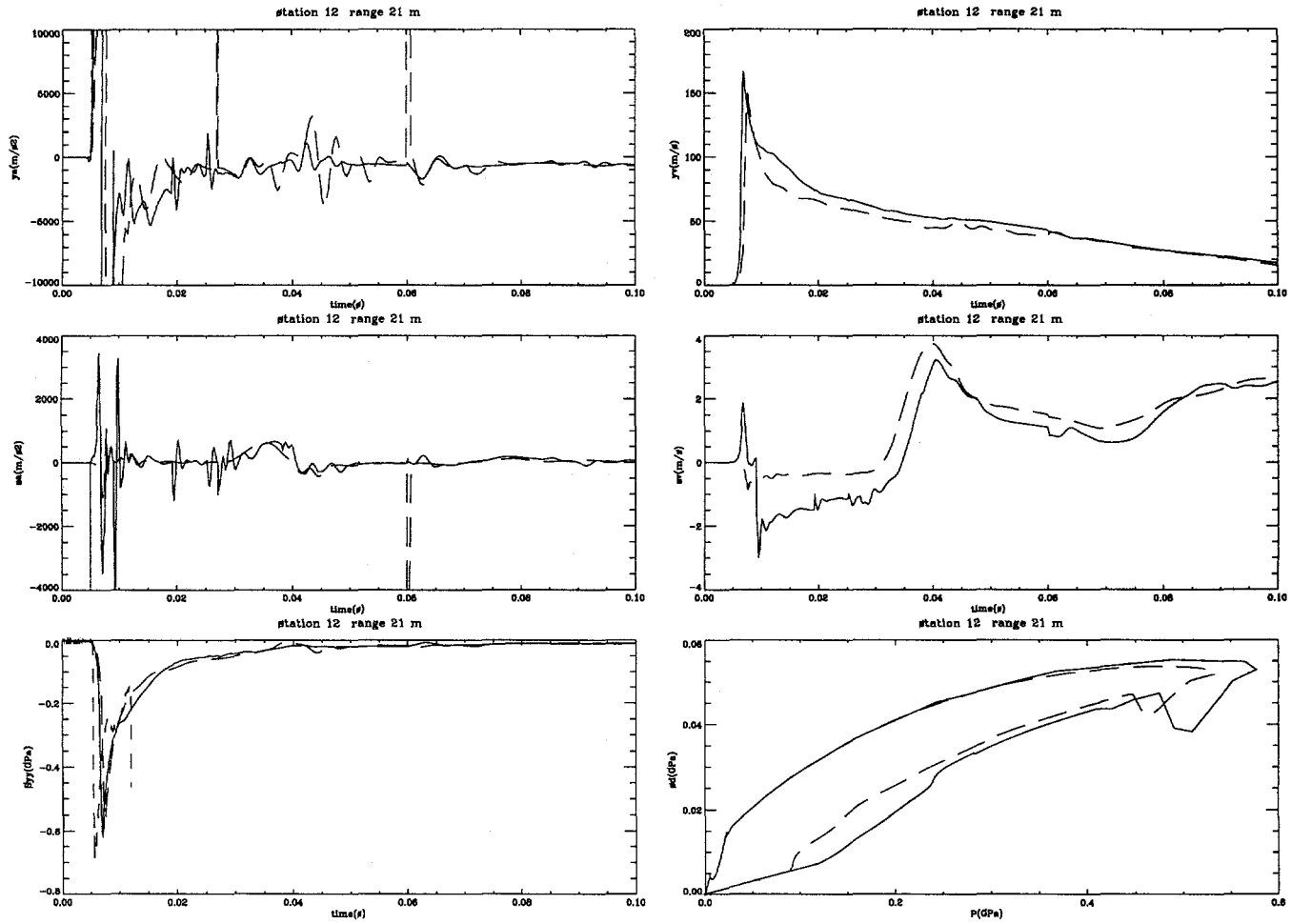

Figure 7: Experimental and computational free-field results at 21 m. Shown are the radial acceleration (m/s^2), radial velocity (m/s), tangential acceleration (m/s^2), tangential velocity (m/s), and radial stress (GPa) vs. time (s), and stress difference (GPa) (i.e., absolute value of radial stress minus tangential stress) vs. pressure (GPa) at shot depth and 21 m range from the NPE WP. Only the first 100 ms of the calculated results are depicted. The solid lines denote the CE simulations; the long dashed lines represent the NE simulations; the short dashed line (radial pressure only) represents the NPE data collected by SNLA [18], gage 2YR (see Table 4).

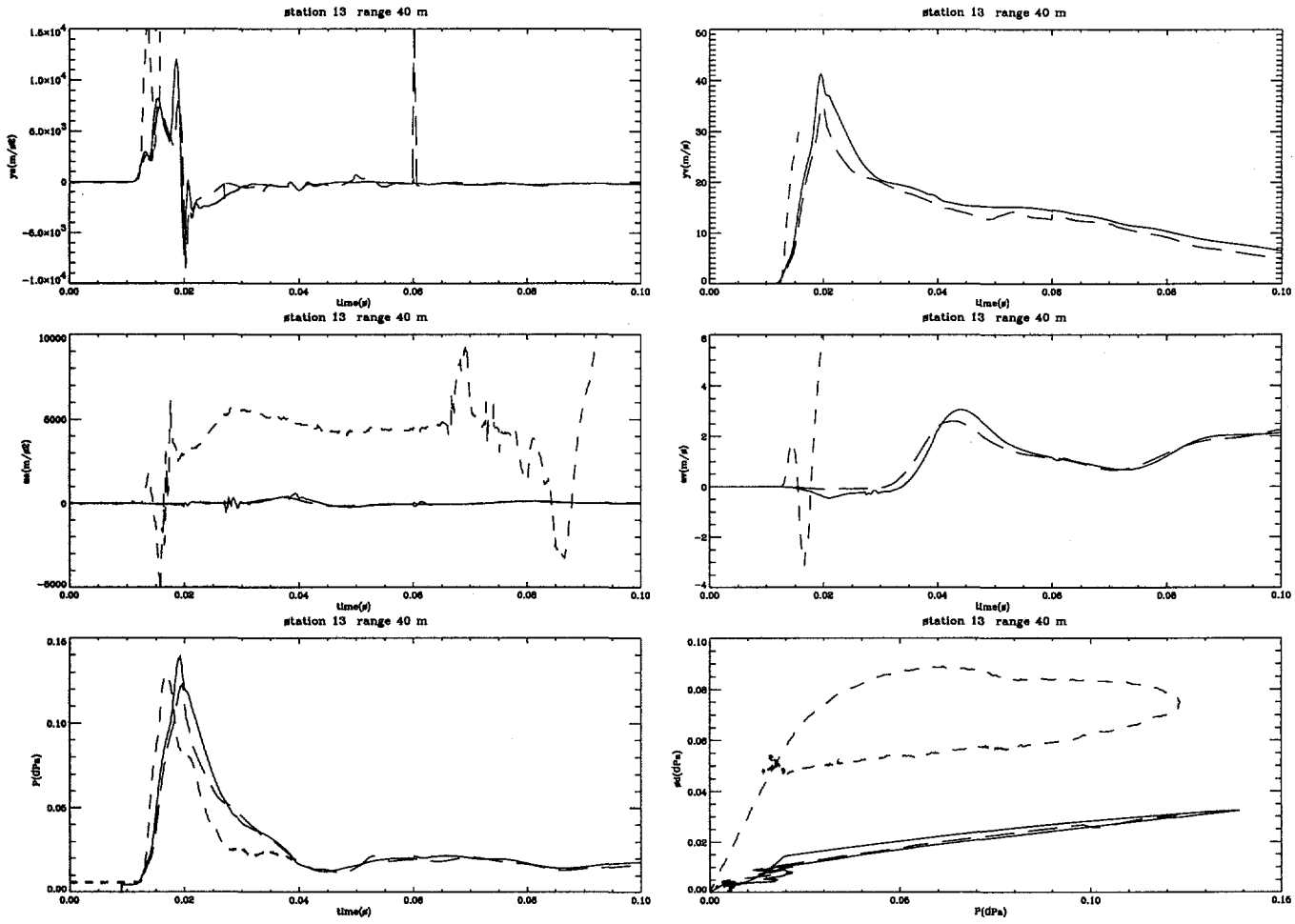

Figure 8: Experimental and computational free-field results at 40 m. Shown are the radial acceleration (m/s^2), radial velocity (m/s), tangential acceleration (m/s^2), tangential velocity (m/s), and pressure (GPa) vs. time (s), and stress difference (GPa) (i.e., absolute value of radial stress minus tangential stress) vs. pressure (GPa) at shot depth and 40 m range from the NPE WP. Only the first 100 ms of the calculated results are depicted. The solid lines denote the CE simulations; the long dashed lines represent the NE simulations; the short dashed line represents the NPE data collected by SNLA [18], gages 3YR, 3YT, 3AR, 3AT (see Table 4).

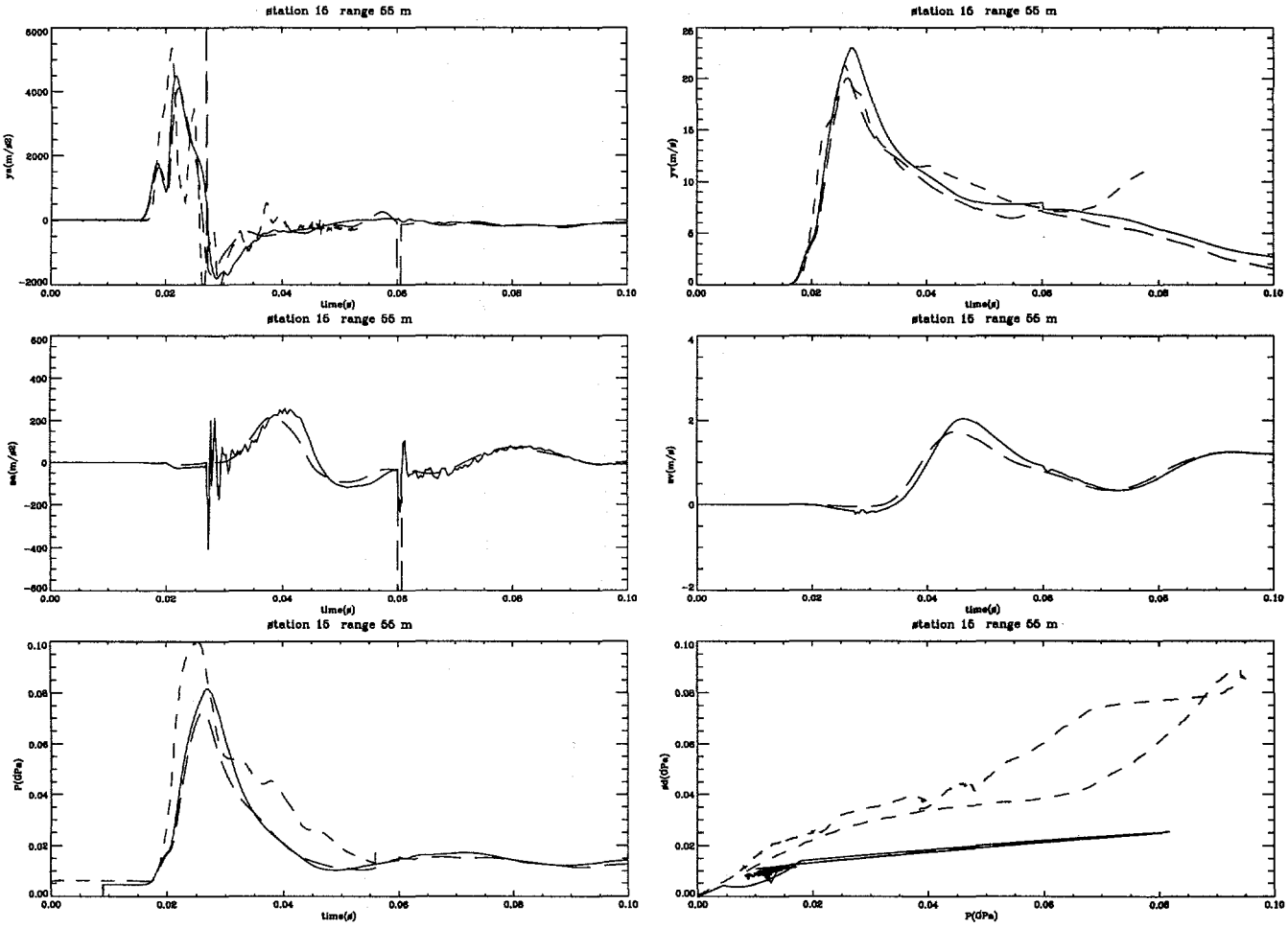

Figure 9: Experimental and computational free-field results at 55 m. Shown are the radial acceleration (m/s^2), radial velocity (m/s), tangential acceleration (m/s^2), tangential velocity (m/s), and pressure (GPa) vs. time (s), and stress difference (GPa) (i.e., absolute value of radial stress minus tangential stress) vs. pressure (GPa) at shot depth and 55 m range from the NPE WP. Only the first 100 ms of the calculated results are depicted. The solid lines denote the CE simulations; the long dashed lines represent the NE simulations; the short dashed line represents the NPE data collected by SNLA [18], gage 4YR, 4YT, 4AR (see Table 4). There are no z-acceleration or z-velocity data at this station.

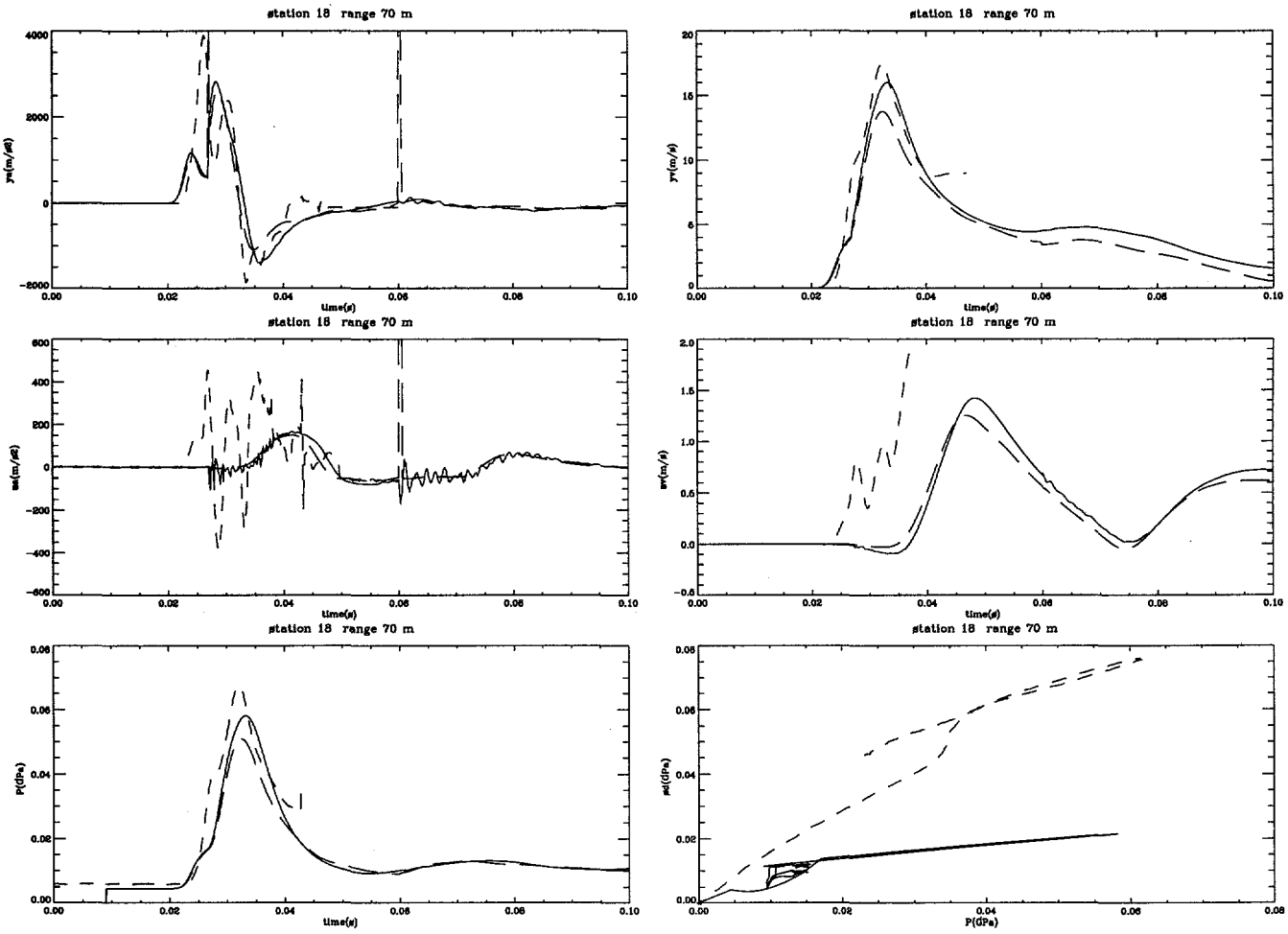

Figure 10: Experimental and computational free-field results at 70 m. Shown are the radial acceleration (m/s^2), radial velocity (m/s), tangential acceleration (m/s^2), tangential velocity (m/s), and pressure (GPa) vs. time (s), and stress difference (GPa) (i.e., absolute value of radial stress minus tangential stress) vs. pressure (GPa) at shot depth and 70 m range from the NPE WP. Only the first 100 ms of the calculated results are depicted. The solid lines denote the CE simulations; the long dashed lines represent the NE simulations; the short dashed line represents the NPE data collected by SNLA [18], gage 5YR, 5YT, 5AR, 5AT (see Table 4).

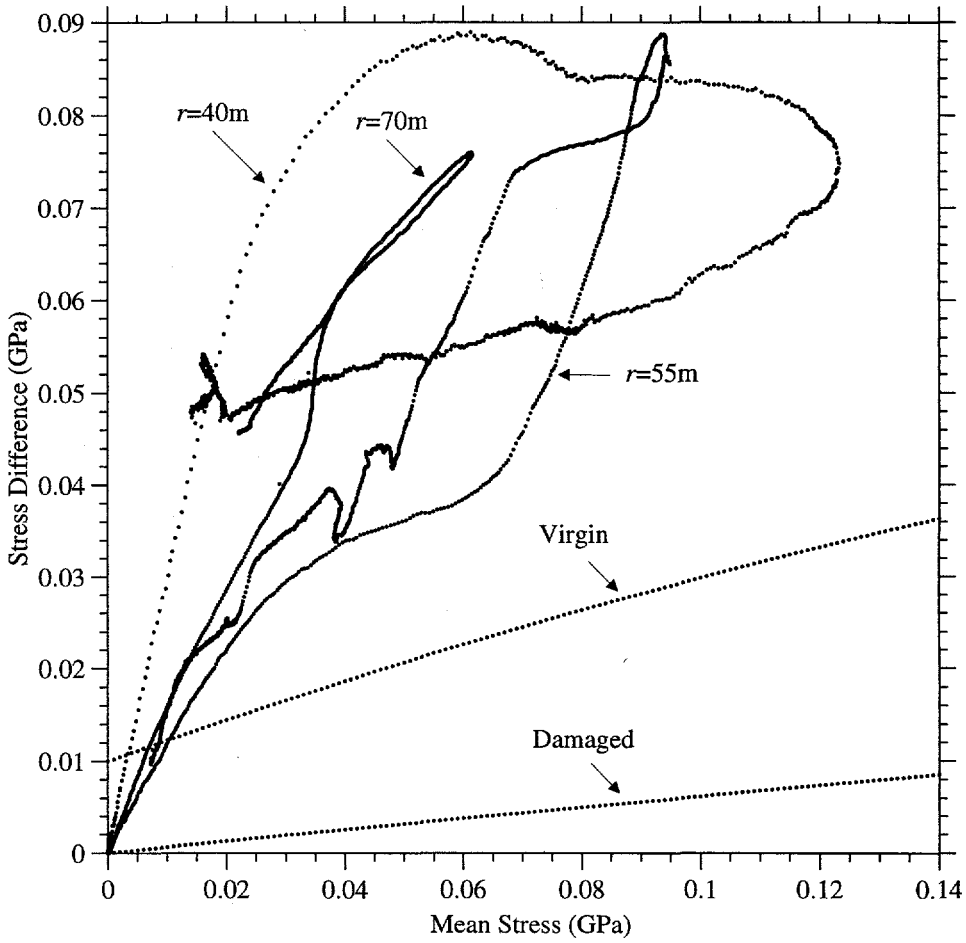

Figure 11: Experimental and computational stress difference vs. pressure. The stress difference (GPa) (i.e., absolute value of radial stress minus tangential stress) is plotted against the mean stress (GPa) from experimental data and corresponding shear failure surface used in the numerical simulations. As discussed in the text, the discrepancy between the experimental data and the computational model is presently inexplicable, as are the differences between the experimental stress paths. The NPE data were collected at shot-level gages by SNLA [18] at stations 3YR and 3YT (40 m), 4YR and 4YT (55 m), and 5YR and 5YT (70 m) (see Table 4).

matches. One explanation could be that a rate-hardening mechanism, which results in high shear strength at these very-near-source locations, causes this response. Alternatively, preliminary calculations with an effective stress model (as previously mentioned) for the working point material, using a somewhat higher shear strength, provide good waveform matches with experimental data at close-in stations, suggesting that the physics contained in that model may more accurately reflect reality. Finally, one could posit that there are (unknown) irregularities with the experimental data; given the high quality of that data set [19], however, we are disinclined to believe this to be the case.

The material response of more distant free-field gages is shown in Figures 12-28, which present comparisons of calculated values with the data collected by K. Olsen and A. Peratt of LANL P-15 [21] and H. D. Garbin of SNLA [22]. These figures contain plots of radial acceleration (m/s^2) vs. time (s), radial velocity (m/s) vs. time (s), vertical acceleration (m/s^2) vs. time (s), vertical velocity (m/s) vs. time (s), reduced velocity potential (RVP) (m^3/s) vs. reduced time (s), and RVP spectrum (m^3) vs. frequency (Hz) for the CE simulation (solid line), and the NE simulation (long dashed line) and 2 s of the actual data (short dashed line). The data collected are accelerometer records that have been demeaned and integrated to obtain velocities. (Unfortunately, the three closest gage packages fielded by Olsen & Peratt, at ranges of 54, 84, and 98 m, failed during the shot.) To better display the wave structure, the first 1 s of waveforms is shown at ranges out to ~400 m (Figs. 12-18), while the full 2 s of the calculation is provided at ranges greater than ~400 m (Figs. 19-28).

We first discuss the features of the waveforms shown in these figures. The calculated first arrivals are somewhat earlier than those of the experimental data, indicating that the sound speed assigned to the working point material (c_ℓ = 2730 m/s) may be somewhat too high. With the exception of station 25 (384 m range, gage TM5, Fig. 16), the experimental data for which appear questionable, the computed peak and pulse width of the initial wave train are in reasonably good agreement with the experimental data. Not unexpectedly, features of the subsequent wave structure are in somewhat poorer agreement.

Examination of the radial velocities (upper right plot) reveals a distinct secondary peak along the unload from the initial pulse that is present at some stations (e.g., Fig. 13, 191 m range), but not in others (e.g., Fig 17, 392 m range); comparing gages at similar ranges but different azimuths suggests that this feature varies as follows: gages located NNW of the source exhibit this secondary pulse, while those NE of the source have smooth primary unload behavior. For example, contrast the first-pulse behavior in the experimental radial velocity traces (short dashed line) in Figs. 18 (406 m range) and 17 (392 m range), Figs. 21 (460 m range) and 19 (438 m range), Figs. 24 (512 m range) and 23 (504 m range); the first cited figure in each of these pairs is located NNW of the source and exhibits the secondary radial velocity peak, while the second is located ENE at approximately the same range yet shows smooth unload behavior. Similar features were found by App & Brunish [7] in comparisons

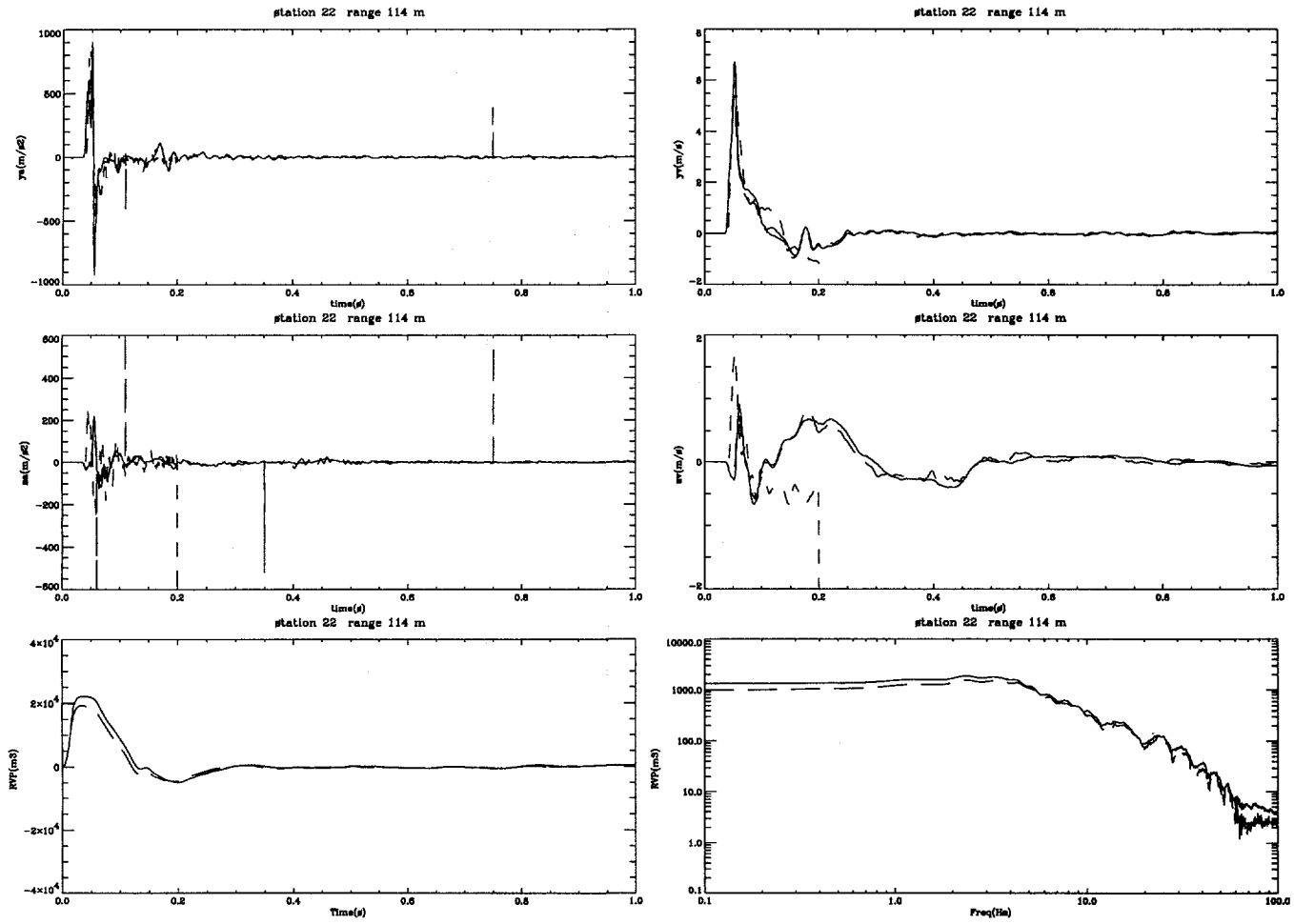

Figure 12: Experimental and computational free-field results at 114 m. Shown are the radial acceleration (m/s^2), radial velocity (m/s), vertical acceleration (m/s^2), and vertical velocity (m/s) vs. time (s), RVP (m^3/s) vs. reduced time (s), and RVP spectrum (m^3) vs. frequency (Hz) at shot depth and 114 m range from the NPE WP. Only the first 1 s of the calculated results are depicted. The solid lines denote the CE simulations; the long dashed lines represent the NE simulations; the short dashed line represents the NPE data collected by LANL P-15 [21], gage TM34. There was insufficient gage data (only ~0.2 s) at this location to compute the RVP and RVP spectrum.

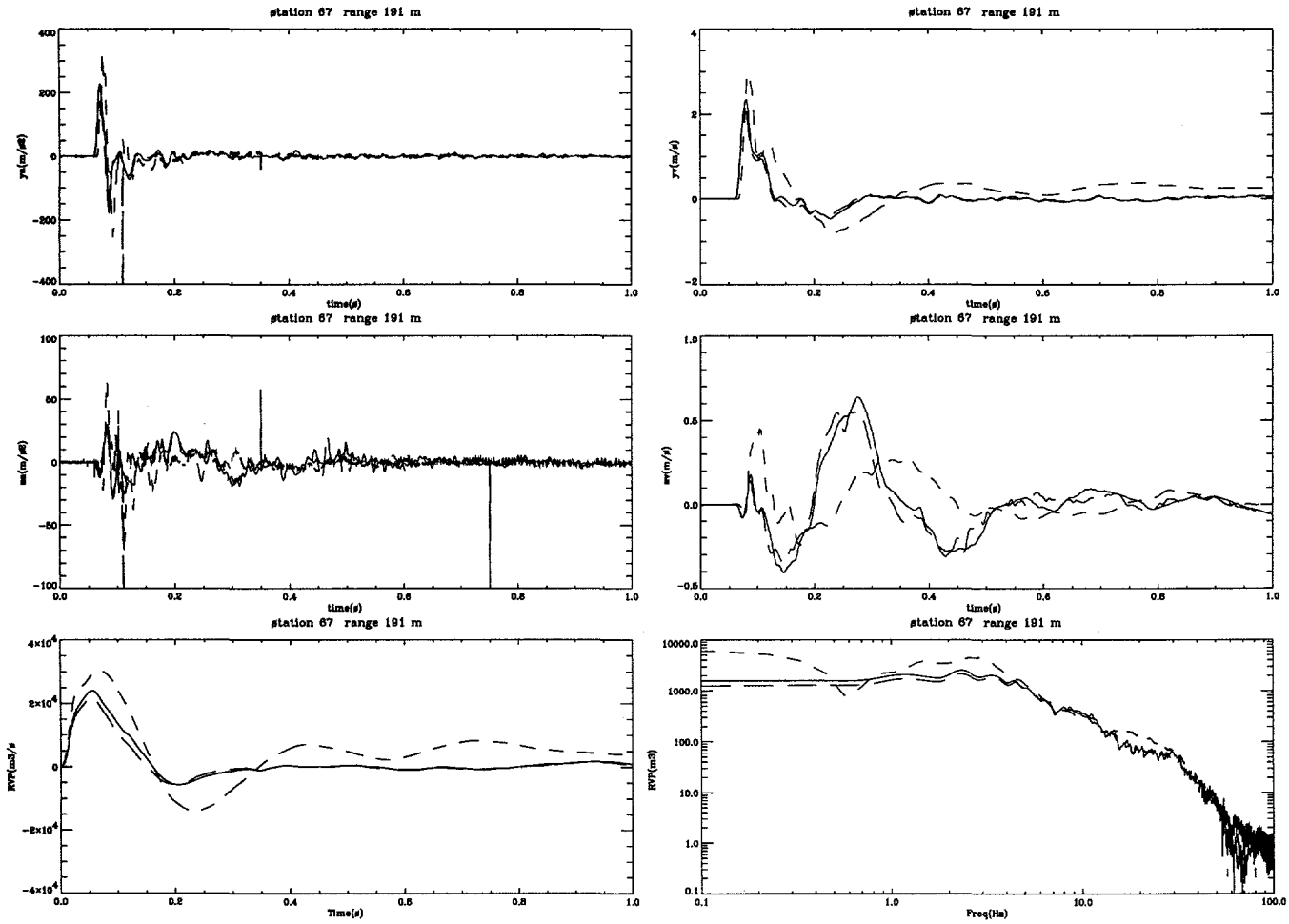

Figure 13: Experimental and computational free-field results at 191 m. Shown are the radial acceleration (m/s^2), radial velocity (m/s), vertical acceleration (m/s^2), and vertical velocity (m/s) vs. time (s), RVP (m^3/s) vs. reduced time (s), and RVP spectrum (m^3) vs. frequency (Hz) at shot depth and 191 m range from the NPE WP. Only the first 1 s of the calculated results are depicted. The solid lines denote the CE simulations; the long dashed lines represent the NE simulations; the short dashed line represents the NPE data collected by H. D. Garbin of SNLA [22], gage IH6.

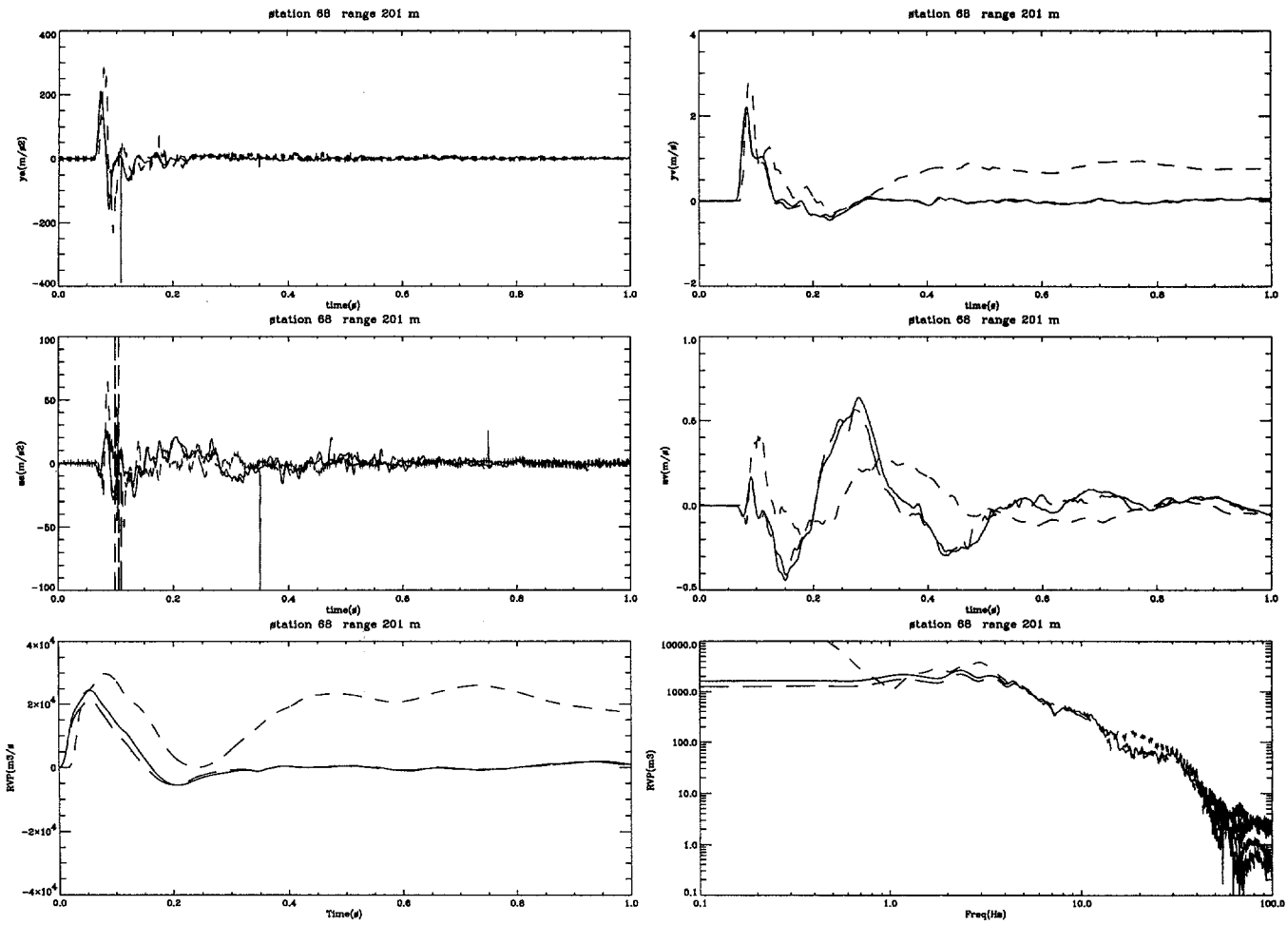

Figure 14: Experimental and computational free-field results at 201 m. Shown are the radial acceleration (m/s^2), radial velocity (m/s), vertical acceleration (m/s^2), and vertical velocity (m/s) vs. time (s), RVP (m^3/s) vs. reduced time (s), and RVP spectrum (m^3) vs. frequency (Hz) at shot depth and 201 m range from the NPE WP. Only the first 1 s of the calculated results are depicted. The solid lines denote the CE simulations; the long dashed lines represent the NE simulations; the short dashed line represents the NPE data collected by H. D. Garbin of SNLA [22], gage IH7.

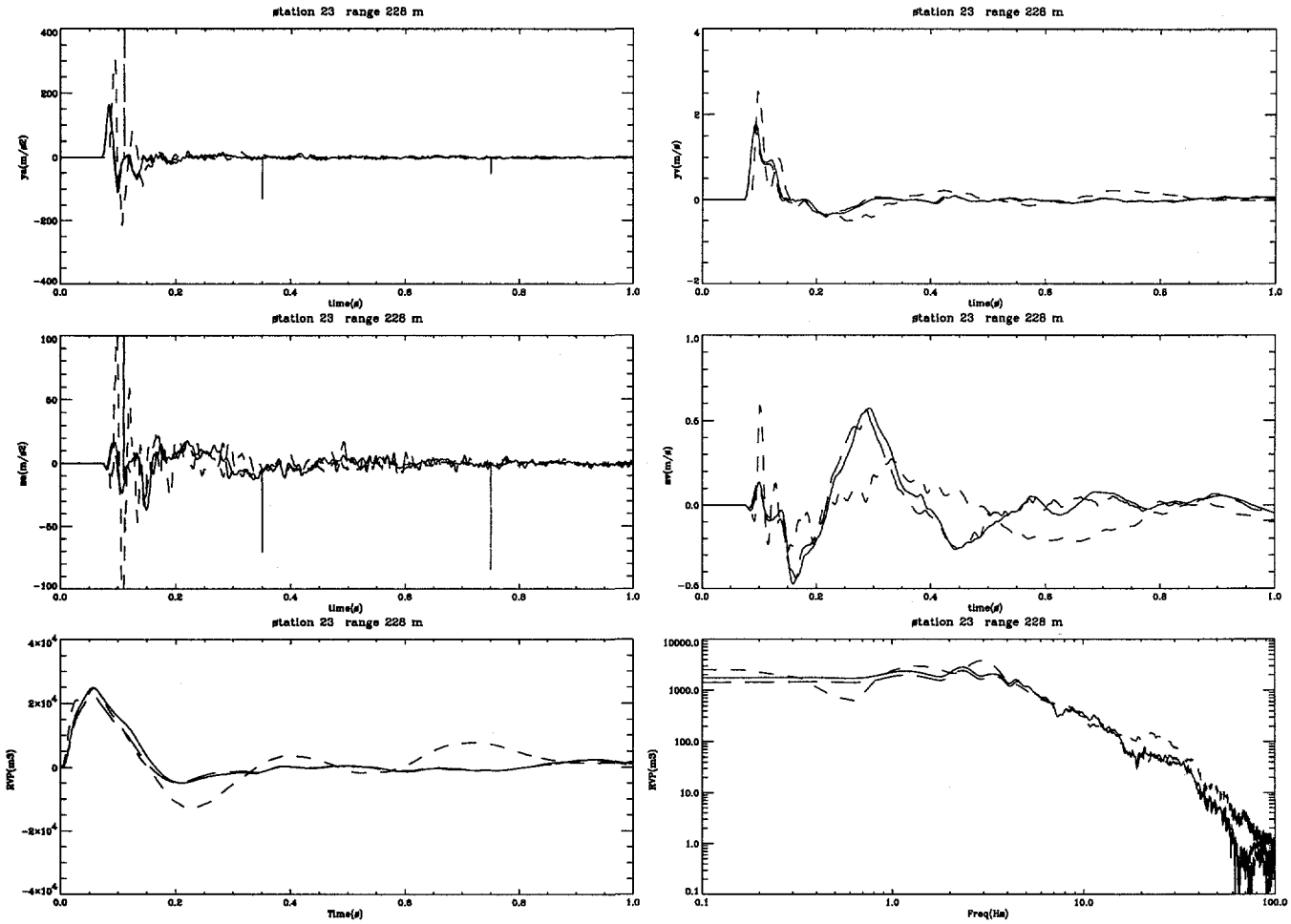

Figure 15: Experimental and computational free-field results at 228 m. Shown are the radial acceleration (m/s^2), radial velocity (m/s), vertical acceleration (m/s^2), and vertical velocity (m/s) vs. time (s), RVP (m^3/s) vs. reduced time (s), and RVP spectrum (m^3) vs. frequency (Hz) at shot depth and 228 m range from the NPE WP. Only the first 1 s of the calculated results are depicted. The solid lines denote the CE simulations; the long dashed lines represent the NE simulations; the short dashed line represents the NPE data collected by LANL P-15 [21], gage TM7.

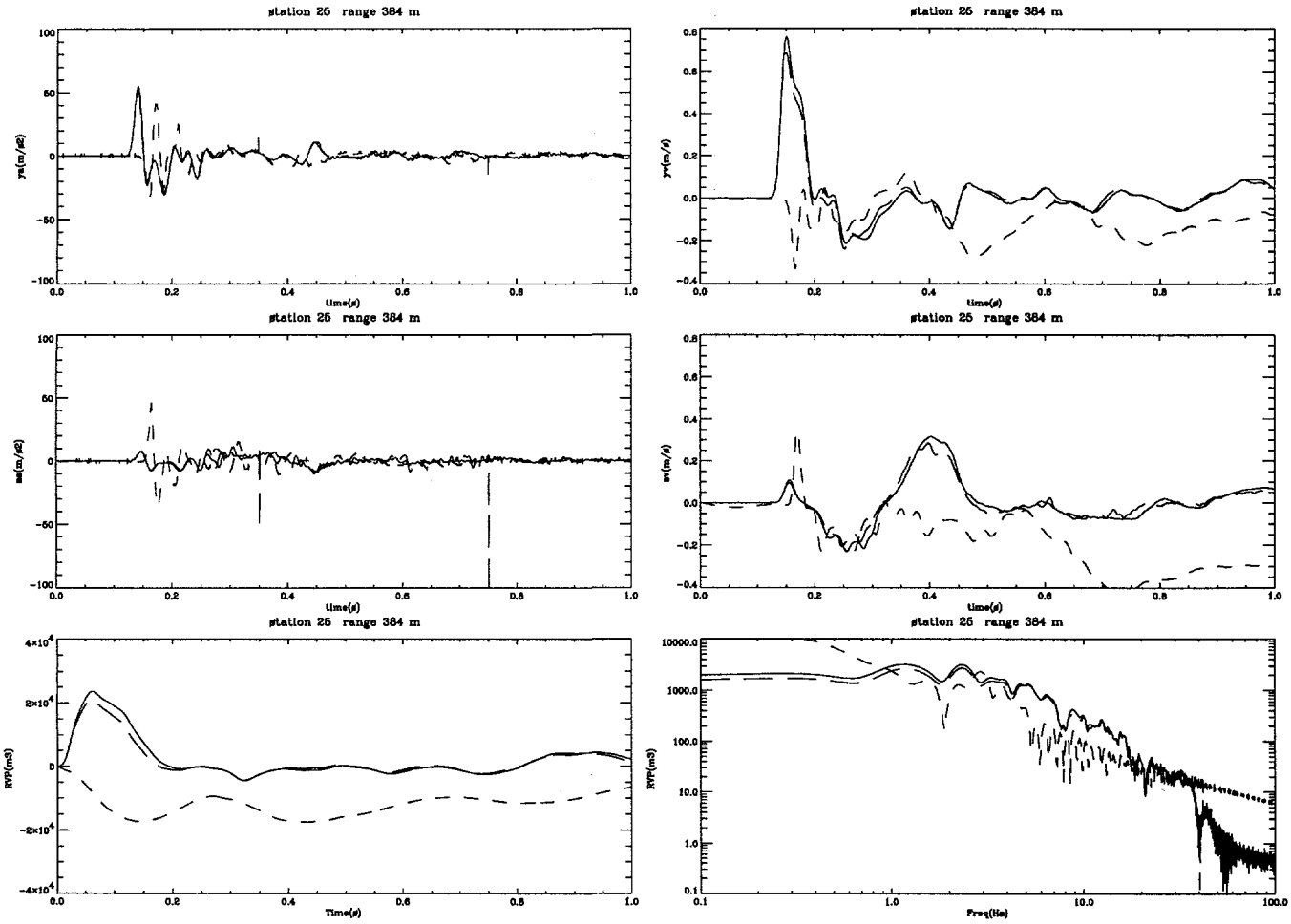

Figure 16: Experimental and computational free-field results at 384 m. Shown are the radial acceleration (m/s^2), radial velocity (m/s), vertical acceleration (m/s^2), and vertical velocity (m/s) vs. time (s), RVP (m^3/s) vs. reduced time (s), and RVP spectrum (m^3) vs. frequency (Hz) at shot depth and 384 m range from the NPE WP. Only the first 1 s of the calculated results are depicted. The solid lines denote the CE simulations; the long dashed lines represent the NE simulations; the short dashed line represents the NPE data collected by LANL P-15 [21], gage TM5. The validity of the experimental radial data at this station appears questionable.

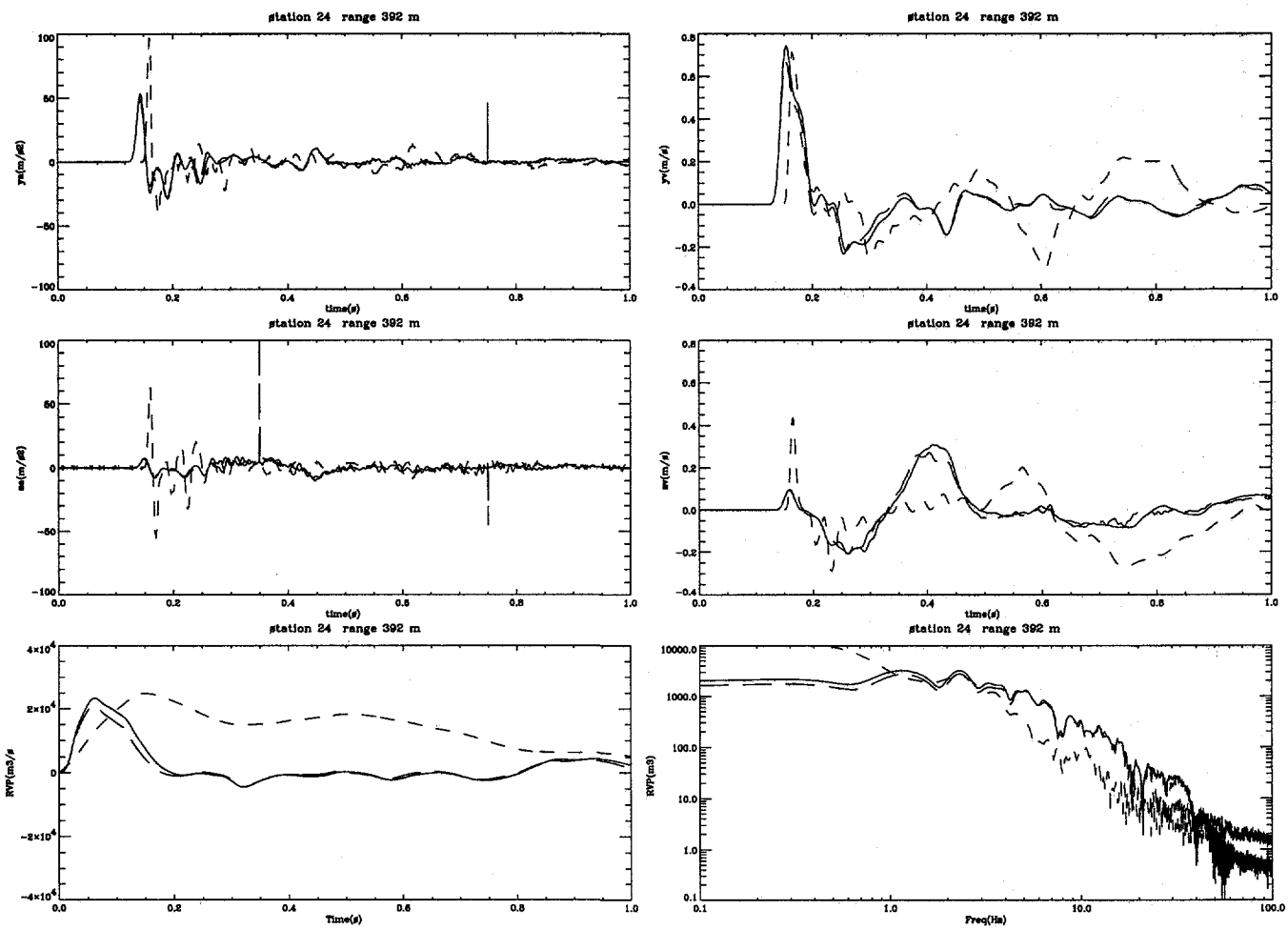

Figure 17: Experimental and computational free-field results at 392 m. Shown are the radial acceleration (m/s^2), radial velocity (m/s), vertical acceleration (m/s^2), and vertical velocity (m/s) vs. time (s), RVP (m^3/s) vs. reduced time (s), and RVP spectrum (m^3) vs. frequency (Hz) at shot depth and 392 m range from the NPE WP. Only the first 1 s of the calculated results are depicted. The solid lines denote the CE simulations; the long dashed lines represent the NE simulations; the short dashed line represents the NPE data collected by LANL P-15 [21], gage TM9.

of calculated results with experimental waveforms for MISTY ECHO, located approximately 250 m due south of the NPE. Comparing six different gages, these authors noted the same azimuthal dependence that we see in the NPE waveforms, and suggested that the bedding of the stratigraphic units may be responsible for this behavior. Specifically, App & Brunish suggest that the more complex release features of waveforms from gages downdip (roughly NW) are due to reflected waves from the vitric unit (Tt5 in Fig. 2), the boundary of which is considerably closer to gage level along this azimuth; correspondingly, along strike (roughly NE) the stratigraphy is more nearly uniformly horizontal, so the waveforms more closely match the waveforms App & Brunish computed with the horizontal layering they assumed. Our findings are consistent with this hypothesis; moreover, at closer-in locations (e.g., Fig. 13), the small plateau in the computed radial velocity upon unloading from the first peak is similar to the secondary peak seen in the data.

Vertical velocity traces (middle right plot) display somewhat less agreement between data and calculation than the radial velocity. As shown in Figures 13 (191 m range), 14 (201 m range), and 15 (228 m range), the vertical velocity exhibits an initial downward pulse in both data and calculation; at all subsequent gage locations (range 384 m and beyond), however, the initial vertical pulse is upward. At all stations, the amplitude of the computed initial vertical velocity is lower than the corresponding data; the width of the initial pulse, however, is approximately correct. Much of the structure evident in the first $\sim$1 s of the vertical velocity waveforms is related to the layering, with the impedence mismatch between the Tt4 (working point) and Tt5 (above) units presumed to be the significant contributor; these effects are evident when compared with the uniform material calculation, which we discuss later.

As observed by Olsen & Peratt [23], the magnitude of the axial and transverse tunnel-level motion captured in the LANL P-15 data set is nearly comparable to that of the radial motions, which suggests a significant departure from spherical symmetry. Although our cylindrically symmetric calculations do not admit transverse motions, the axial motions we compute are of essentially the same amplitude as the experimental axial data. Olsen & Peratt [23] speculate that scattering processes due to medium inhomogeneities contribute to this effect, which is observed to increase with propagation distance.

Figure 29 is a record section plot of the free-field radial velocity vs. time, in which the ordinate for *each* trace has been normalized (so that, e.g., only gross structure should be compared), with the solid lines representing computed waveforms and the dotted lines denoting the experimental data. In this figure, the arrival of the calculated front is early relative to the data at ranges greater than $\sim$100 m (indicating that the ascribed sound speed of the WP material is too high). Greater decorrelation is evidenced in the experimental data, which include stations at varying azimuths, as opposed to the calculated waveforms, which admit identification of related structures induced by both imposed cylindrical symmetry and horizontal layering. Figure 30 contains the same data at

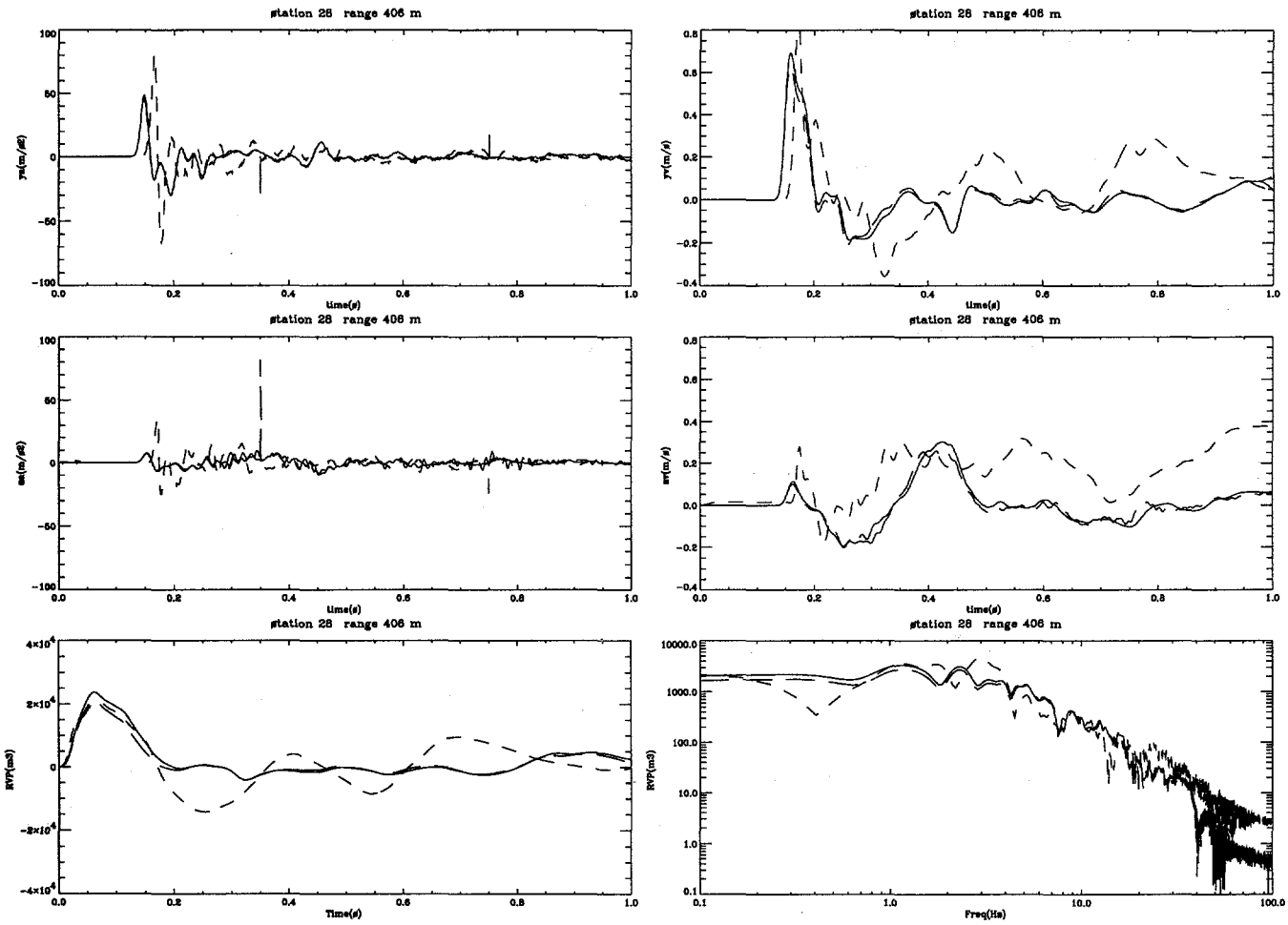

Figure 18: Experimental and computational free-field results at 406 m. Shown are the radial acceleration (m/s^2), radial velocity (m/s), vertical acceleration (m/s^2), and vertical velocity (m/s) vs. time (s), RVP (m^3/s) vs. reduced time (s), and RVP spectrum (m^3) vs. frequency (Hz) at shot depth and 406 m range from the NPE WP. Only the first 1 s of the calculated results are depicted. The solid lines denote the CE simulations; the long dashed lines represent the NE simulations; the short dashed line represents the NPE data collected by LANL P-15 [21], gage TM26.

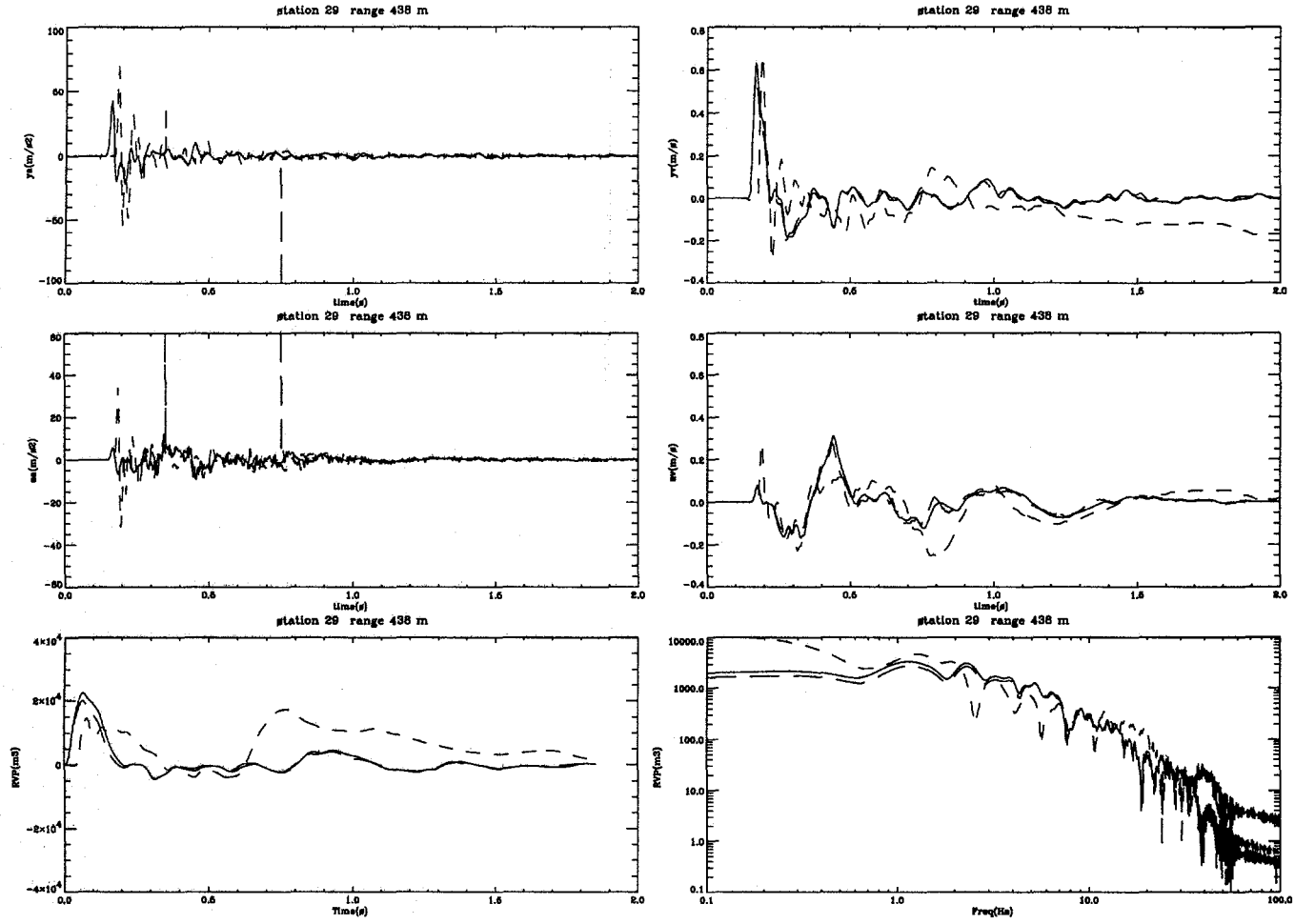

Figure 19: Experimental and computational free-field results at 438 m. Shown are the radial acceleration (m/s^2), radial velocity (m/s), vertical acceleration (m/s^2), and vertical velocity (m/s) vs. time (s), RVP (m^3/s) vs. reduced time (s), and RVP spectrum (m^3) vs. frequency (Hz) at shot depth and 438 m range from the NPE WP. The solid lines denote the CE simulations; the long dashed lines represent the NE simulations; the short dashed line represents the NPE data collected by LANL P-15 [21], gage TM8.

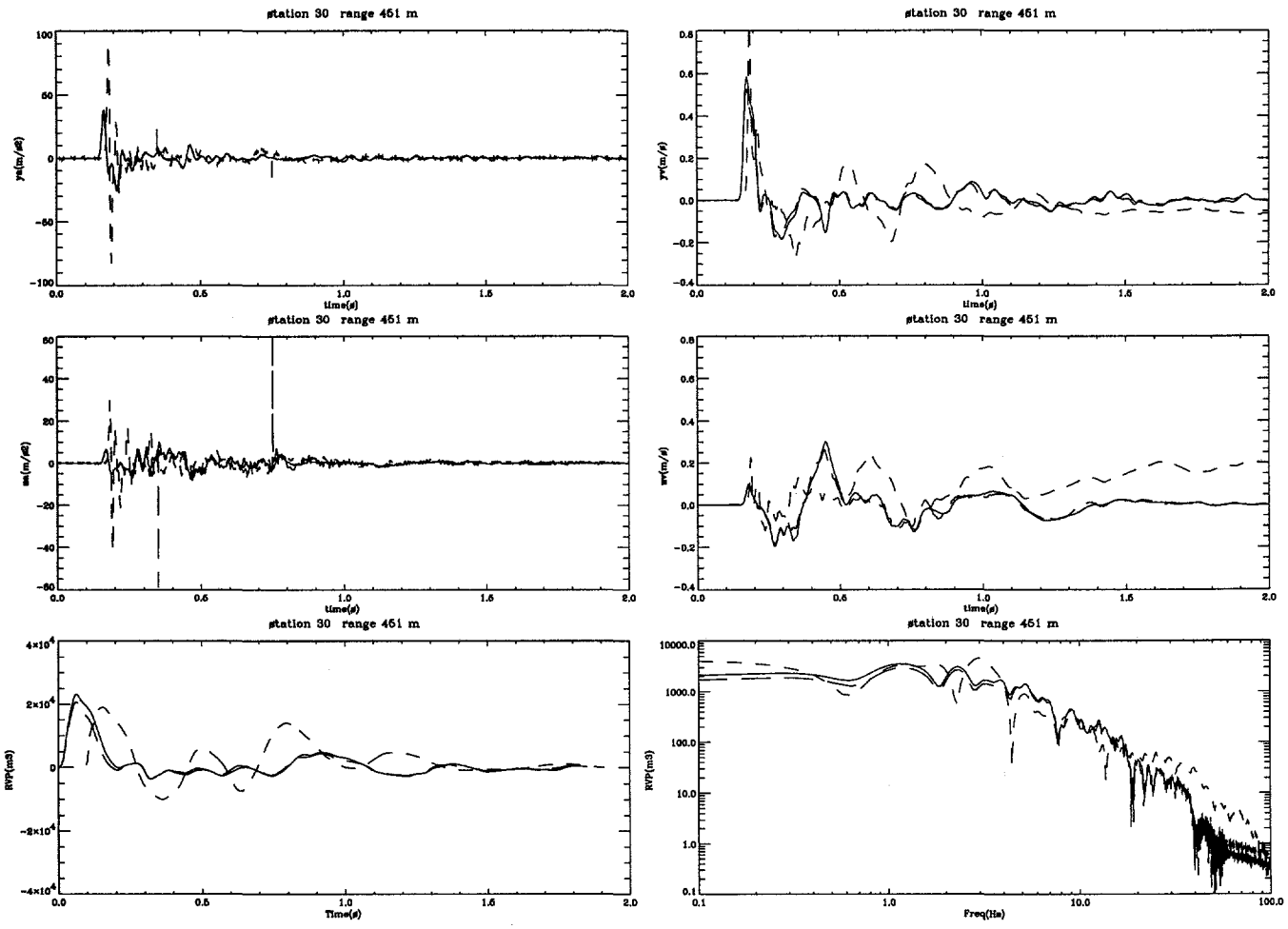

Figure 20: Experimental and computational free-field results at 451 m. Shown are the radial acceleration (m/s^2), radial velocity (m/s), vertical acceleration (m/s^2), and vertical velocity (m/s) vs. time (s), RVP (m^3/s) vs. reduced time (s), and RVP spectrum (m^3) vs. frequency (Hz) at shot depth and 451 m range from the NPE WP. The solid lines denote the CE simulations; the long dashed lines represent the NE simulations; the short dashed line represents the NPE data collected by LANL P-15 [21], gage TM25.

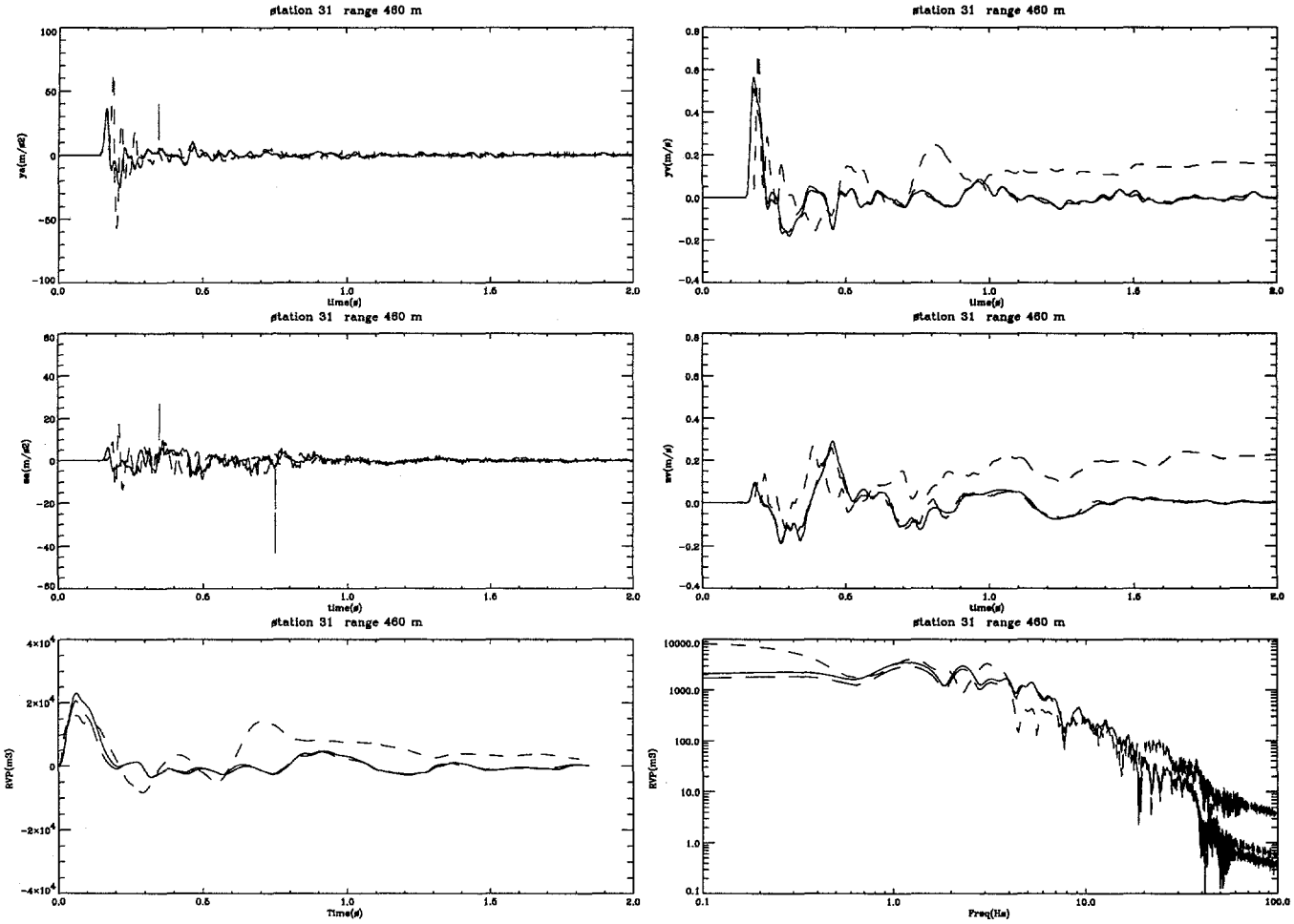

Figure 21: Experimental and computational free-field results at 460 m. Shown are the radial acceleration (m/s^2), radial velocity (m/s), vertical acceleration (m/s^2), and vertical velocity (m/s) vs. time (s), RVP (m^3/s) vs. reduced time (s), and RVP spectrum (m^3) vs. frequency (Hz) at shot depth and 460 m range from the NPE WP. The solid lines denote the CE simulations; the long dashed lines represent the NE simulations; the short dashed line represents the NPE data collected by LANL P-15 [21], gage TM13.

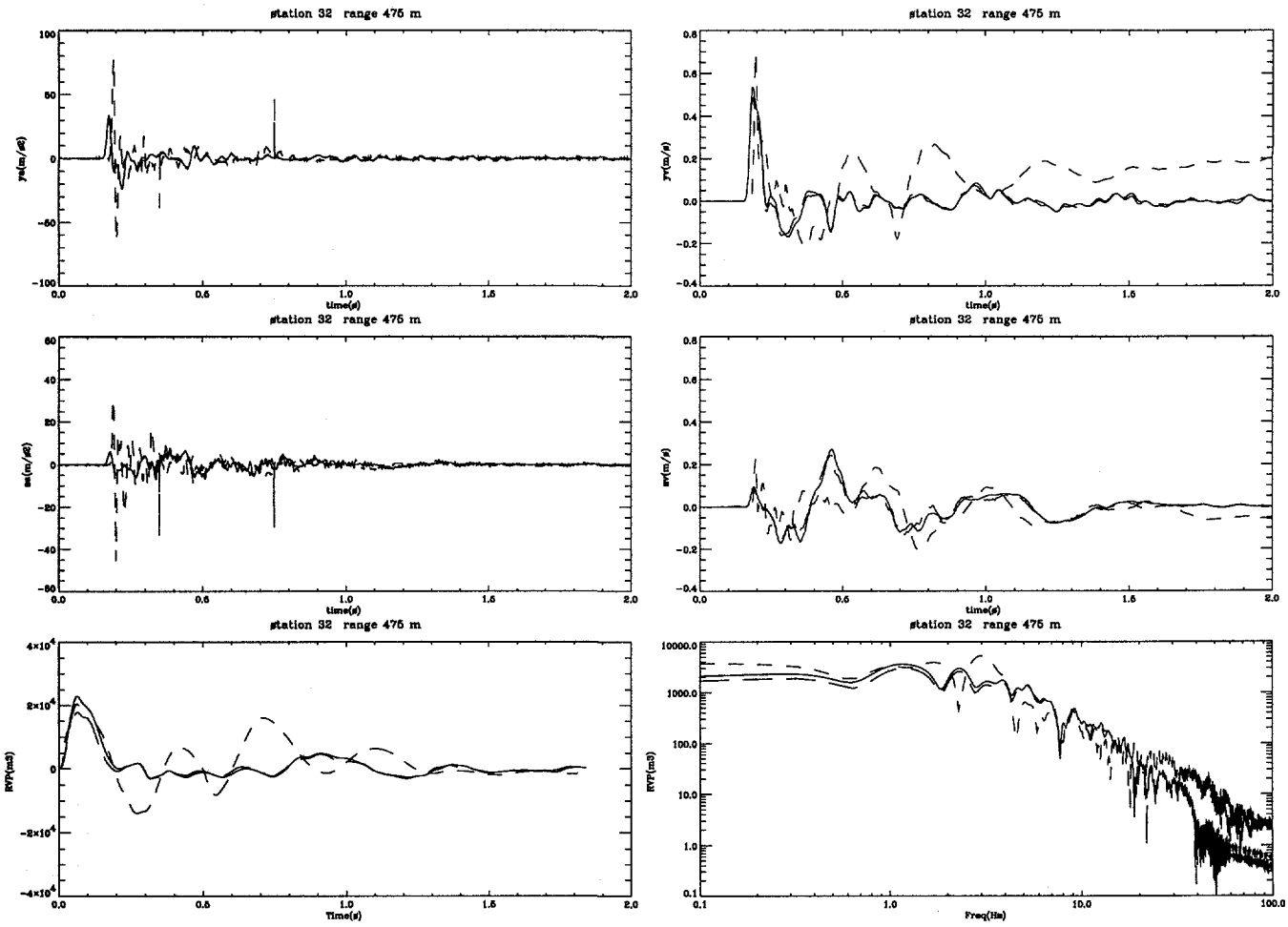

Figure 22: Experimental and computational free-field results at 475 m. Shown are the radial acceleration (m/s^2), radial velocity (m/s), vertical acceleration (m/s^2), and vertical velocity (m/s) vs. time (s), RVP (m^3/s) vs. reduced time (s), and RVP spectrum (m^3) vs. frequency (Hz) at shot depth and 475 m range from the NPE WP. The solid lines denote the CE simulations; the long dashed lines represent the NE simulations; the short dashed line represents the NPE data collected by LANL P-15 [21], gage TM24.

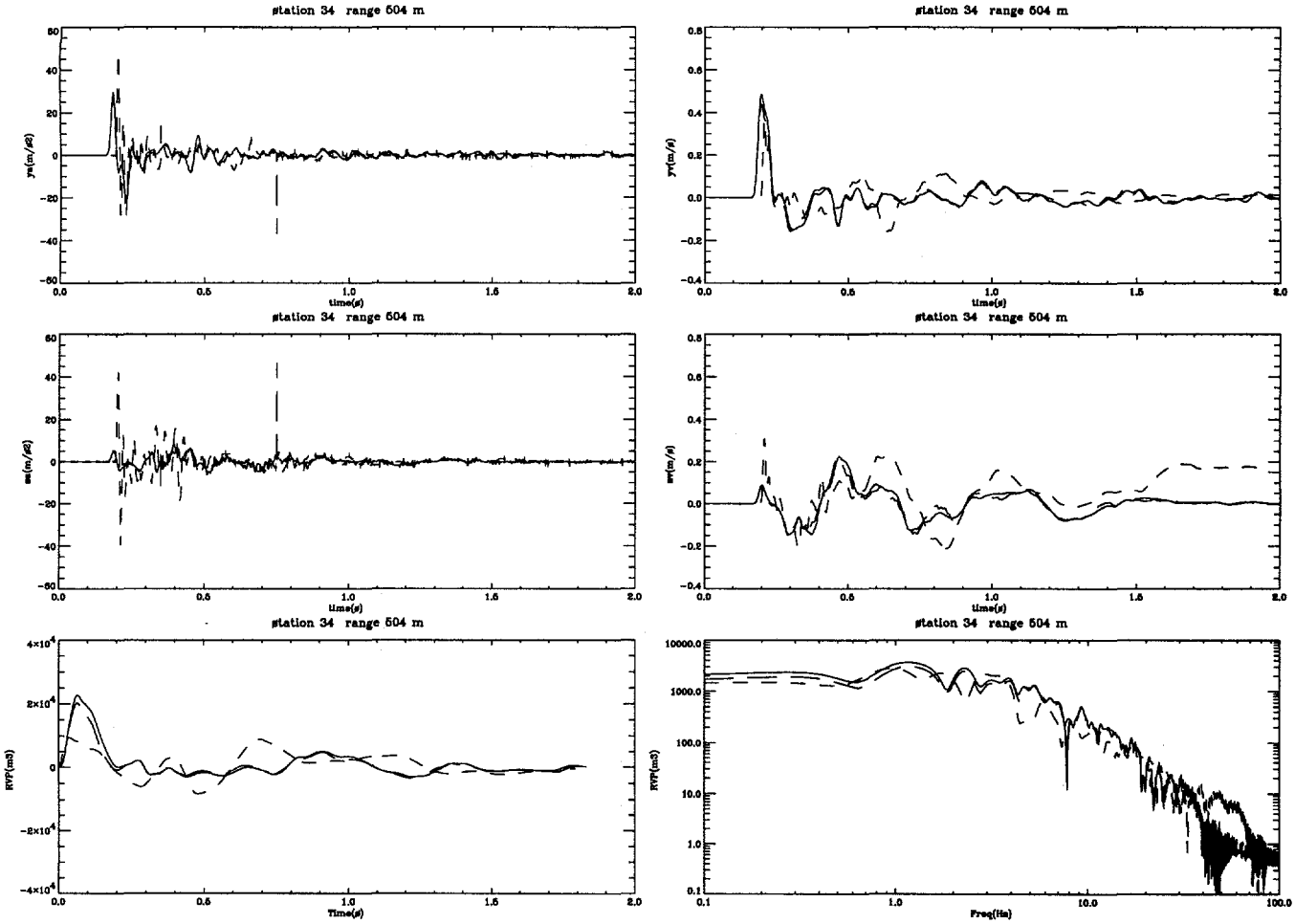

Figure 23: Experimental and computational free-field results at 504 m. Shown are the radial acceleration (m/s^2), radial velocity (m/s), vertical acceleration (m/s^2), and vertical velocity (m/s) vs. time (s), RVP (m^3/s) vs. reduced time (s), and RVP spectrum (m^3) vs. frequency (Hz) at shot depth and 504 m range from the NPE WP. The solid lines denote the CE simulations; the long dashed lines represent the NE simulations; the short dashed line represents the NPE data collected by LANL P-15 [21], gage TM14.

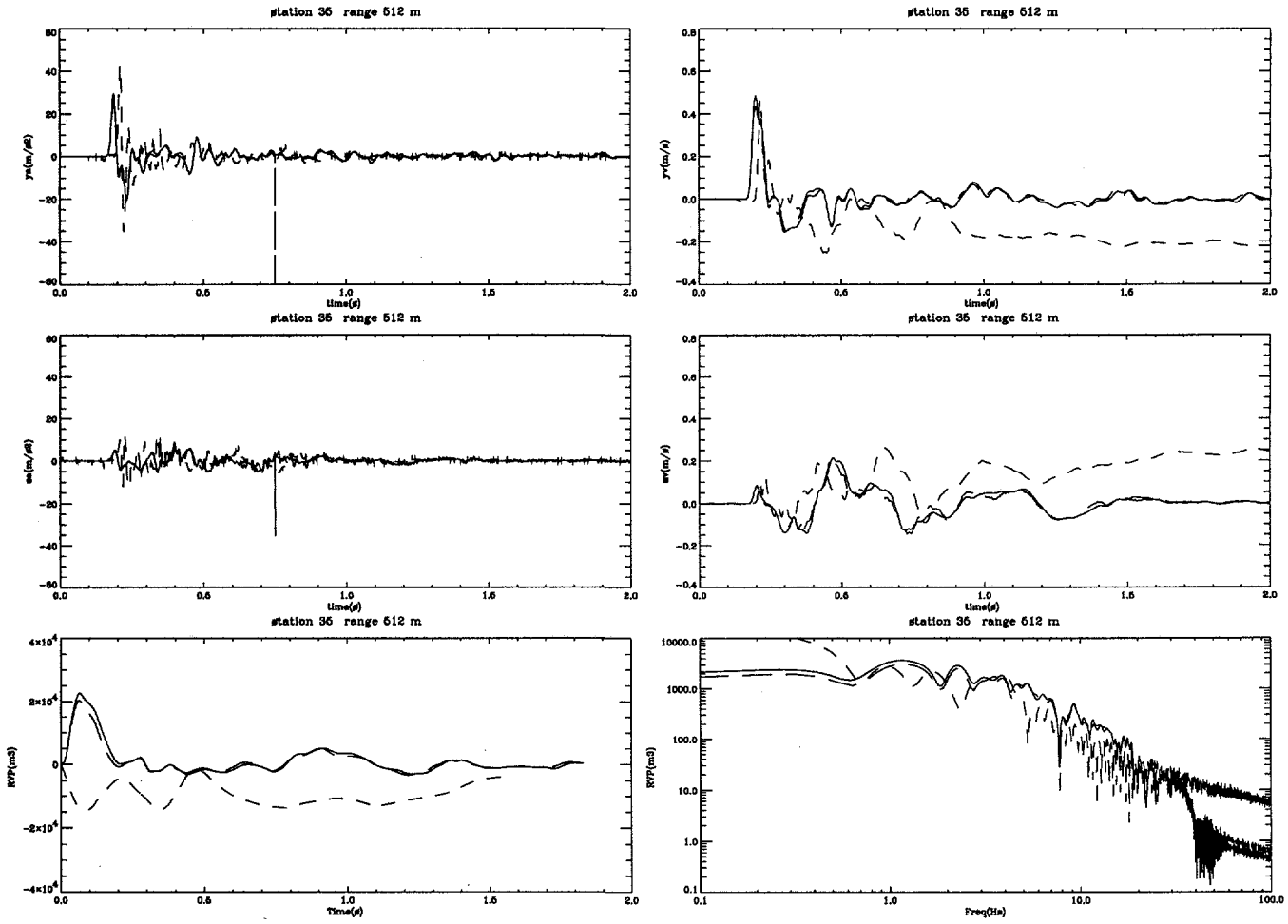

Figure 24: Experimental and computational free-field results at 512 m. Shown are the radial acceleration (m/s^2), radial velocity (m/s), vertical acceleration (m/s^2), and vertical velocity (m/s) vs. time (s), RVP (m^3/s) vs. reduced time (s), and RVP spectrum (m^3) vs. frequency (Hz) at shot depth and 512 m range from the NPE WP. The solid lines denote the CE simulations; the long dashed lines represent the NE simulations; the short dashed line represents the NPE data collected by LANL P-15 [21], gage TM1.

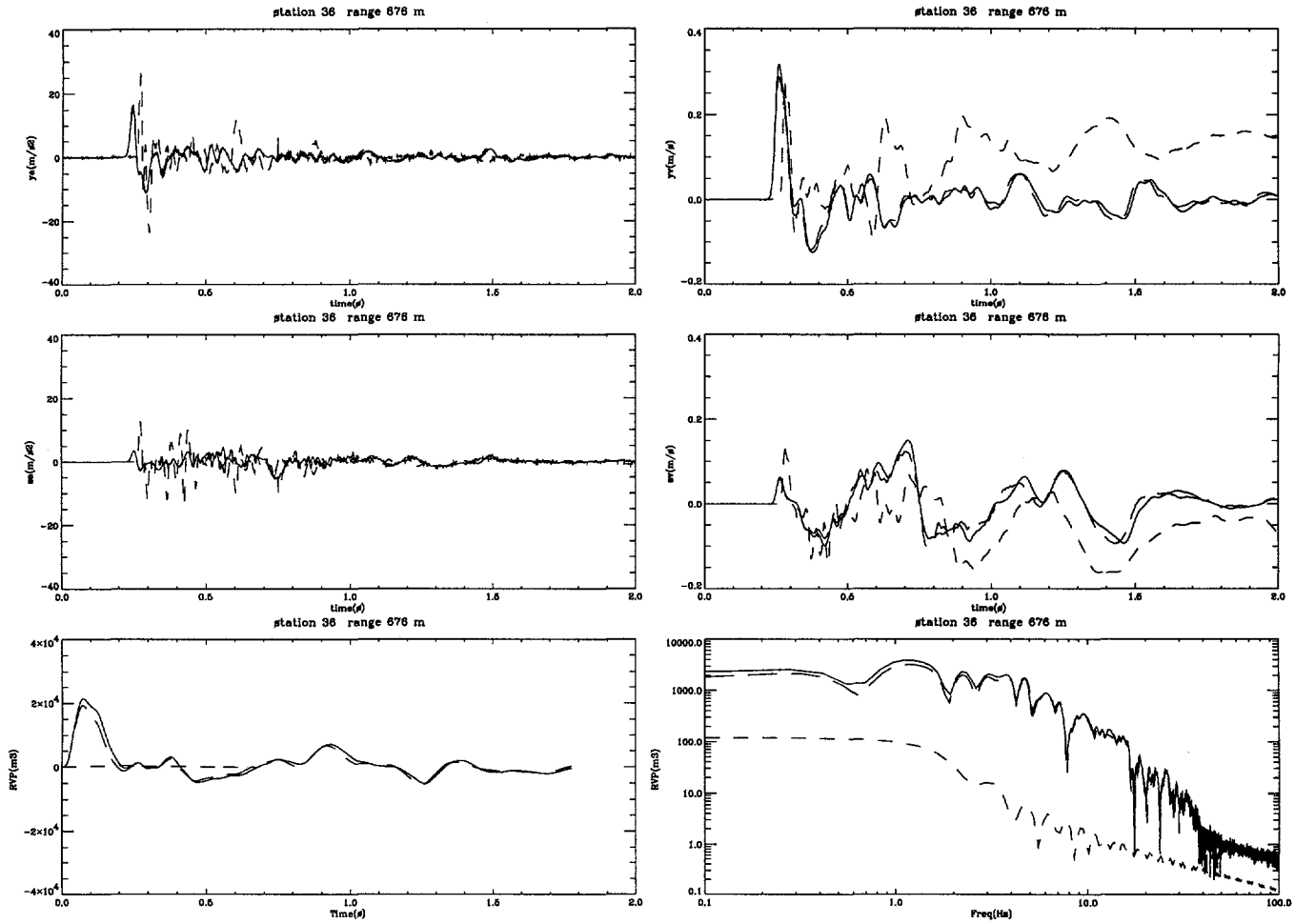

Figure 25: Experimental and computational free-field results at 676 m. Shown are the radial acceleration (m/s^2), radial velocity (m/s), vertical acceleration (m/s^2), and vertical velocity (m/s) vs. time (s), RVP (m^3/s) vs. reduced time (s), and RVP spectrum (m^3) vs. frequency (Hz) at shot depth and 676 m range from the NPE WP. The solid lines denote the CE simulations; the long dashed lines represent the NE simulations; the short dashed line represents the NPE data collected by LANL P-15 [21], gage TM10.

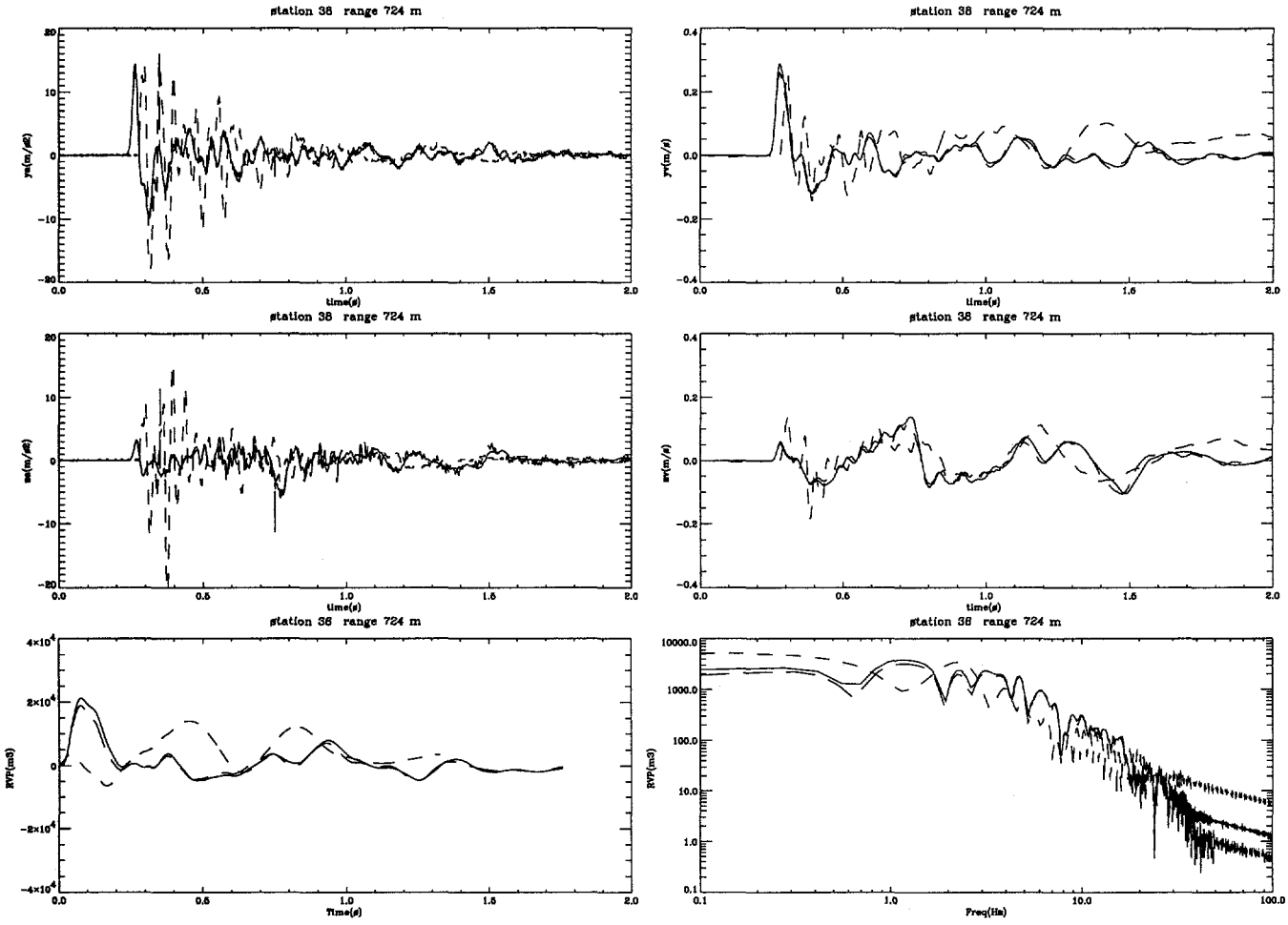

Figure 26: Experimental and computational free-field results at 724 m. Shown are the radial acceleration (m/s^2), radial velocity (m/s), vertical acceleration (m/s^2), and vertical velocity (m/s) vs. time (s), RVP (m^3/s) vs. reduced time (s), and RVP spectrum (m^3) vs. frequency (Hz) at shot depth and 724 m range from the NPE WP. The solid lines denote the CE simulations; the long dashed lines represent the NE simulations; the short dashed line represents the NPE data collected by LANL P-15 [21], gage TM12.

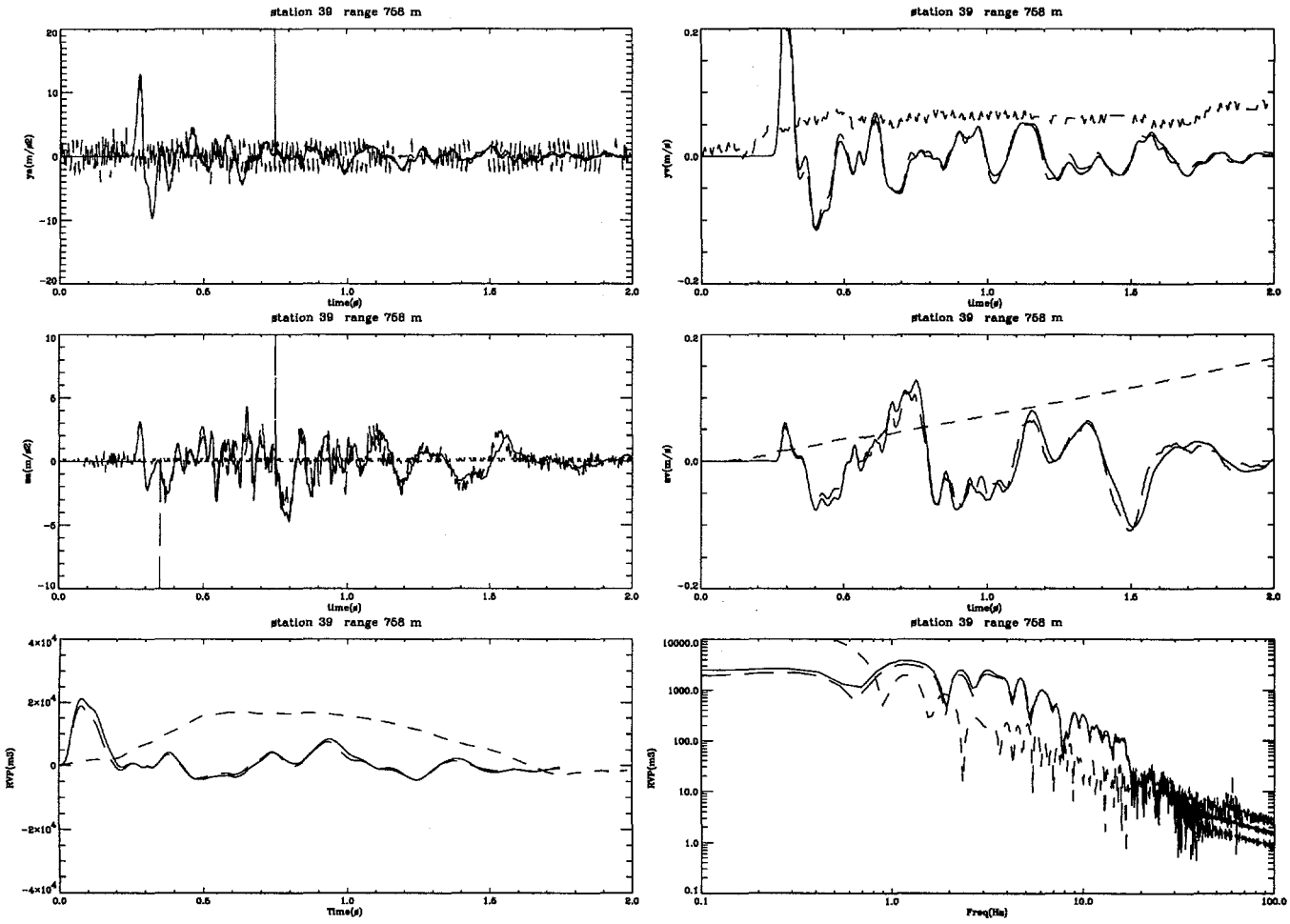

Figure 27: Experimental and computational free-field results at 758 m. Shown are the radial acceleration (m/s^2), radial velocity (m/s), vertical acceleration (m/s^2), and vertical velocity (m/s) vs. time (s), RVP (m^3/s) vs. reduced time (s), and RVP spectrum (m^3) vs. frequency (Hz) at shot depth and 758 m range from the NPE WP. The solid lines denote the CE simulations; the long dashed lines represent the NE simulations; the short dashed line represents the NPE data collected by LANL P-15 [21], gage TM11. Although the data at this station appear irreparably damaged, we include them for completeness.

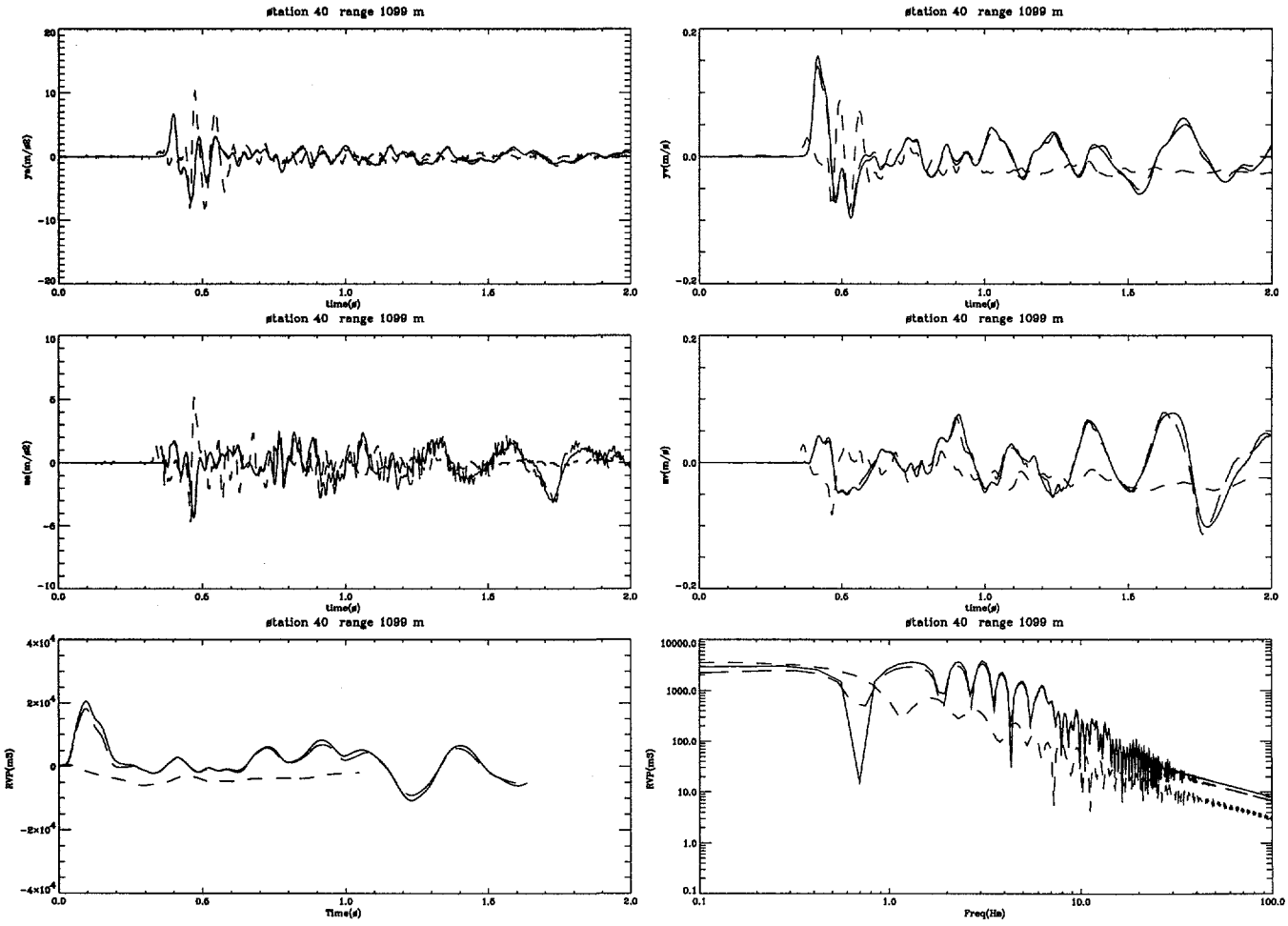

Figure 28: Experimental and computational free-field results at 1099 m. Shown are the radial acceleration (m/s^2), radial velocity (m/s), vertical acceleration (m/s^2), and vertical velocity (m/s) vs. time (s), RVP (m^3/s) vs. reduced time (s), and RVP spectrum (m^3) vs. frequency (Hz) at shot depth and 1099 m range from the NPE WP. The solid lines denote the CE simulations; the long dashed lines represent the NE simulations; the short dashed line represents the NPE data collected by LANL P-15 [21], gage TM15.

stations greater than 100 m from the WP, but the traces have *not* been normalized (demonstrating primarily the geometric divergence effect on amplitudes).

Comparisons of these waveforms with those of a CE calculation in which the layering was omitted and the WP Tt4 unit assumed throughout the entire geologic medium, suggest, as expected, that material layering has a relatively small effect on the radial signal near the source, while certain waveform features vertically near the source and both radially and vertically at greater ranges are probably related to the layered lithology. Shown in Figs. 31 and 32 are plots of the radial (left) and vertical (right) velocity (m/s) vs. time (s) for the layered geology CE simulation (solid lines), the uniform geology CE simulation (long dashed lines), and the experimental data (short dashed line) at selected free-field stations between 70 m and 724 m range. The radial velocity plots in Fig. 31 show negligible differences between the uniform and layered cases at 70 m, but a small yet significant difference at 191 m and 228 m: the post-initial-peak "plateau" evident in the data and the layered calculation is not present in the uniform calculation, suggesting that this feature is related to wave reflection (probably from the nearby dissimilar Tt5 unit above). The vertical velocity plots in Fig. 31 exhibit, as expected, little structure in the uniform calculation when compared to either the layered calculation or the experimental data. The stations farther out, shown in Fig. 32 show that the peak radial velocity values for the uniform calculation are ~25% greater than those of either the layered calculation or data, i.e., that layering acts (in this case) to attenuate the radial signal. Furthermore, this figure demonstrates that layering has significant effects out to the latest time of the simulations (and, presumably, to later times): both radial and vertical velocity in the uniform calculation are relatively flat beyond ~1 s, beyond which the experimental data and layered calculation continue to exhibit significant structure.

As shown in Figs. 12–28, we have used the experimental data and computed results to compute the seismic source function. As derived and discussed by, e.g., Denny and Johnson [24] and examined, via numerical simulation of various materials, by App [25] and Cherry *et al.* [26], the seismic source function provides a low-dimensional model characterization of elastic wave propagation from explosion sources. Assuming perfectly elastic material response, the reduced displacement potential (RDP), denoted ψ, satisfies the spherical P-wave equation, and can be computed from the radial displacement values as a function of the reduced time $\tau \equiv t - (r - R_c)/c_\ell > 0$, where R_c is a location beyond the elastic radius and c_ℓ is the longitudinal elastic wave speed. The reduced velocity potential (RVP), denoted ϕ, is the reduced-time derivative of the RDP and can be computed from the radial velocity data; following the work of many others, we also consider the Fourier spectrum of the RVP.

The characteristics of the RVP we consider are: the zero-frequency RVP spectrum value, which equals the final (i.e., $\tau \to \infty$) value of the RDP and is denoted ψ_∞ ([L^3]); the RVP spectrum overshoot, $\delta\widetilde{\phi}$ ([L^3]); the RVP spectrum

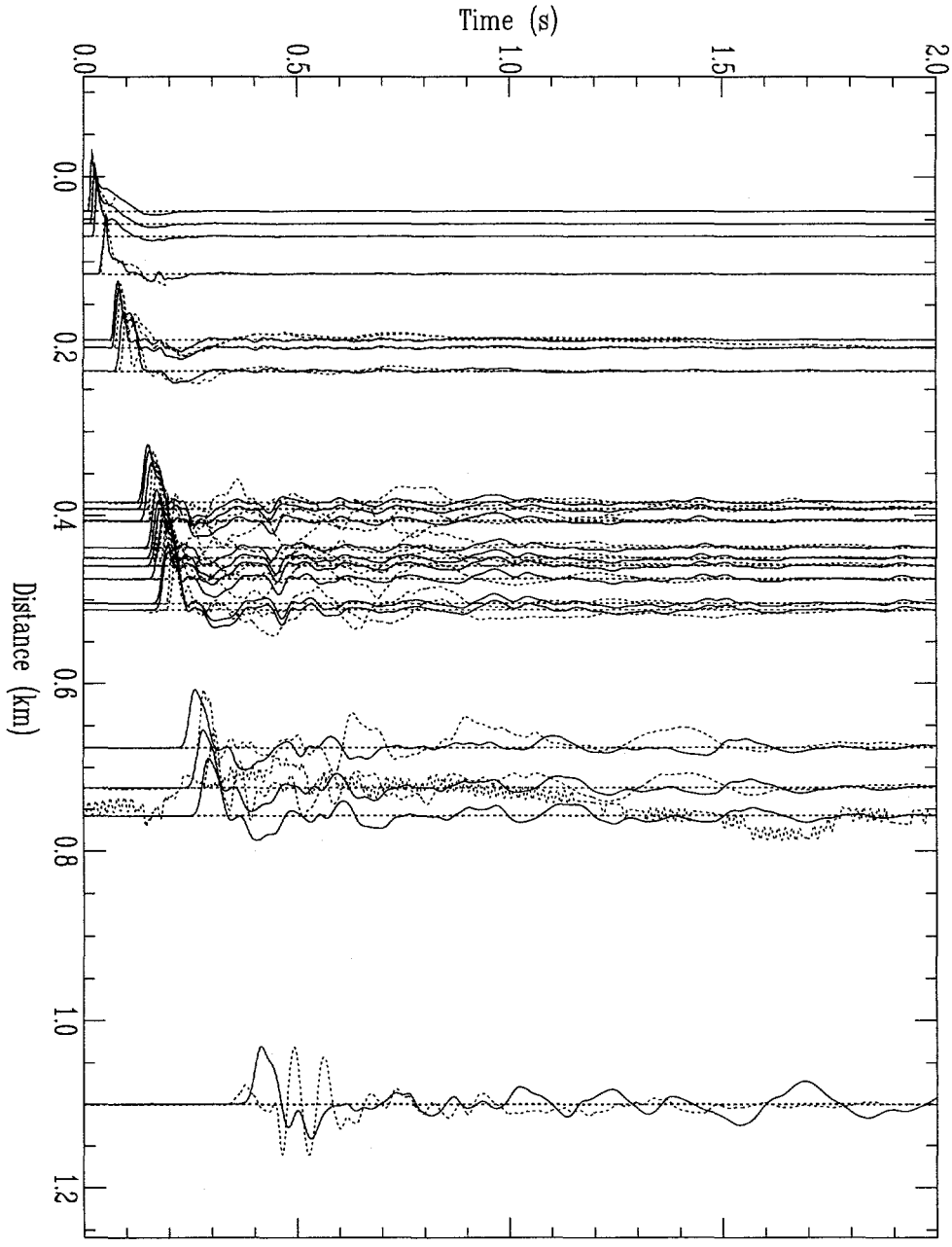

Figure 29: Record section plot of normalized free-field radial velocity (m/s) vs. time (s) at shot depth for the NPE. The solid lines denote the CE simulations and the dotted line represents the NPE data collected by LANL P-15 [21] and SNLA [22].

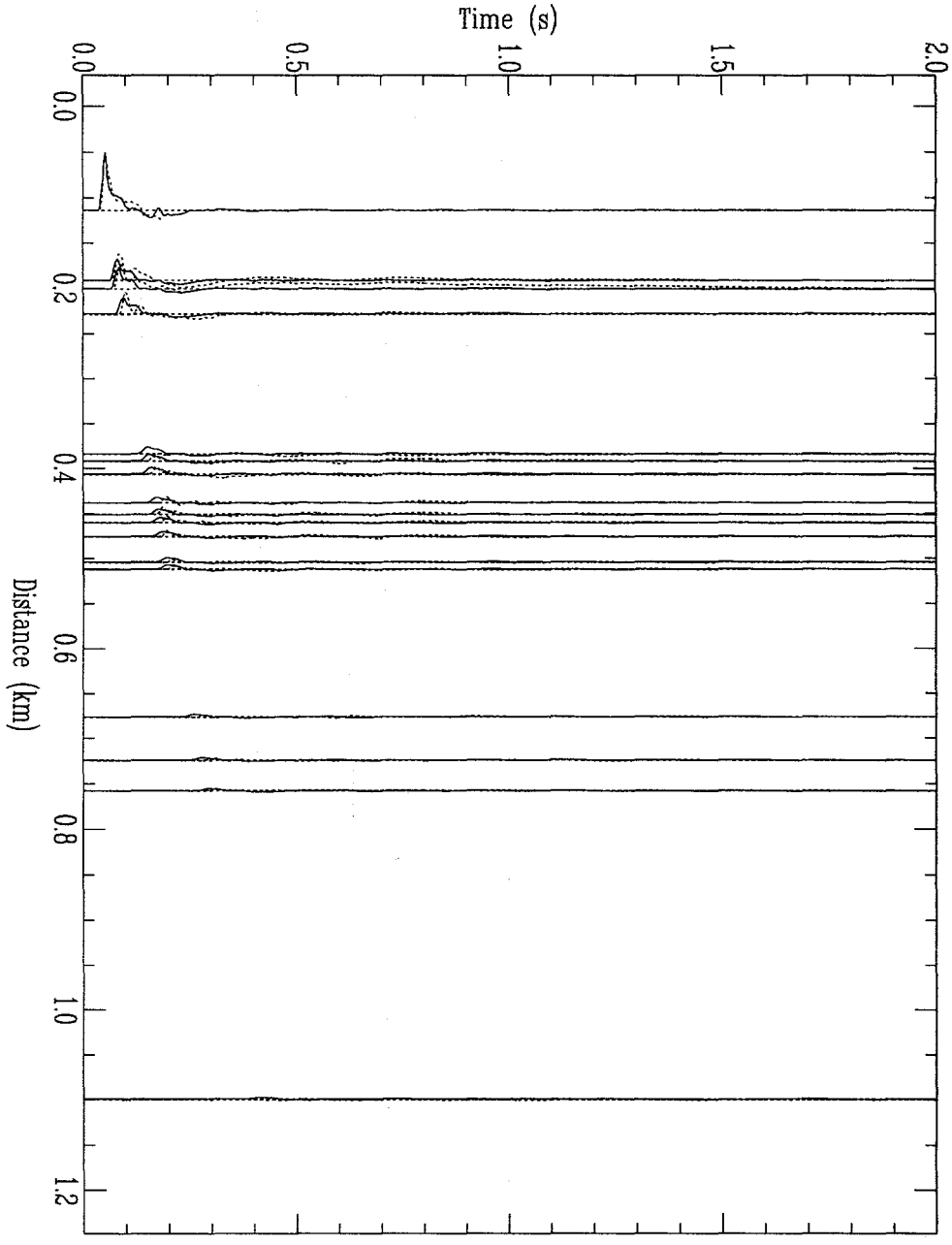

Figure 30: Record section plot of unnormalized free-field radial velocity (m/s) vs. time (s) at shot depth for the NPE. The solid lines denote the CE simulations and the dotted line represents the NPE data collected by LANL P-15 [21] and SNLA [22]. Only stations at ranges greater than 100 m from the WP are included in this plot.

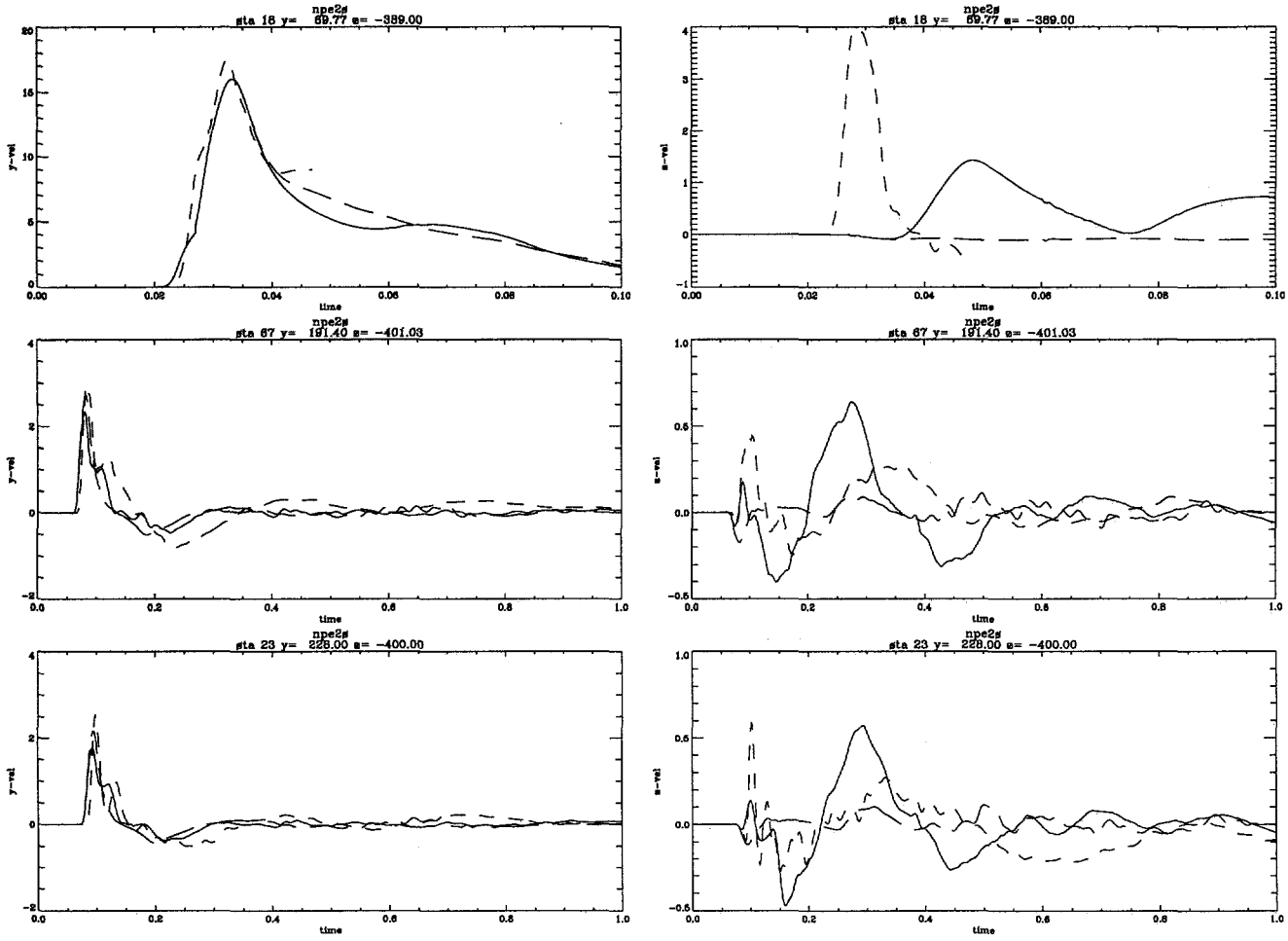

Figure 31: Near source free-field velocities: uniform and layered geologies. Shown are the radial (left) and vertical (right) velocity (m/s) vs. time (s) at shot depth for ranges of 70 m, 191 m, and 228 m from the NPE WP. The solid lines denote the layered geology CE simulations; the long dashed lines represent the uniform WP geology CE simulations; the short dashed line represents the NPE data collected by LANL P-15 [21] and SNLA [22]. The significant differences exhibited in the vertical velocity traces are presumably a manifestation of layering effects. Similarly, the post-initial-peak "plateau" in radial velocity evident in the experimental data and layered calculation at 191 m and 228 m is probably related to layering, as this structure is not present in the uniform calculation.

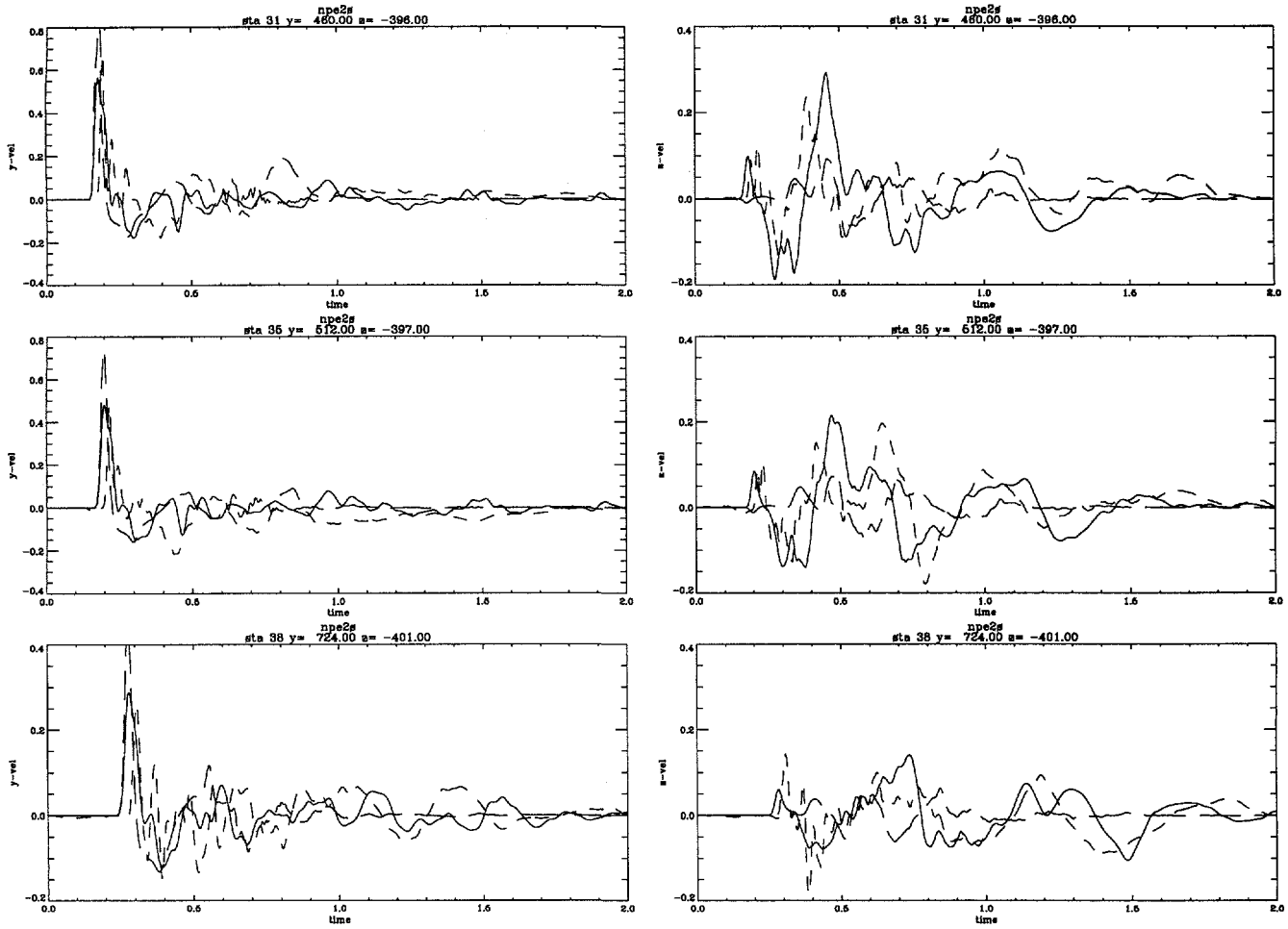

Figure 32: Moderate range free-field velocities: uniform and layered geologies. Shown are the radial (left) and vertical (right) velocity (m/s) vs. time (s) at shot depth for ranges of 460 m, 512 m, and 724 m from the NPE WP. The solid lines denote the layered geology CE simulations; the long dashed lines represent the uniform WP geology CE simulations; the short dashed line represents the NPE data collected by LANL P-15 [21]. The uniform geology calculation contains ~25% higher peak radial velocity values, while the amplitude variation (and, therefore, frequency content) of the vertical velocity for the experimental data and layered calculation is quite dissimilar from that of the uniform calculation, which flattens out beyond ~1 s.

corner frequency, f_c ([T^{-1}]); and the RVP spectrum roll-off, β (dimensionless). The following are physical interpretations of these quantities vis-à-vis explosion sources [27]: ψ_∞ corresponds to the net permanent outward displacement induced by the source; $\delta\widetilde{\phi}$ can be interpreted heuristically as a measure of a damped resonance phenomenon characteristic of the explosion-medium interaction, with materials having high porosity [24] or low shear strength [25] possibly exhibiting greater overshoot; f_c corresponds to a characteristic frequency, on the order of the material sound speed divided by a characteristic length (related, e.g., to a cavity dimension or elastic radius), separating low-frequency ($f < f_c$) from high-frequency ($f > f_c$) phenomena; β, which is the exponent in the decay of the high-frequency asymptote of the RVP spectrum, is a measure of the temporal decay of the radial stress beyond the elastic radius. The reader is referred to the work of Denny and Johnson [24] for a more comprehensive discussion of the explosion seismic source function. These quantities were computed as follows: the RVP is calculated using the velocity information and the assumed WP-material sound velocity; the FFT of this quantity is computed, the zero-frequency value of which yields ψ_∞. The overshoot is obtained as the maximum value of the absolute magnitude of the RVP FFT less ψ_∞. The roll-off is calculated by performing a linear least squares fit, in log-log space, to the absolute magnitude of the RVP FFT on a frequency interval delimited by a fixed maximum frequency (typically 40 Hz) and a RVP-dependent minimum frequency algorithmically located at the highest frequency prior to a downturn in the RVP spectrum; this slope of this fit equals β. The corner frequency is calculated to lie at the intersection of the low-frequency RVP spectrum asymptote (i.e., ψ_∞) and the high-frequency asymptote (determined by β).

Figures 33 and 34 contain plots of the RVP spectrum (m^3) vs. frequency (Hz) for the free-field gage locations. These figures present the results for the CE simulations (left column), NE simulations (middle column), and NPE data (right column). The RVP spectra were computed from the RVP (shown in Figs. 12–28), which are based on 2 s of computed results or 2 s of experimental data. We display the spectral data down to 0.1 Hz, although, with a fixed final time of 2 s, the final reduced time (which varies as a function or range) is less than 2 s; hence, the minimum spectral frequency is greater than 0.5 Hz, which provides possibly incorrect estimates of ψ_∞ and, therefore, of $\delta\widetilde{\phi}$. This early data termination contributes to the spectral scalloping (at frequency-multiples of the inverse final reduced time) evident in some RVP spectra, particularly at greater ranges. The high-frequency ($f \gtrsim 40$ Hz) structure in the RVP spectra is not meaningful: it is a numerical artifact resulting from not tapering the waveforms prior to the spectral calculation.

The experimental RVP spectra (right column in Figs. 33 and 34) exhibit significant scatter. This occurs despite the consistent (albeit brute-force) data analysis technique in which the raw accelerations were demeaned and detrended, and the resulting velocities were linearly detrended by imposing that the veloc-

ity at $t = 2$ s be zero. The variation in ψ_∞ is sufficiently large, for example, that the estimates of $\delta\widetilde{\phi}$ and f_c are highly questionable. The disparity in experimental RVP spectra is due to low-frequency enhancement from systematic signals that we have not removed from the raw data at our disposal. Therefore, we believe that the values obtained in our analysis of the experimental data possess large systematic error bars that we are unable to confidently estimate; a rough approximation of this uncertainty might be twice the scatter in the values computed from the data. Proper analysis of the free-field experimental data requires careful manipulation of each data record, a task beyond the scope of the present investigation, but which would prove worthwhile by providing seismic source parameter estimates of much greater fidelity than those presented herein.

We compile in Table 5 the mean values of ψ_∞, $\delta\widetilde{\phi}$, f_c, and β for the chemical and nuclear source calculations in both layered and uniform geologies, as well as from the free-field data collected outside of the computed elastic radius. As indicated above, the experimental waveforms imply *extremely questionable* source parameter values, as indicated by the large scatter in these results; we believe this effect is due to the suspicious and probably spurious low-frequency content in those records. The value of ψ_∞ from the NPE simulation, 2040 ± 290 m^3, is a factor of $\sim$2.5 greater than the value $\psi_\infty \approx 825$ m^3 found by analysis of the low-frequency data by Patton [28], and a factor of $\sim$1.5 greater than the value $\widetilde{\phi}(0.5\text{ Hz}) \approx 1300$ m^3 obtained by the free-field data analysis of Goldstein & Jarpe [29]; these authors do not provide error estimates, however, so we cannot ascertain if our calculated value falls within their computed experimental uncertainty. As shown in this table, all computations had $f_c \approx 3$–4 Hz, and $\beta \approx -2$. The only property that differs significantly between the layered CE and NE calculations is the mean value of ψ_∞, which is approximately 25% greater for the chemical source. Comparison of mean properties for the layered and uniform CE calculations reveals a nontrivial difference in overshoot values. Heuristically, this result may be understood in terms of a greater "trapping" of energy, near the appropriate characteristic frequency, in the layered calculation.

The variation of the calculated source function properties with range is demonstrated in Fig. 35, which contains plots of computed values of ψ_∞, $\delta\widetilde{\phi}$, f_c, and β as functions of range. This figure shows distinct trends among these parameters not revealed in the simple statistics of Table 5. As shown in Fig. 35, ψ_∞ increases with range and is nearly consistently 25% greater for the chemical source than for the equivalent nuclear source. Also, β and f_c decrease with range, with the latter exhibiting a nearly range-independent difference between the layered and uniform geologies. The behavior of $\delta\widetilde{\phi}$ with range is somewhat curious, and displays a more-or-less consistent difference between layered and uniform geologies. According to 1-D perfectly elastic theory (upon which the source function concept is based [24]), these properties should be independent of range beyond the elastic radius, which is approximately 150 m according to the calculations (see Table 6). This figure clearly suggests that the 1-D perfectly

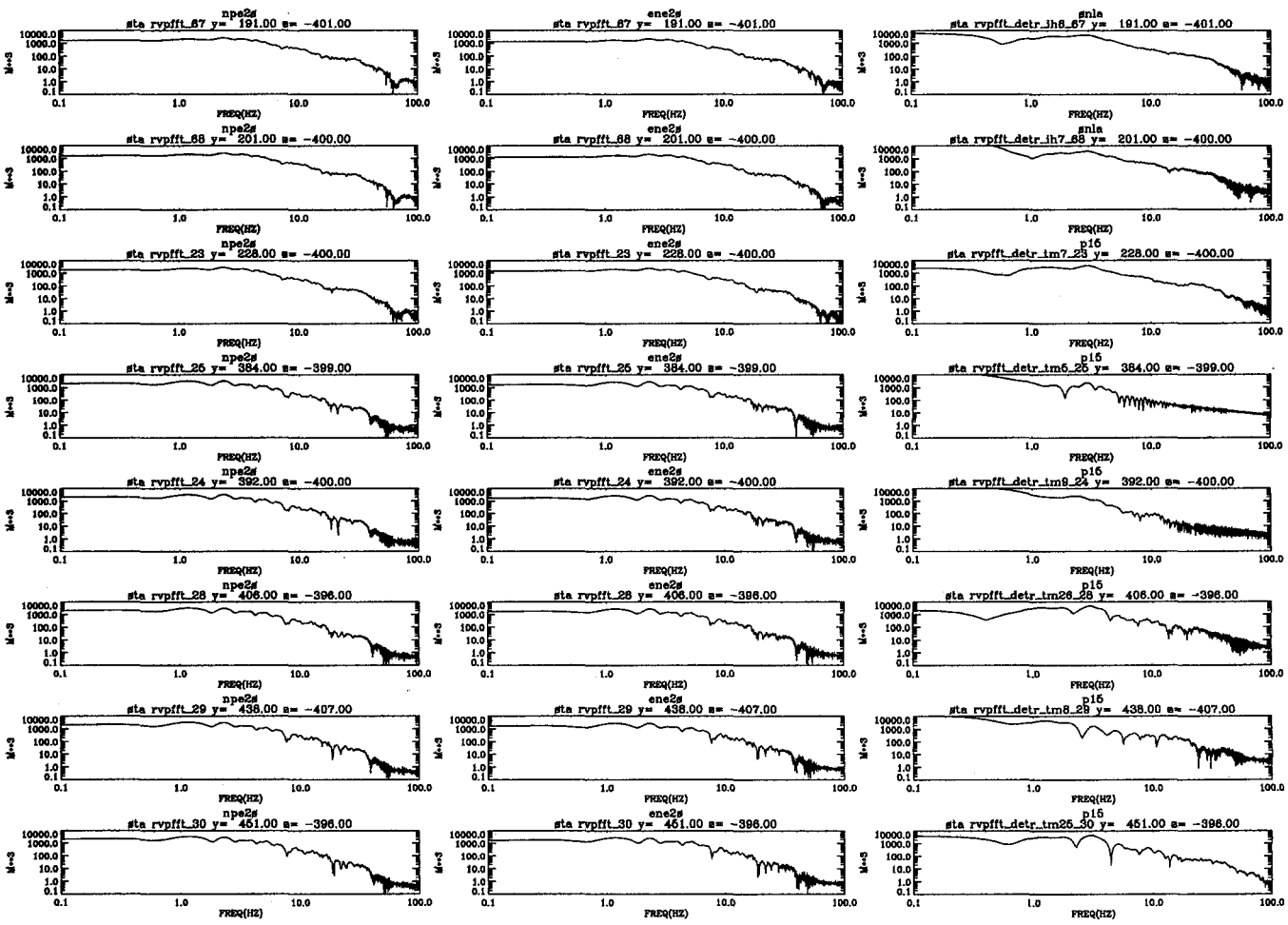

Figure 33: Near source free-field RVP spectra. The computed reduced velocity potential spectra (m^3) are plotted against frequency (Hz) at near source free-field locations beyond the elastic radius. The left column contains the CE simulation results; the middle column contains the NE simulation results; the right column contains the NPE data [21, 22] results.

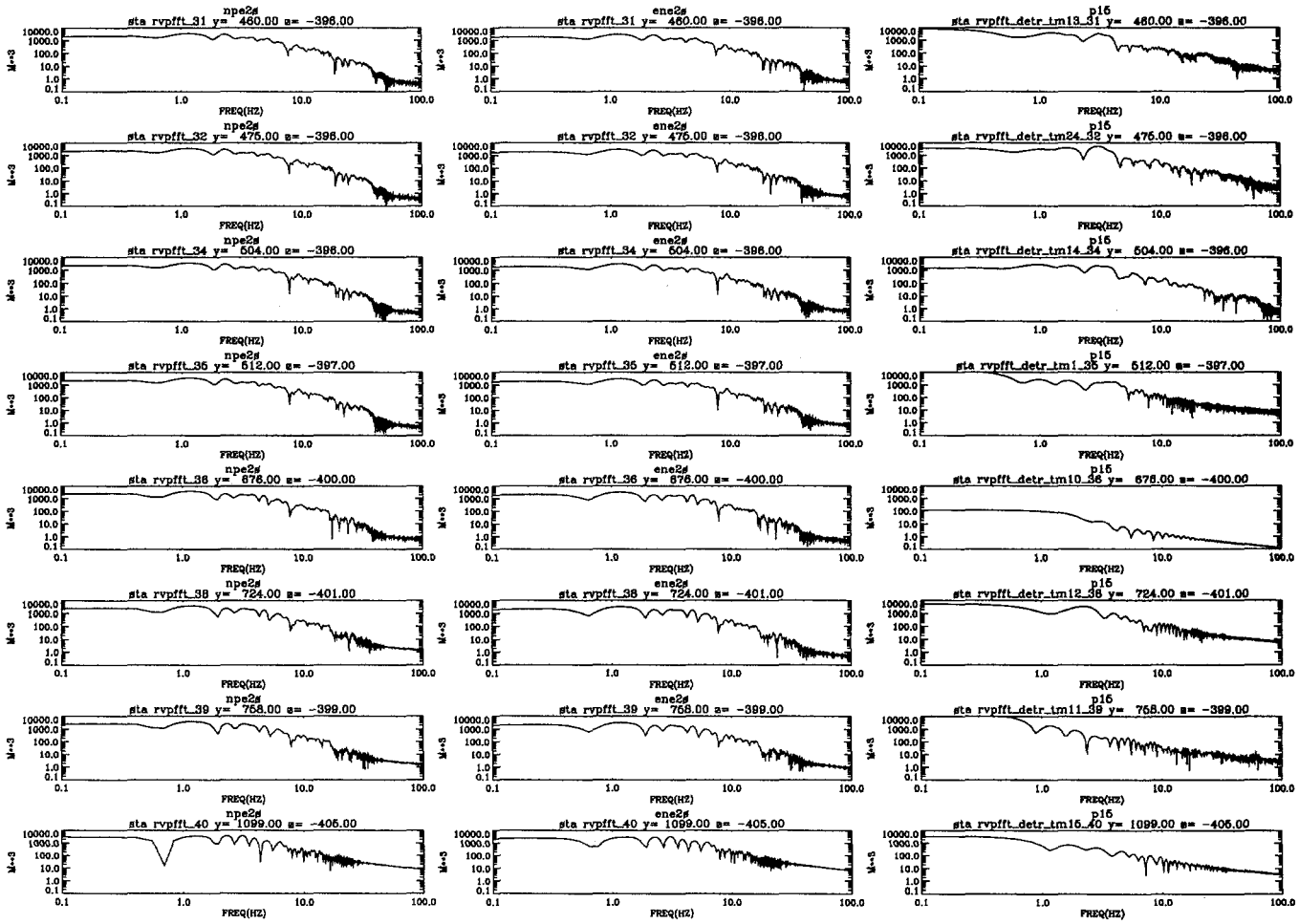

Figure 34: Moderate range free-field RVP spectra. The computed reduced velocity potential spectra (m^3) are plotted against frequency (Hz) at moderate range free-field locations beyond the elastic radius. The left column contains the CE simulation results; the middle column contains the NE simulation results; the right column contains the NPE data [21] results.

Computed Source Function Properties from the NPE Simulations

	CE-L	NE-L	CE-U	Exp.(2s)
ψ_∞ (m^3)	2040±290	1620±200	1840±290	⟨8550±7250⟩
$\delta\widetilde{\phi}$ (m^3)	1380±240	1270±180	400±290	⟨420±740⟩
f_c (Hz)	3.29±0.39	3.53±0.48	4.14±0.25	⟨1.48±0.73⟩
β	-1.96±0.13	-1.93±0.12	-2.00±0.16	⟨-1.47±0.09⟩

Table 5: Listed are the final value of the RDP ψ_∞ (m^3), the RVP spectrum overshoot $\delta\widetilde{\phi}$ (m^3), the RVP spectrum corner frequency f_c (Hz), and the RVP spectrum roll-off β computed from the 2 s simulations of chemical (CE) and nuclear (NE) explosions in 2-D uniform (U) and layered (L) configurations, as well as values calculated from 2 s of experimental data. The numbers given are mean values with one standard deviation bounds. The values for ψ_∞ and $\delta\phi$ are suspect, insofar as they were calculated with only 2 s waveforms. Also, all values cited for the experimental data are ⟨bracketed⟩ to indicate that they are *highly questionable*, since they were computed from waveforms that we believe contained nonphysical low-frequency signals.

elastic assumption is inadequate in the near-source ($\lesssim$1 km range) region, even for the uniform geology (i.e., working point material only) calculation.

The peak WP-level radial velocity (m/s) vs. range (m) is shown in Figure 36, in which data at experimental stations are denoted by ⊗ connected with a dotted line; also shown in this log-log plot are results from the CE simulation (solid line) and the NE simulation (dashed line), and values provided by the Perret & Bass scaling relations [30] for wet tuff (dash-dot line). Both calculations are close to the experimental data, which tend to be somewhat greater than the Perret & Bass results. The "break" in the calculated curves at ~150 m corresponds to the elastic radius. The fall-off of the data beyond this range is notably greater than that of the simulations; possible explanations for this discrepancy include 3-D effects (as observed by Olsen & Peratt [23]) as well as the possibility that the working-point tuff material model may not have been sufficiently dissipative.

The peak WP-level pressure (GPa) vs. range (m) is shown in Figure 37, in which the values at the three SNLA stations are indicated by ⊗ connected by the dotted line; also shown in this plot are the values from the CE simulation (solid line) and the NE simulation (dashed line). This plot shows that the calculated results compare favorably to the few experimental data points, and illustrates one aspect of the near-source difference between chemical and nuclear sources: the peak pressure is nearly constant within the CE source (i.e., at ranges less than 7.6 m), while the peak pressure for the NE source is a monotonically decreasing function of range. Beyond a range of ~20 m, there is little difference between the peak pressure for the CE and NE simulations. Figure 38 depicts the pressure (GPa) as a function of time (s) at a point initially located 1.5 m from the cavity centerline, on log-log scales (upper plot) and semi-log scales (lower

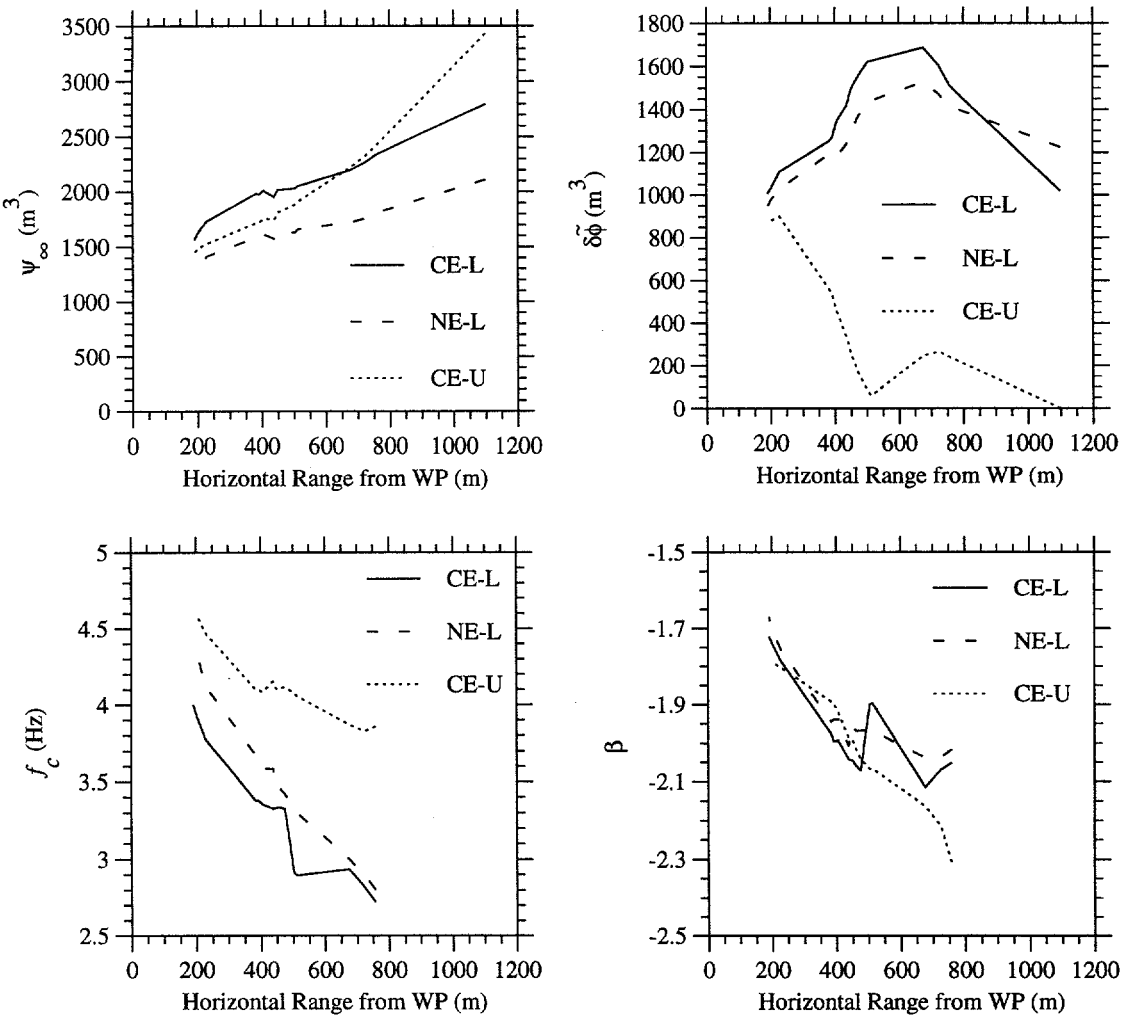

Figure 35: Computed free-field seismic source function parameters vs. range (m) at locations beyond the elastic radius. Clockwise from the upper left, these plots are of the final RDP value ψ_∞ (m^3), the RVP spectrum overshoot $\delta\tilde{\phi}$ (m^3), the RVP spectrum roll-off β, and the RVP spectrum corner frequency f_c (Hz) for the layered CE simulation (solid line), the layered NE simulation (dashed line), and the uniform CE simulation (dotted line).

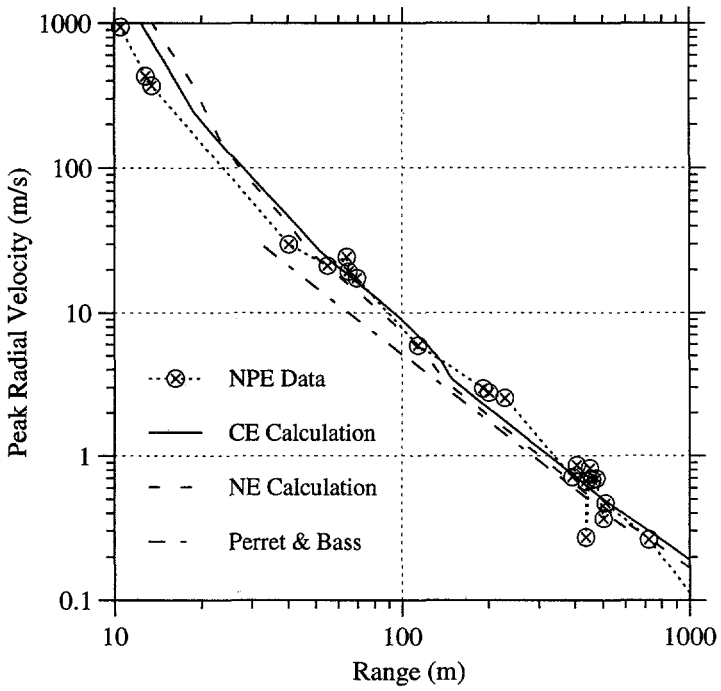

Figure 36: Peak WP-level radial velocity (m/s) vs. range (m) in the plane of the working point. The solid line denotes the CE simulations; the dashed line represents the NE simulations; the dotted line connects values (⊗) inferred from NPE data collected by SNLA [18, 22] and LANL P-15 [21] accelerometers and LANL P-15 ASM gages [17]; the dash-dot (– - –) line represents the Perret & Bass scaling relations [30] for wet tuff. Both calculations fall close to the data, which tend to be somewhat greater than the Perret & Bass scaling curve.

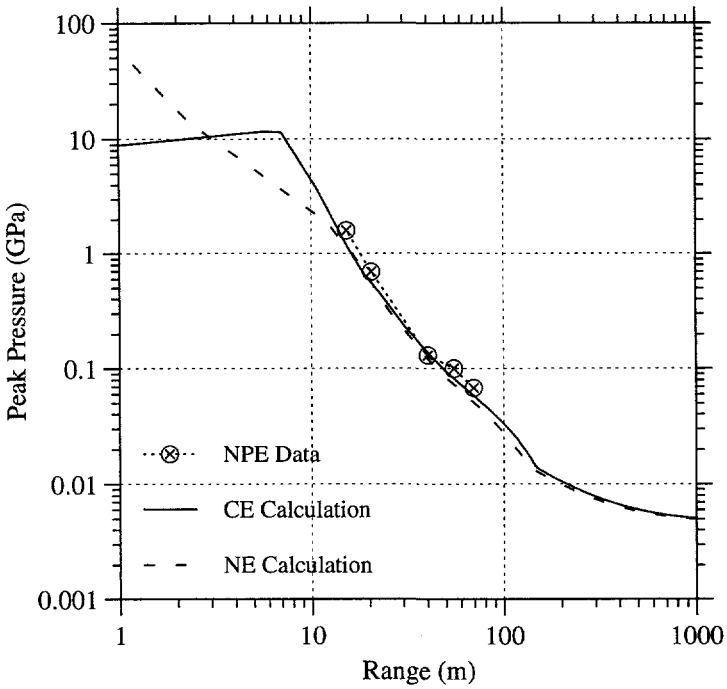

Figure 37: Peak WP-level pressure (GPa) vs. range (m) in the plane of the working point. The solid line denotes the CE simulations; the dashed line represents the NE simulations; the dotted line connects values (⊗) inferred from NPE data collected by SNLA [18]. The data at the two closest ranges are peak radial stresses, which should be approximately equal to the peak pressures at these ranges [19] (i.e., assuming $\sigma_{rr} \approx \sigma_{zz} \approx \sigma_{\theta\theta}$). This plot clearly illustrates one aspect of the near-source difference between chemical and nuclear sources.

plot). These plots illustrate the much greater peak pressure from the nuclear source, the finite initiation time of the blasting agent, and the differing late-time variation in cavity pressure. We are suspicious of the slowly decreasing, somewhat low late-time cavity pressure in the NE simulation, and believe this behavior may be due to inaccurate SESAME data in the low pressure, low density regime. For the CE simulation, the early, fast (i.e., $O(1$ ms$)$) oscillations correspond to shock reverberations within the chamber; it is unclear, however, what is associated with the later, slower (i.e., $O(10$ ms$)$) oscillations.

Figure 39 is a plot of the mean cavity radius (m) vs. time (s) for the CE and NE simulations. The CE calculation yields a cavity that is bigger than the NE case, and that attains its final dimension sooner. Table 6 contains values for the computed cavity radii, as well as the cavity radius estimate based on the final value of the RDP, viz., $R_c = \sqrt[3]{3\,\psi_\infty}$ [31], a result that is based on the assumption of an explosively generated cavity in an incompressible, perfectly elastic medium. Also included in this table are values for the computed elastic radius, which is approximated as the WP-level range at which the inelastic shear strain drops below 10^{-5}. For the nuclear source, the value of the computed cavity radius of 16.5 m compares favorably with the estimate used by the nuclear test containment community for nuclear explosions on Rainier Mesa [32], viz., $R_{c,\text{est.}} \approx 16.8\,W^{1/3}$ m ≈ 17.0 m; similarly, the computed nuclear elastic radius of 145 m is close to the nuclear test containment community estimate [32] of $R_{el,\text{est.}} \approx 152\,W^{1/3}$ m ≈ 155 m.

Figure 40 is a plot of the computational mesh for the CE simulation near the cavity at the final time in the simulation. The final cavity, bounded by the interface between the blasting agent detonation products and the surrounding rock, is easily identified in this figure as the nearly semicircular region along the vertical axis. The location of the initial chamber is delineated by the rectangular outline near the center of the cavity. The final cavity is nearly spherical, which is interesting, given the high aspect ratio ($\sim 3:1$) of the emplacement chamber.

Computed Final Cavity Properties from the NPE Simulations

	CE-L	NE-L	CE-U
Max. cavity radius (m)	20.5	19	20
Final cavity radius (m)	19	16.5	18
ψ_∞-Est. cavity radius (m)	18.3	16.9	17.7
Elastic radius (m)	155	145	165

Table 6: Listed are the maximum cavity radius (m), the final cavity radius (m), the ψ_∞-based estimated cavity radius (m), and the elastic radius (m) calculated from the simulations of chemical (CE) and nuclear (NE) explosions in 2-D uniform (U) and layered (L) configurations. The ψ_∞-based estimate is calculated from the computed value of ψ_∞ (see Table 5) and the relation $R_c = \sqrt[3]{3\,\psi_\infty}$ [31].

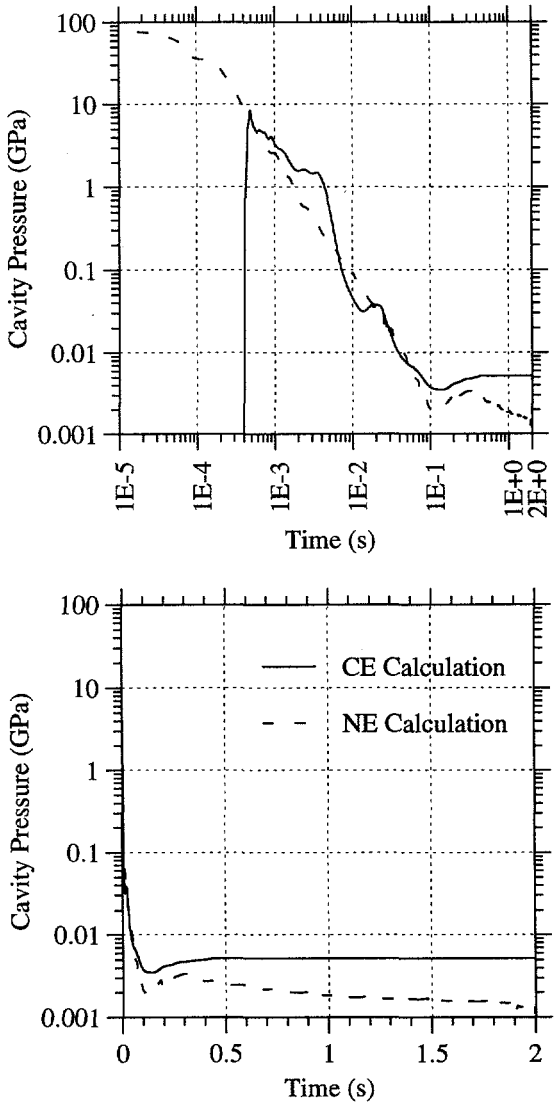

Figure 38: Cavity pressure (GPa) vs. time (s) at a point initially located 1.5 m from the cavity centerline. The upper graph, on log-log scales, demonstrates the early-time differences in cavity pressure between the chemical and nuclear source, while the lower graph, containing the same data on semilog scales, shows the late-time differences.

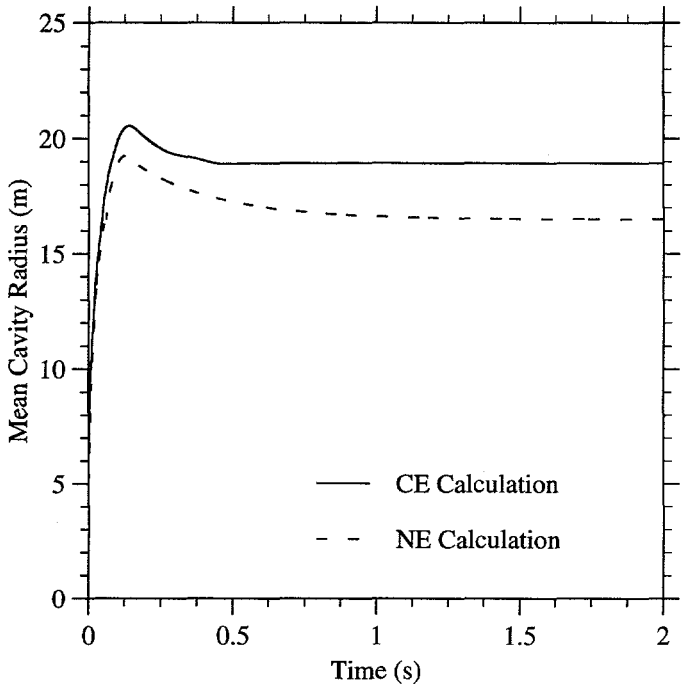

Figure 39: Mean cavity radius (m) vs. time (s). The solid line denotes the CE simulations; the dashed line represents the NE simulations. The cavity radius at 2 s of simulation time is 19 m for the CE calculation, and 16.5 m for the NE calculation.

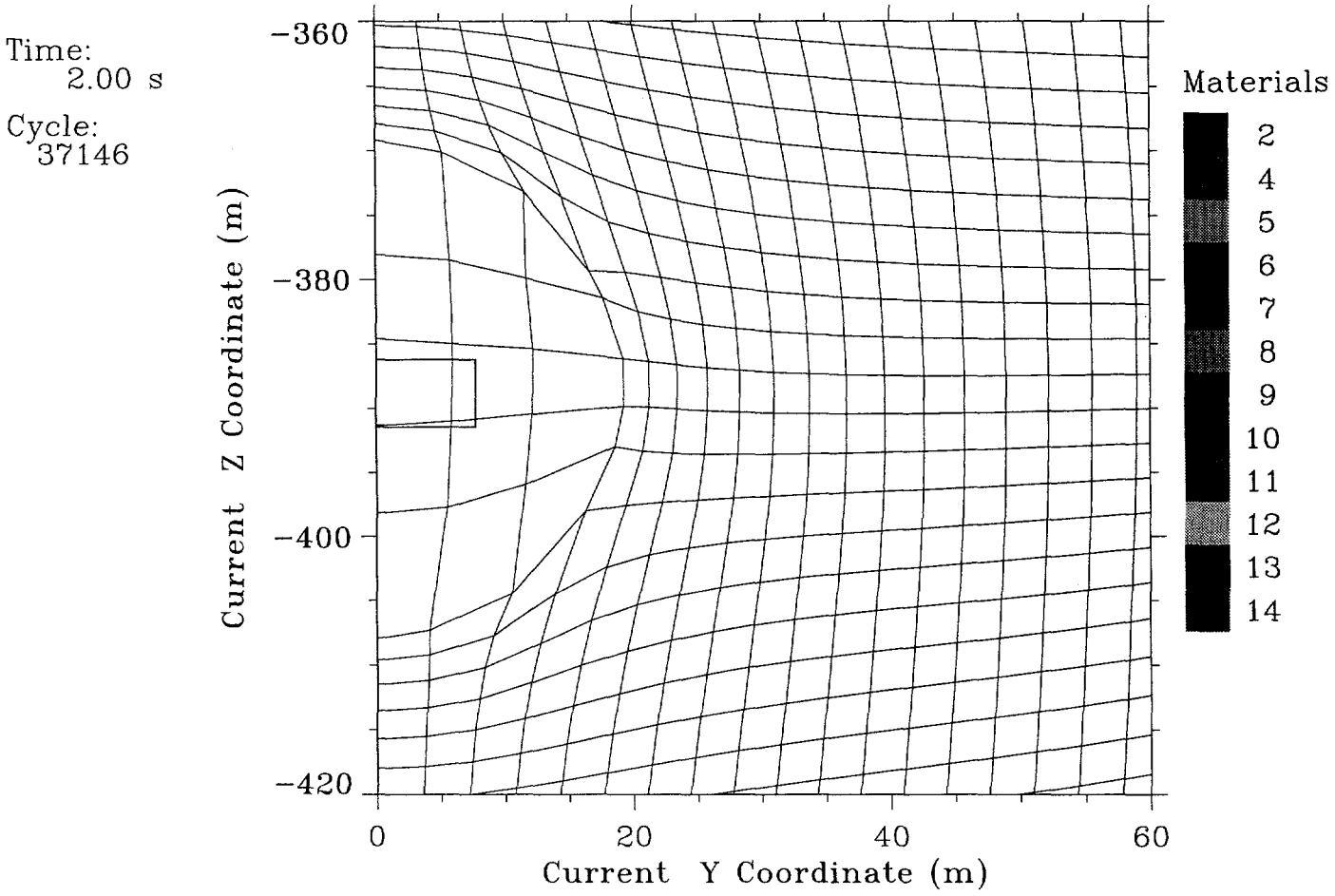

Figure 40: Final cavity (mesh). The final computational mesh is shown in the vicinity of the blasting agent chamber for the CE simulations. The approximately spherical cavity extends from a depth of -408 m to -369 m, and out to a radius of almost 20 m. The blasting agent was initially emplaced in a cylindrical chamber, indicated by the rectangular outline, of height 5.2 m (extending from $z = -391.6$ m to $z = -386.4$ m) and radius 7.6 m; the initial computational mesh had uniform zones of rectilinear dimension 0.1 m.

3.2 Free-Surface Characteristics

The free-surface data are the primary information source for seismic analysis of the NPE and for seismic comparison with nearby nuclear shots. The free-surface data for the NPE range from surface ground zero (SGZ) to teleseismic recording of the event at several thousand km distance (see [1]); we restrict our comparison of calculated waveforms to approximately one km range from SGZ (see Table 4 and Fig. 4).

The material response of free-surface gages is shown in Figures 41–64, in which the data collected by LLNL [33] and LANL EES-3 [34] are compared with the calculated values. These figures contain plots of radial acceleration (m/s^2) vs. time (s), radial velocity (m/s) vs. time (s), vertical acceleration (m/s^2) vs. time (s), and vertical velocity (m/s) vs. time (s) for the actual data (short dashed line), the CE simulation (solid line), and the NE simulation (long dashed line). The collected data are accelerometer records that have been demeaned and integrated to obtain velocities. In these figures, the exact computed results are shown, i.e., they have *not* been time-shifted to match the experimental arrival times.

The calculated ground motion at SGZ, shown in Fig. 41, exhibits nearly ideal spall structure, with spall initiation followed by uniform -1 g free fall and terminated with slapdown; the experimental record, however, shows nonideal behavior manifest in the concave upward vertical velocity trace, which suggests more complicated spall phenomena, perhaps due to the nonuniform surface weathered layer. The calculated spall dwell time is approximately 100 ms greater than the data. Although the magnitude of the computed vertical acceleration at spall initiation is close to that of the experimental records, the calculated vertical slapdown acceleration is notably greater. Additionally, significant post-slapdown "ringing" is evident in the computed results and not present in the experimental data; this is partially due to the greater bandwidth of the computed results (which have not been filtered to the passband of the experimental data). We suspect both of these differences are related primarily to the computational spall model, which allows zones that have exceeded the spall strength (set to 1 bar) to continue expanding at zero pressure, and secondarily to the assumed uniformity of the surface layer model (as opposed to the inhomogeneous *in situ* weathered layer). The radial signals at SGZ are characteristically different, with experimental data exhibiting distinct first pulse and slapdown-like signals and the computed results showing very small first pulse response and subsequent behavior of similar amplitude to (though with greater high-frequency content than) the experimental data. We attribute this difference to the simple spall model, and also to the cylindrical symmetry imposed in the calculation; that the experimental data shows such a noticeable first arrival suggests that the SGZ location may not have been the true first surface arrival point of the initial upgoing wave.

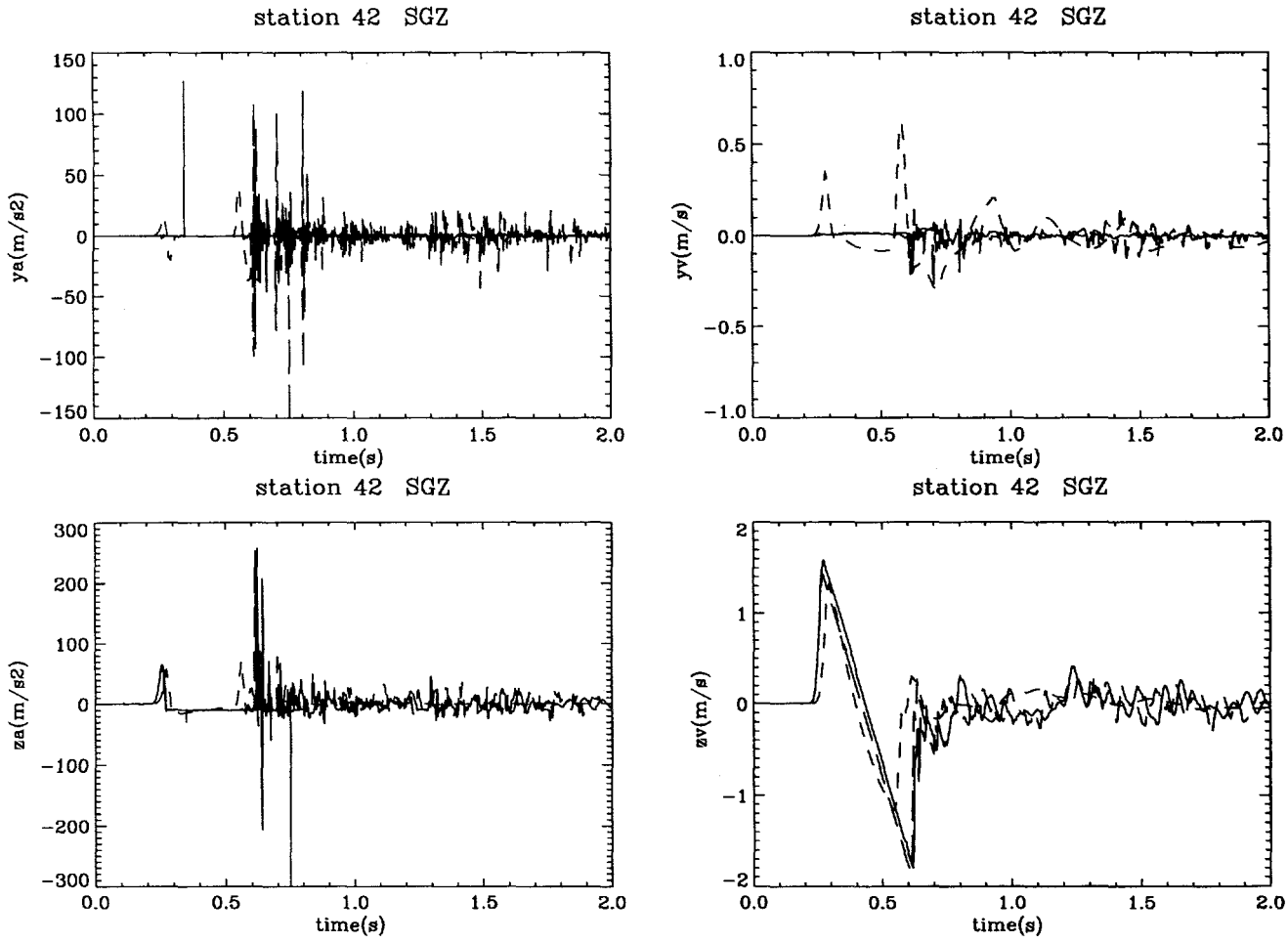

Figure 41: Experimental and computational free-surface results at SGZ. Shown are the radial acceleration (m/s^2), radial velocity (m/s), vertical acceleration (m/s^2), and vertical velocity (m/s) vs. time (s) at the NPE SGZ. The solid line denotes the CE simulation; the long dashed line represents the NE simulation; the short dashed line represents the NPE data collected by LLNL [33], gage GZ. The vertical velocity amplitude and dwell compare favorably between experiment and calculation. The strong signal in experimental radial velocity suggests that the true first surface arrival point may not have been at SGZ.

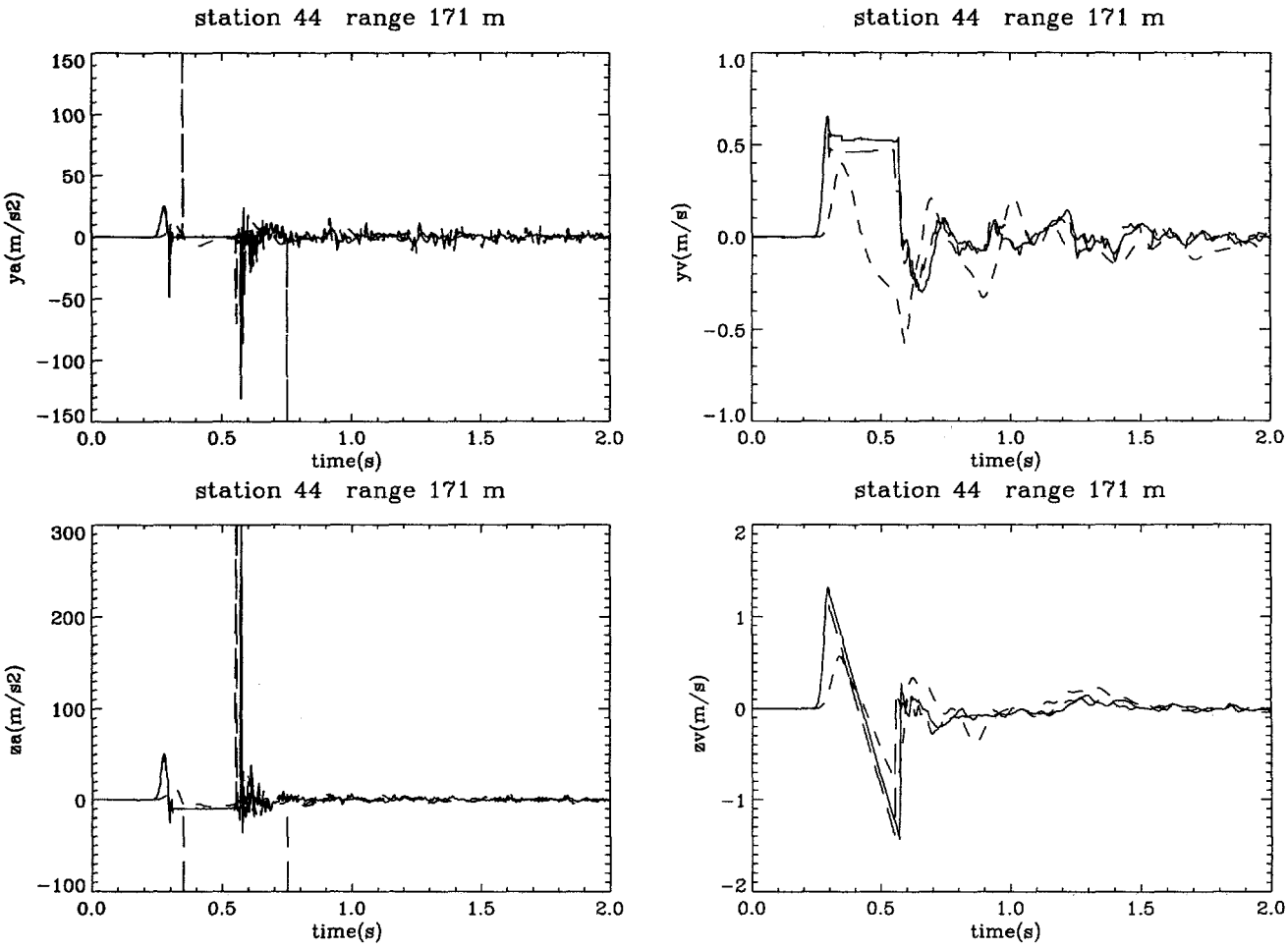

Figure 42: Experimental and computational free-surface results at 171 m. Shown are the radial acceleration (m/s^2), radial velocity (m/s), vertical acceleration (m/s^2), and vertical velocity (m/s) vs. time (s) at 171 m range from the NPE SGZ. The solid line denotes the CE simulation; the long dashed line represents the NE simulation; the short dashed line represents the NPE data collected by LLNL [33], gage E4.

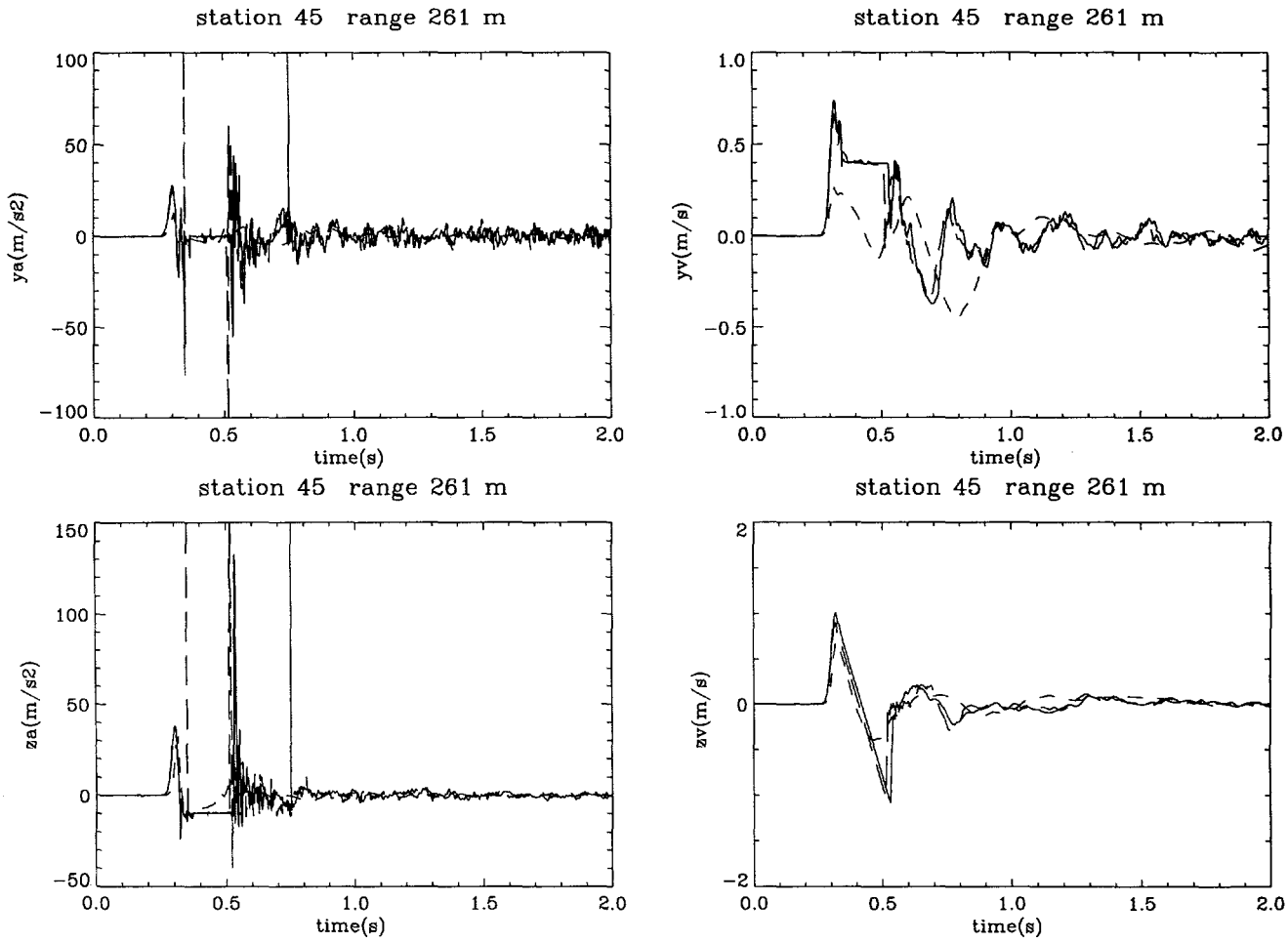

Figure 43: Experimental and computational free-surface results at 261 m. Shown are the radial acceleration (m/s^2), radial velocity (m/s), vertical acceleration (m/s^2), and vertical velocity (m/s) vs. time (s) at 261 m range from the NPE SGZ. The solid line denotes the CE simulation; the long dashed line represents the NE simulation; the short dashed line represents the NPE data collected by LLNL [33], gage E1.

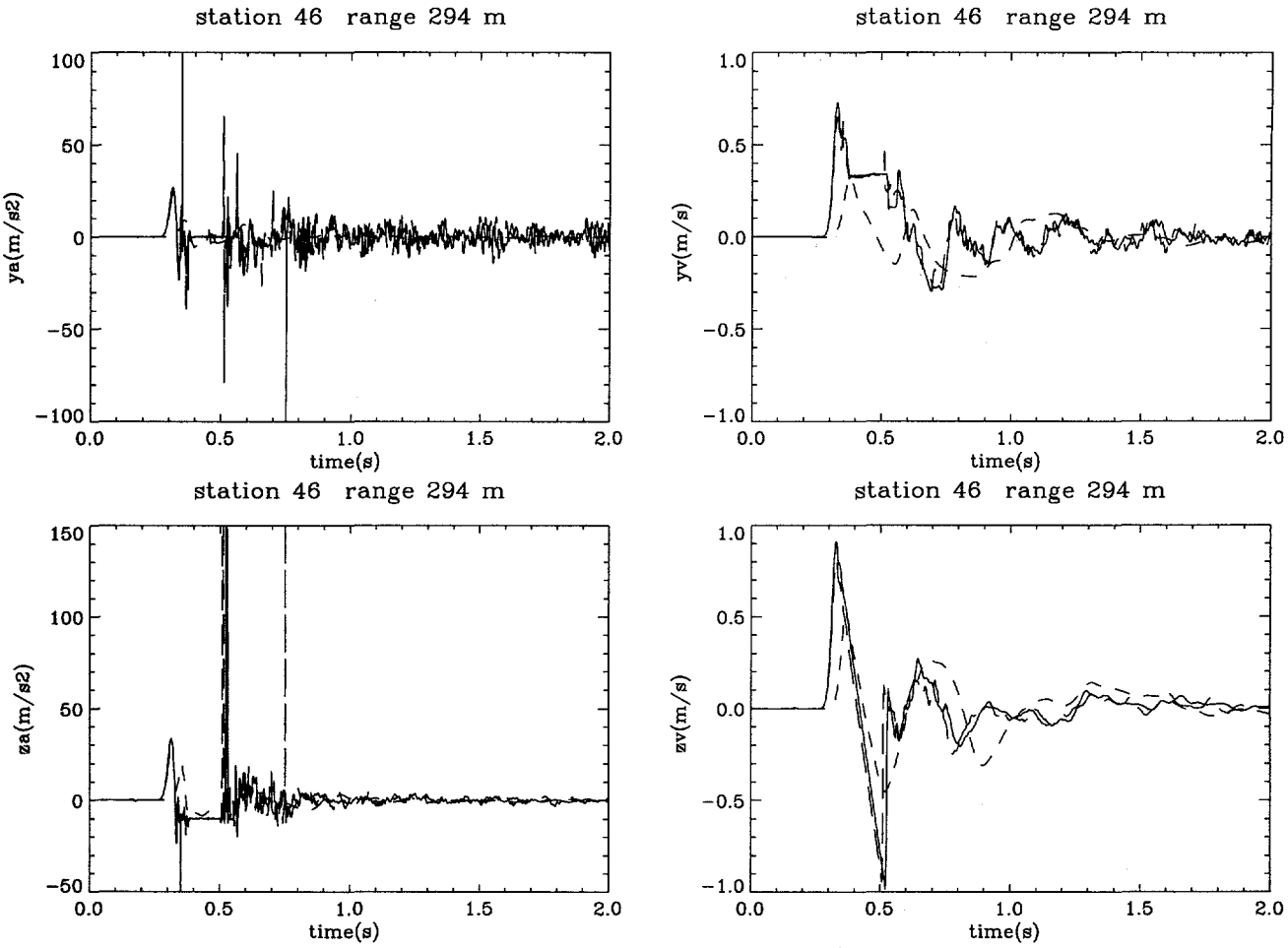

Figure 44: Experimental and computational free-surface results at 294 m. Shown are the radial acceleration (m/s^2), radial velocity (m/s), vertical acceleration (m/s^2), and vertical velocity (m/s) vs. time (s) at 294 m range from the NPE SGZ. The solid line denotes the CE simulation; the long dashed line represents the NE simulation; the short dashed line represents the NPE data collected by LLNL [33], gage Q4.

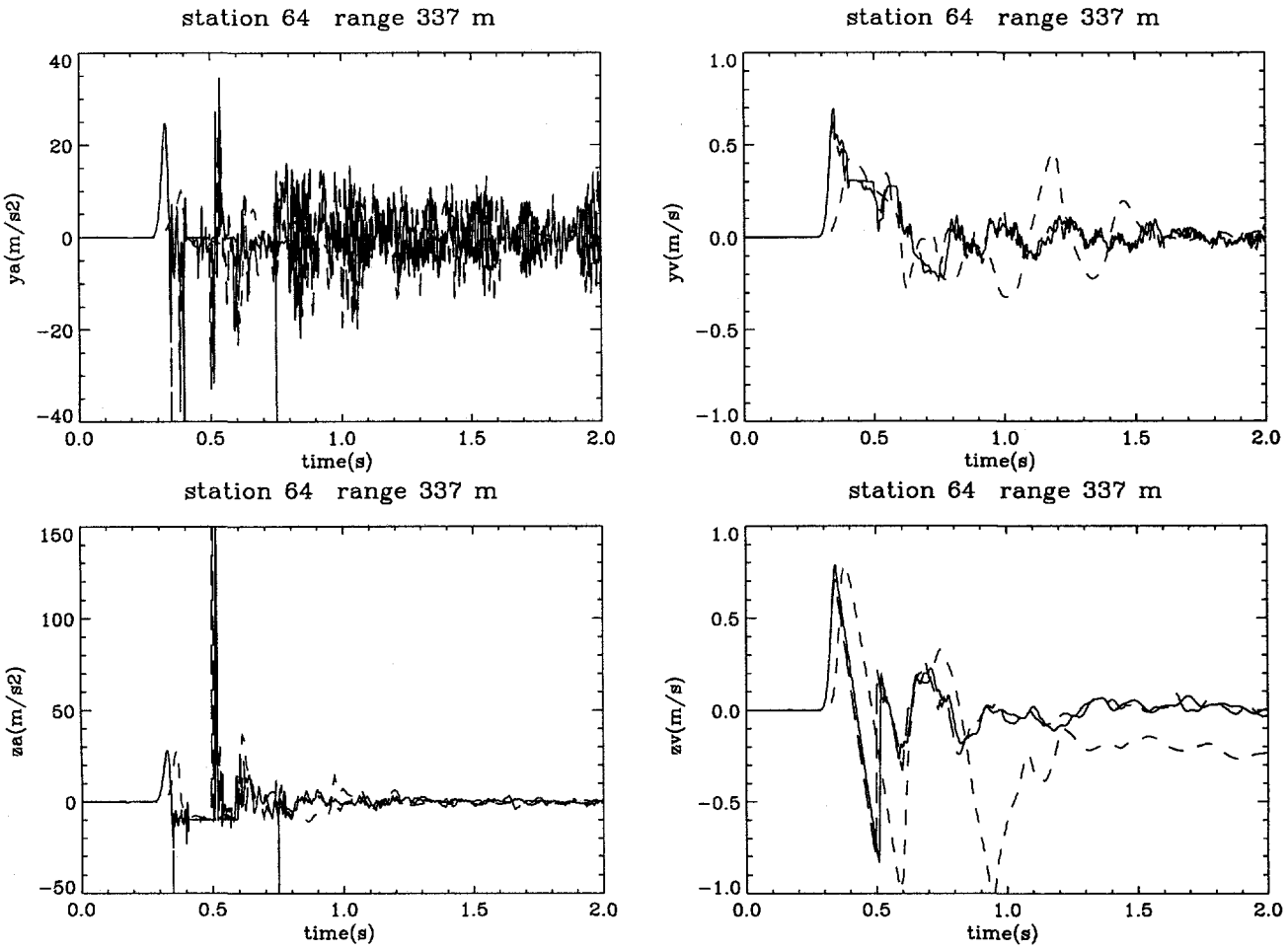

Figure 45: Experimental and computational free-surface results at 337 m. Shown are the radial acceleration (m/s^2), radial velocity (m/s), vertical acceleration (m/s^2), and vertical velocity (m/s) vs. time (s) at 337 m range from the NPE SGZ. The solid line denotes the CE simulation; the long dashed line represents the NE simulation; the short dashed line represents the NPE data collected by LLNL [33], gage H7.

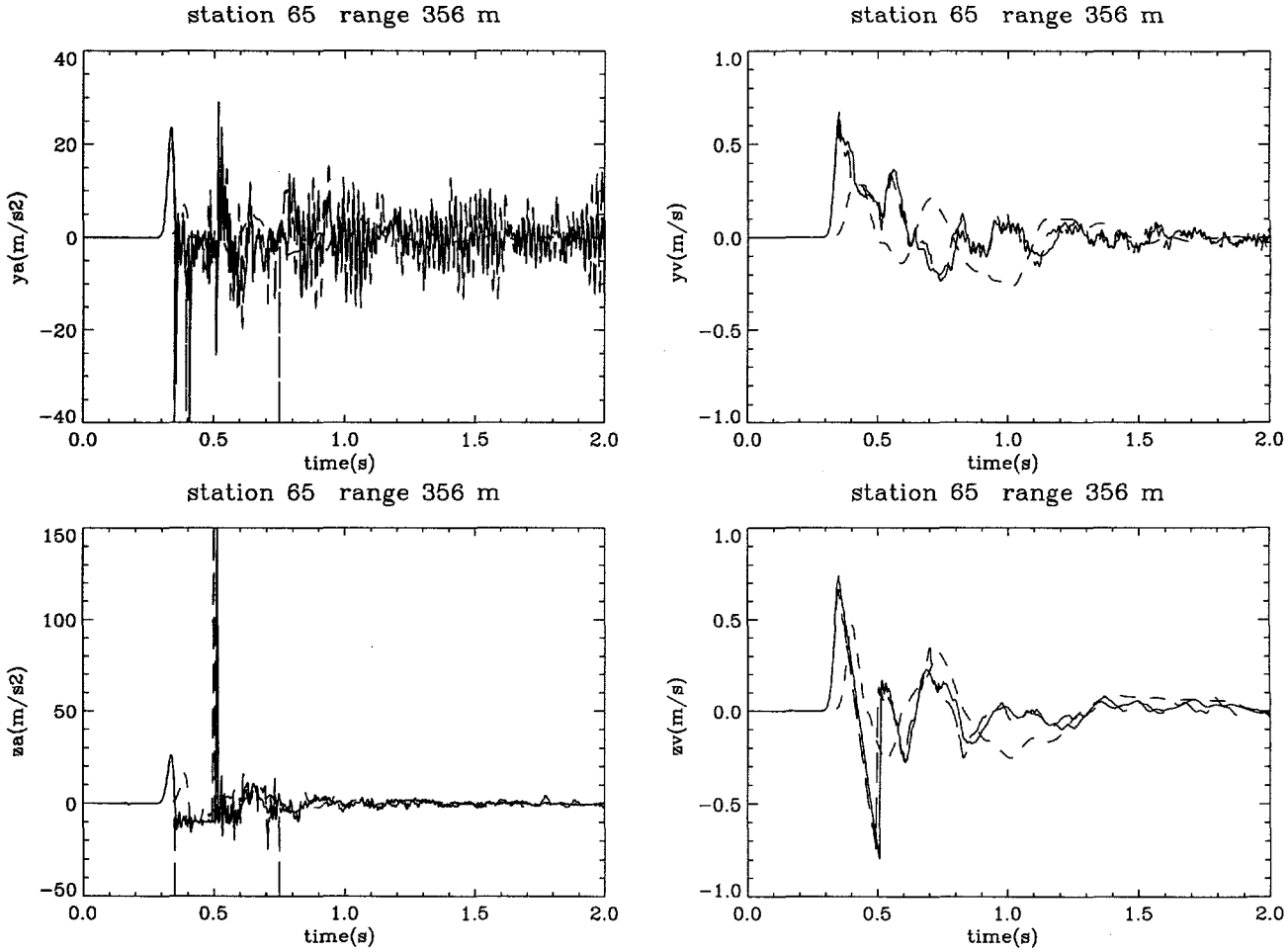

Figure 46: Experimental and computational free-surface results at 356 m. Shown are the radial acceleration (m/s^2), radial velocity (m/s), vertical acceleration (m/s^2), and vertical velocity (m/s) vs. time (s) at 356 m range from the NPE SGZ. The solid line denotes the CE simulation; the long dashed line represents the NE simulation; the short dashed line represents the NPE data collected by LLNL [33], gage H6.

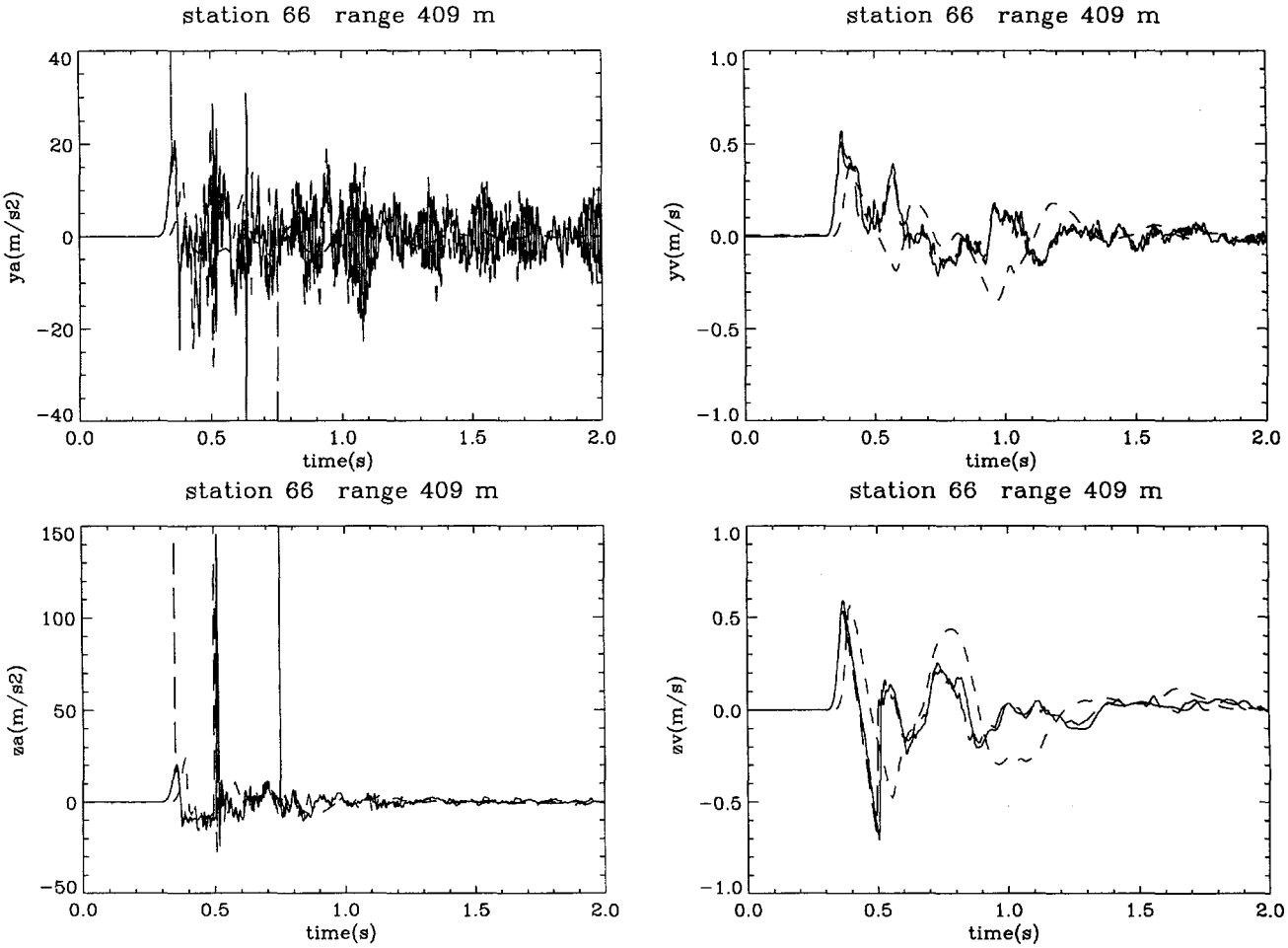

Figure 47: Experimental and computational free-surface results at 409 m. Shown are the radial acceleration (m/s^2), radial velocity (m/s), vertical acceleration (m/s^2), and vertical velocity (m/s) vs. time (s) at 409 m range from the NPE SGZ. The solid line denotes the CE simulation; the long dashed line represents the NE simulation; the short dashed line represents the NPE data collected by LLNL [33], gage H3.

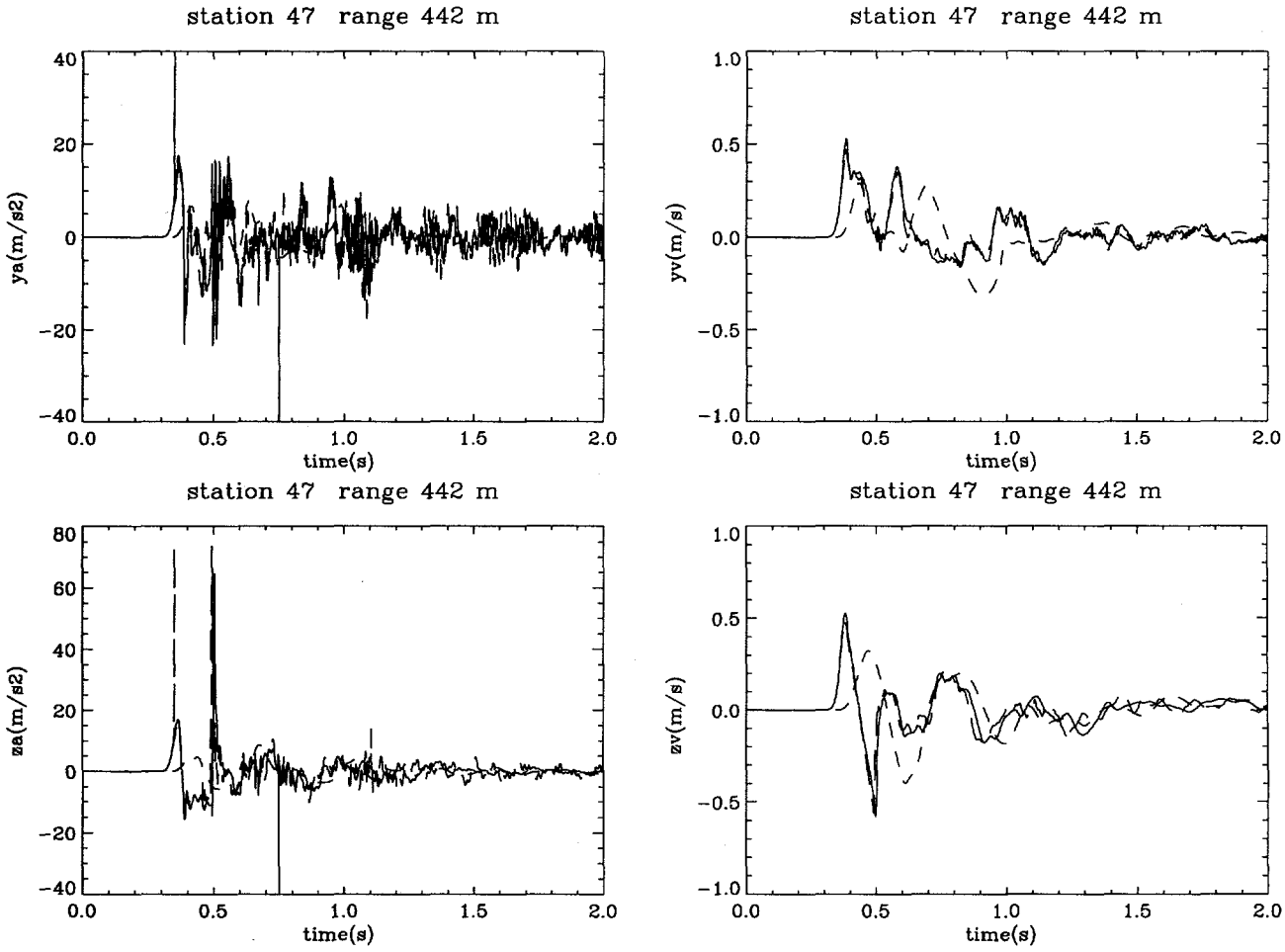

Figure 48: Experimental and computational free-surface results at 442 m. Shown are the radial acceleration (m/s^2), radial velocity (m/s), vertical acceleration (m/s^2), and vertical velocity (m/s) vs. time (s) at 442 m range from the NPE SGZ. The solid line denotes the CE simulation; the long dashed line represents the NE simulation; the short dashed line represents the NPE data collected by LLNL [33], gage S11P.

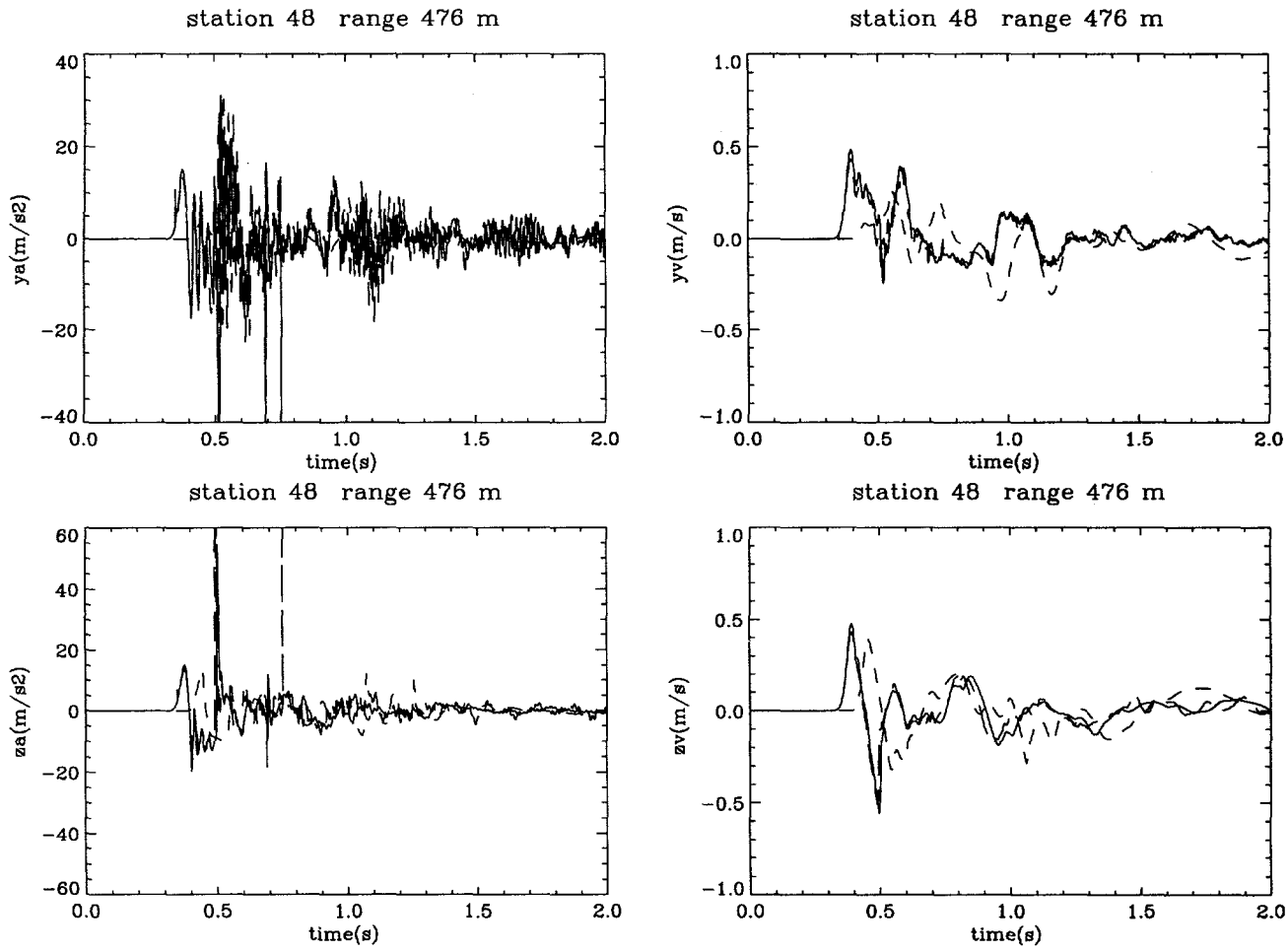

Figure 49: Experimental and computational free-surface results at 476 m. Shown are the radial acceleration (m/s^2), radial velocity (m/s), vertical acceleration (m/s^2), and vertical velocity (m/s) vs. time (s) at 476 m range from the NPE SGZ. The solid line denotes the CE simulation; the long dashed line represents the NE simulation; the short dashed line represents the NPE data collected by LANL [34], gage H9A.

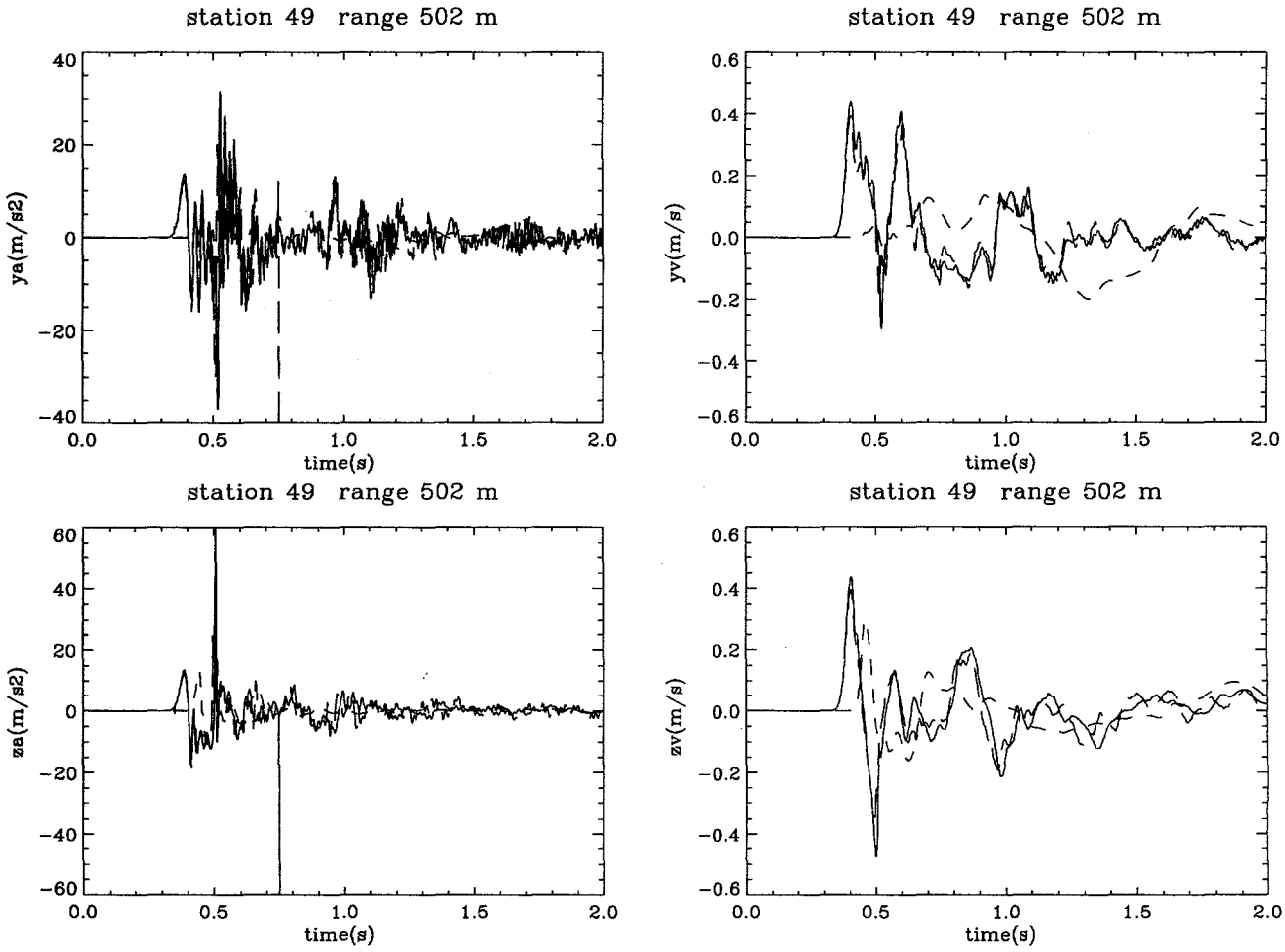

Figure 50: Experimental and computational free-surface results at 502 m. Shown are the radial acceleration (m/s^2), radial velocity (m/s), vertical acceleration (m/s^2), and vertical velocity (m/s) vs. time (s) at 502 m range from the NPE SGZ. The solid line denotes the CE simulation; the long dashed line represents the NE simulation; the short dashed line represents the NPE data collected by LANL [34], gage S11A.

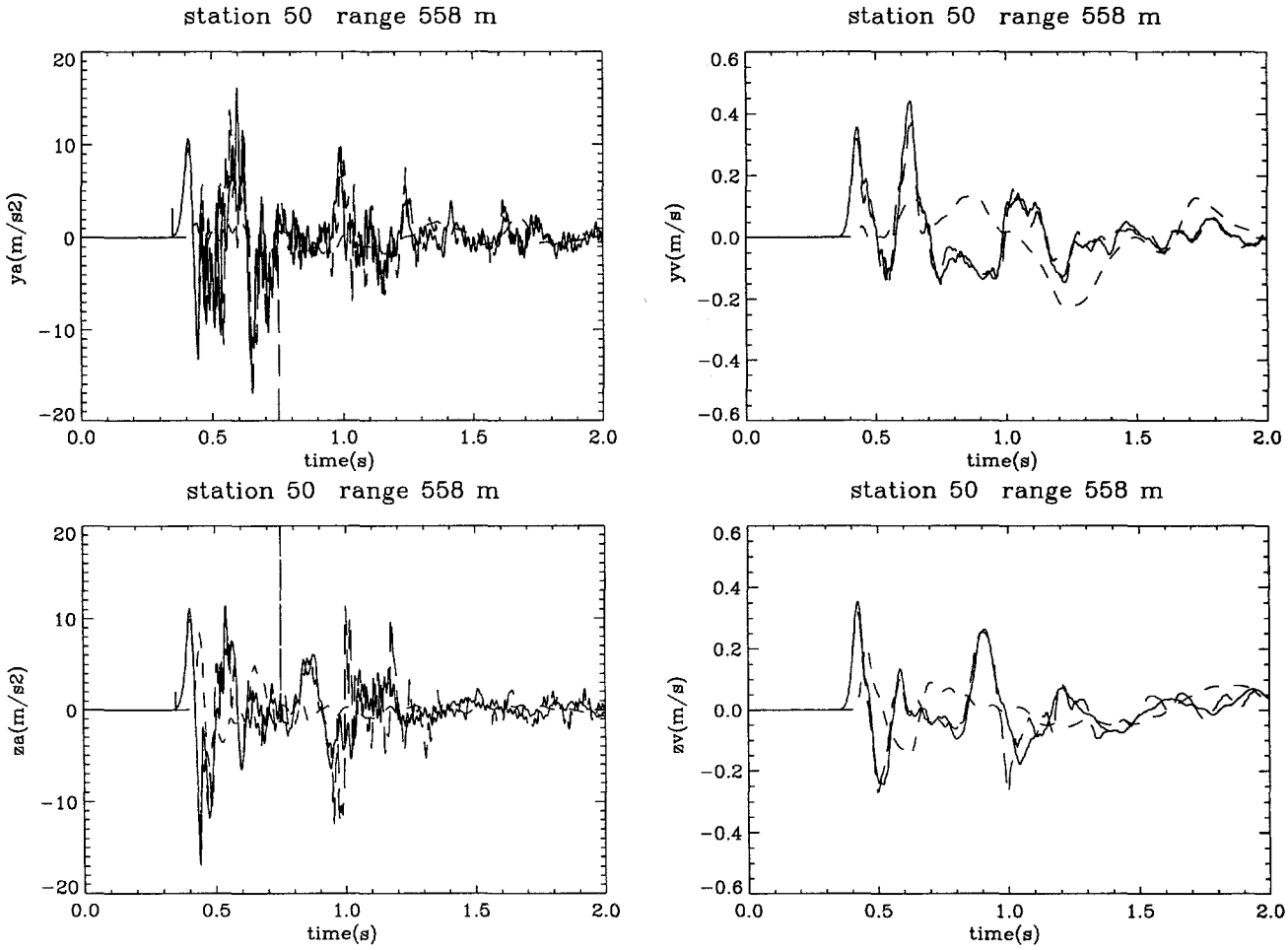

Figure 51: Experimental and computational free-surface results at 558 m. Shown are the radial acceleration (m/s^2), radial velocity (m/s), vertical acceleration (m/s^2), and vertical velocity (m/s) vs. time (s) at 558 m range from the NPE SGZ. The solid line denotes the CE simulation; the long dashed line represents the NE simulation; the short dashed line represents the NPE data collected by LLNL [33], gage E10.

As can be seen by comparing Fig. 41 with the subsequent figures, the experimental data exhibit a more rapid decrease in peak amplitude of both vertical and radial acceleration and velocity as a function of range than the computed results; similarly, the experimental results display a less peaked acceleration structure. The computed results at ranges of 294 m (Fig. 44) to 356 m (Fig. 46) exhibit a double-spall-like signature in vertical velocity; interestingly, this feature[5] is present neither in the calculated results outside of this range nor in the experimental data.

At ranges close to SGZ, there is reasonable agreement between the second computed vertical velocity pulse and corresponding experimental feature (see, e.g., Figs. 42 and 43). The computed spall dwell time matches the data fairly well at the 171 m station (Fig. 42). In the range of the computed double spall (Figs. 44–46), the correlation remains between the third computed pulse and the second experimental pulse. Beyond this range (~400 m), there is a varying amount of "phase coherence" between computed and experimental vertical velocity waveforms at the various stations; heuristically, however, the frequency content as well as the amplitude excursions of the computed result appear comparable to those of the data. The startling exception to this approximate correspondence is the 920 m station (Fig. 60), at which surprisingly good agreement obtains. The correspondence between computed and experimental radial velocity waveforms is somewhat less satisfactory, however, with an overall greater degree of phase decorrelation; specifically, for ranges greater than ~550 m (Fig. 51 ff.) the second computed pulse is of greater amplitude than the first, in contradistinction to the data.

Comparison of surface stations approximately equidistant from SGZ but at different azimuths does not reveal any particular azimuthal traits, such as observed at the free-field stations. One could argue, perhaps, that there is a characteristic difference between the broader second pulse of the vertical velocity between stations in the NW quadrant (e.g., Figs. 44, 294 m range, and 48, 442 m range) and the more peaked second pulse of those stations ESE of SGZ (e.g., Figs. 49, 476 m range, through 51, 558 m range). Such differences are probably of negligible import, however, since signal coherence with even closely spaced arrays may be lacking due to medium structure near the free surface (see the discussion by Stump *et al.* [35]).

Generally speaking, the moderate agreement between calculated and experimental waveforms decreases with range from SGZ, although there appears to be good heuristic agreement in frequency content at all ranges. The variation between calculation and experiment is to be expected, as the computed results presuppose a cylindrically symmetrical, horizontally layered medium, while the variations in bedding, material properties, and coherence of the *in situ* rock depart radically from this assumption.

[5] As in the calculations of Jones *et al.* [36], the secondary spall may be related to elastic rebound of material in response to initial cavity growth.

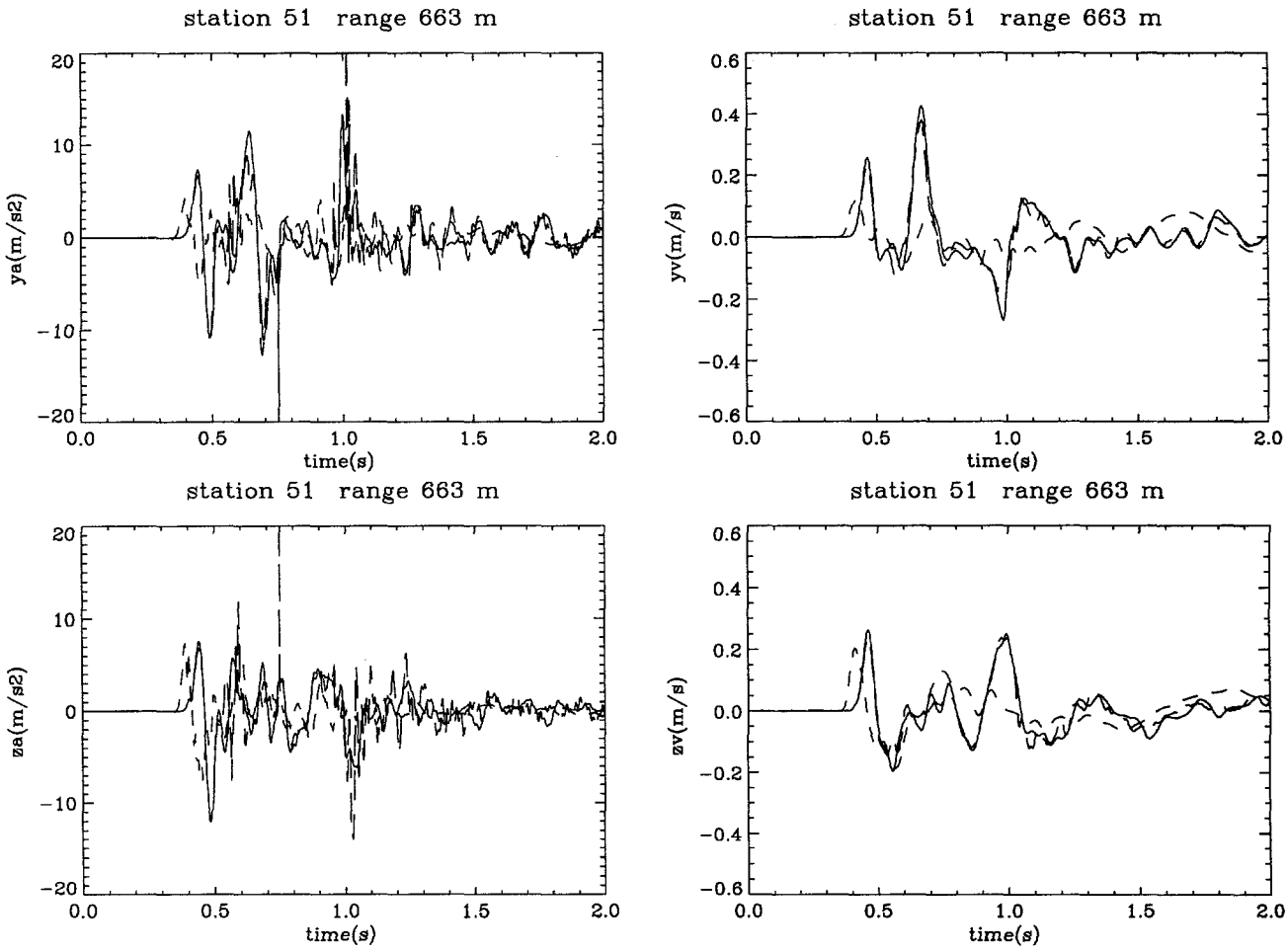

Figure 52: Experimental and computational free-surface results at 663 m. Shown are the radial acceleration (m/s^2), radial velocity (m/s), vertical acceleration (m/s^2), and vertical velocity (m/s) vs. time (s) at 663 m range from the NPE SGZ. The solid line denotes the CE simulation; the long dashed line represents the NE simulation; the short dashed line represents the NPE data collected by LANL [34], gage S6A.

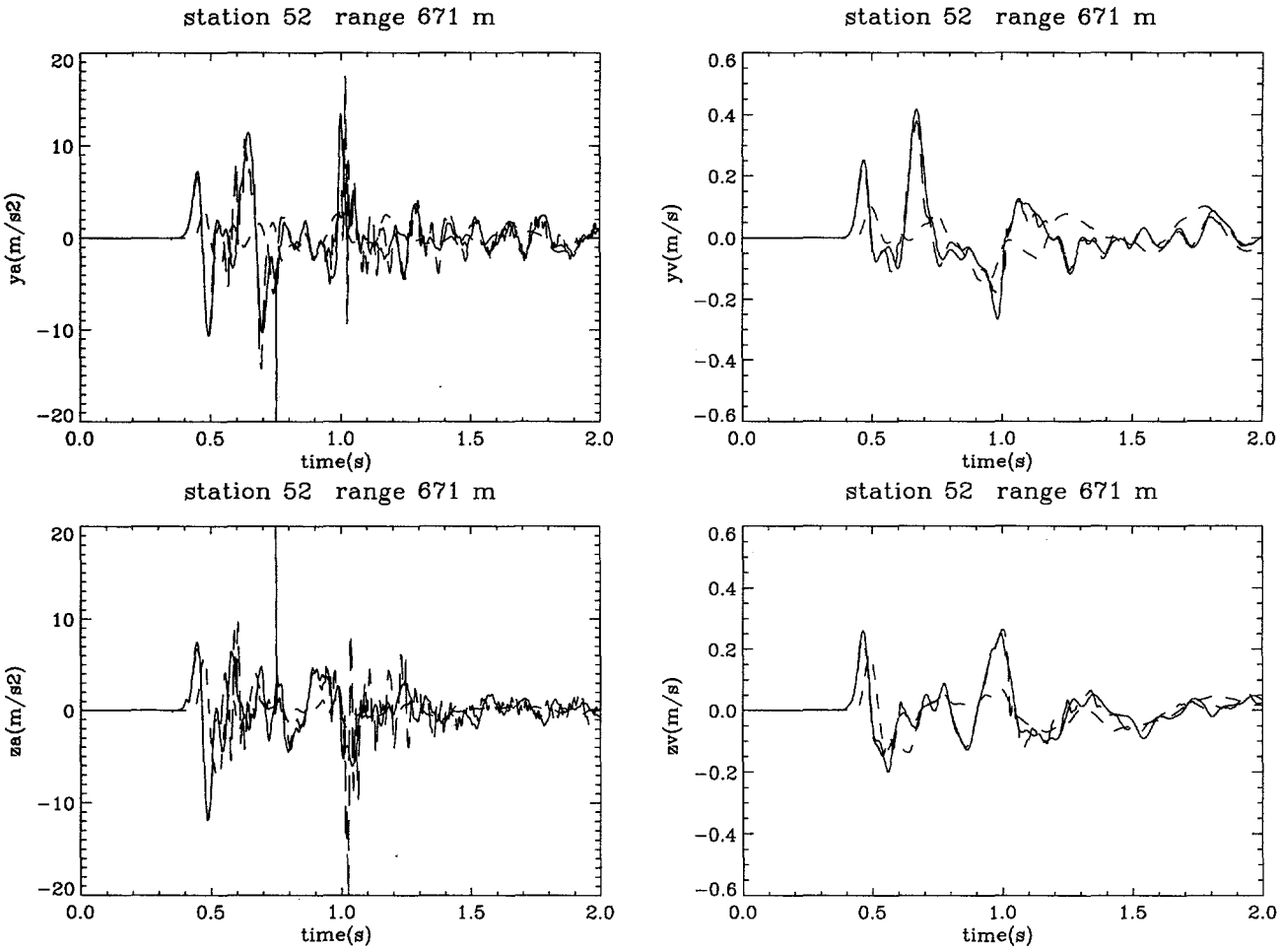

Figure 53: Experimental and computational free-surface results at 671 m. Shown are the radial acceleration (m/s^2), radial velocity (m/s), vertical acceleration (m/s^2), and vertical velocity (m/s) vs. time (s) at 671 m range from the NPE SGZ. The solid line denotes the CE simulation; the long dashed line represents the NE simulation; the short dashed line represents the NPE data collected by LLNL [33], gage E6.

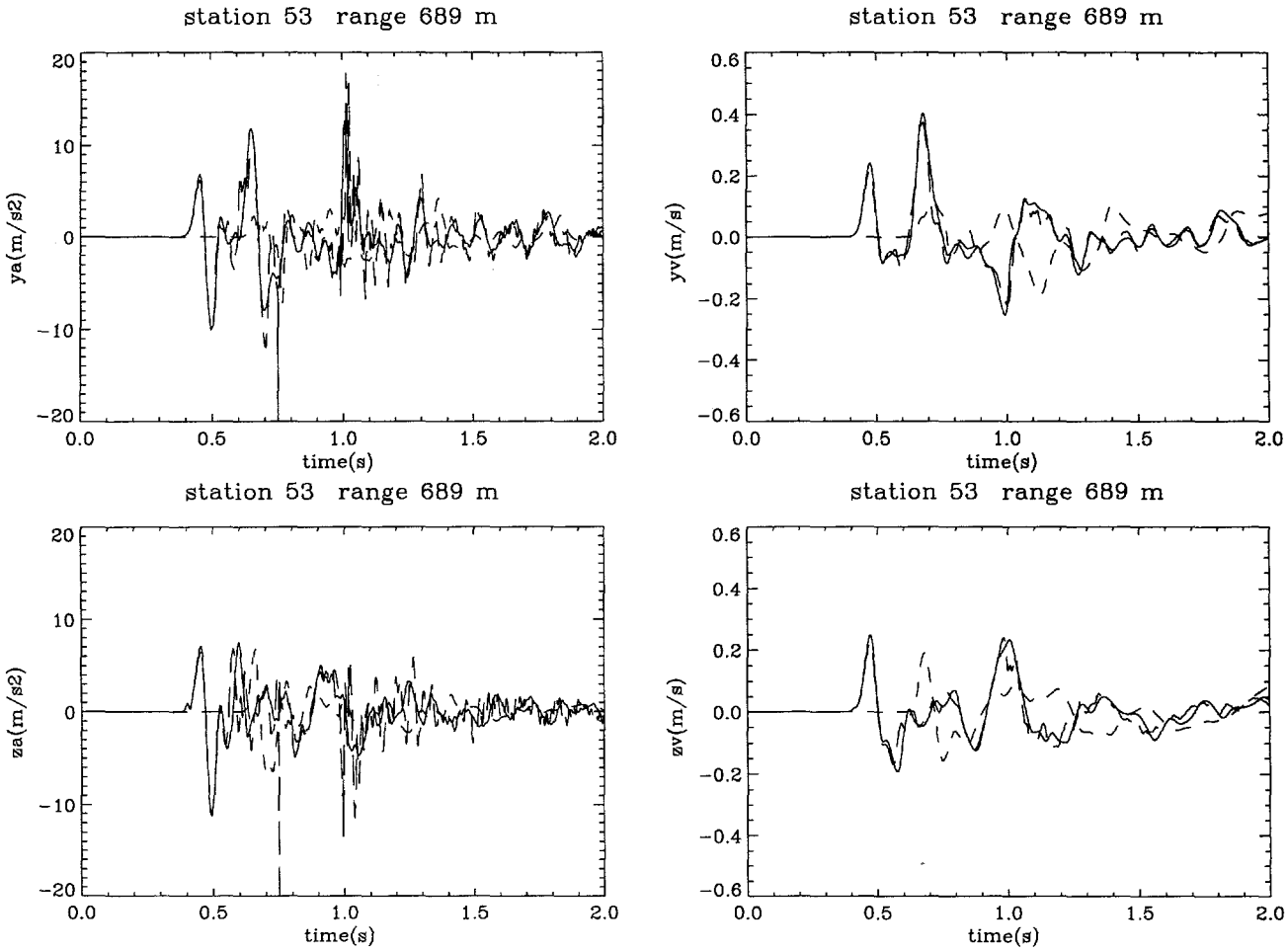

Figure 54: Experimental and computational free-surface results at 689 m. Shown are the radial acceleration (m/s^2), radial velocity (m/s), vertical acceleration (m/s^2), and vertical velocity (m/s) vs. time (s) at 689 m range from the NPE SGZ. The solid line denotes the CE simulation; the long dashed line represents the NE simulation; the short dashed line represents the NPE data collected by LANL [34], gage S10P.

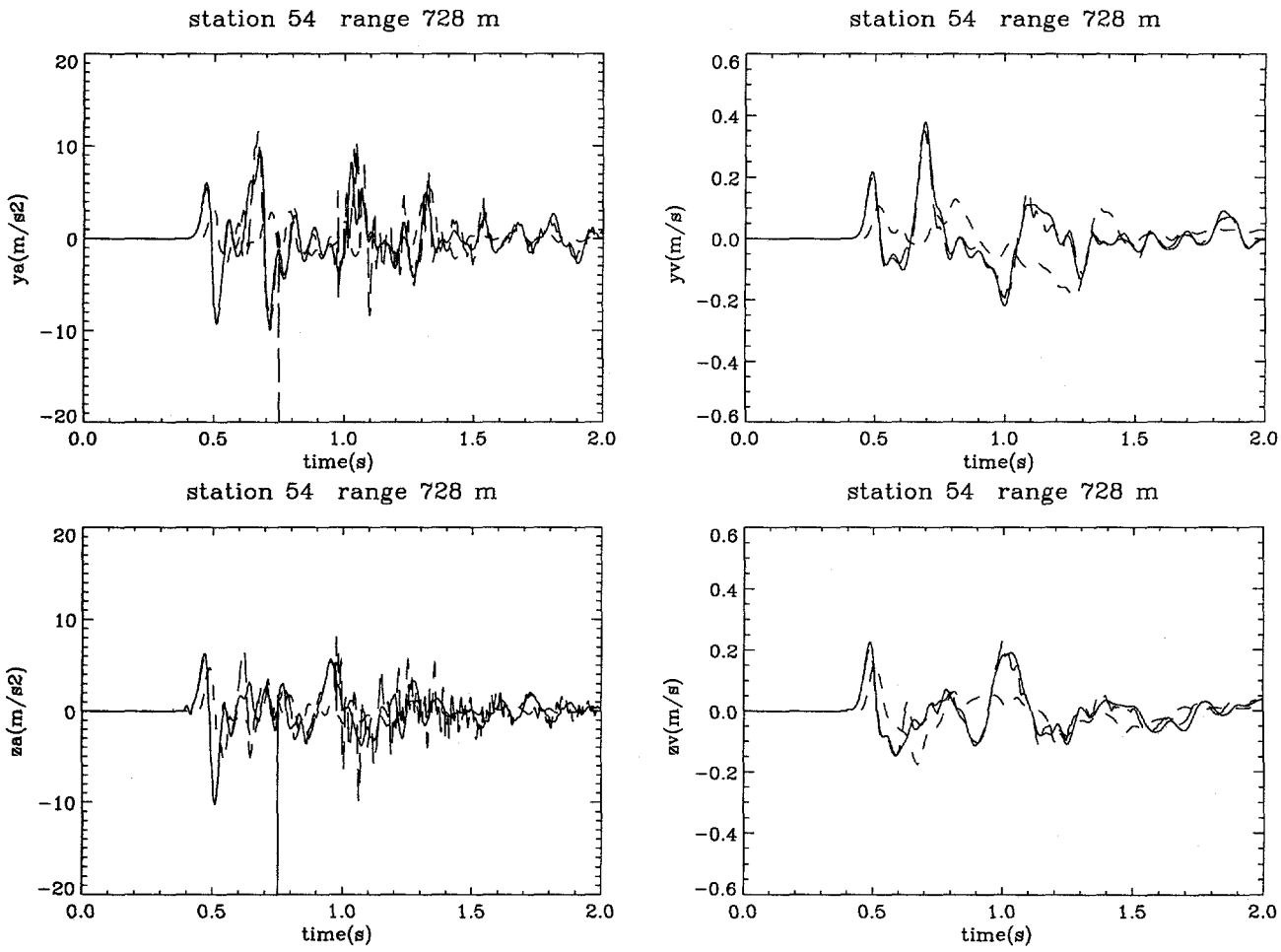

Figure 55: Experimental and computational free-surface results at 728 m. Shown are the radial acceleration (m/s^2), radial velocity (m/s), vertical acceleration (m/s^2), and vertical velocity (m/s) vs. time (s) at 728 m range from the NPE SGZ. The solid line denotes the CE simulation; the long dashed line represents the NE simulation; the short dashed line represents the NPE data collected by LLNL [33], gage Q5.

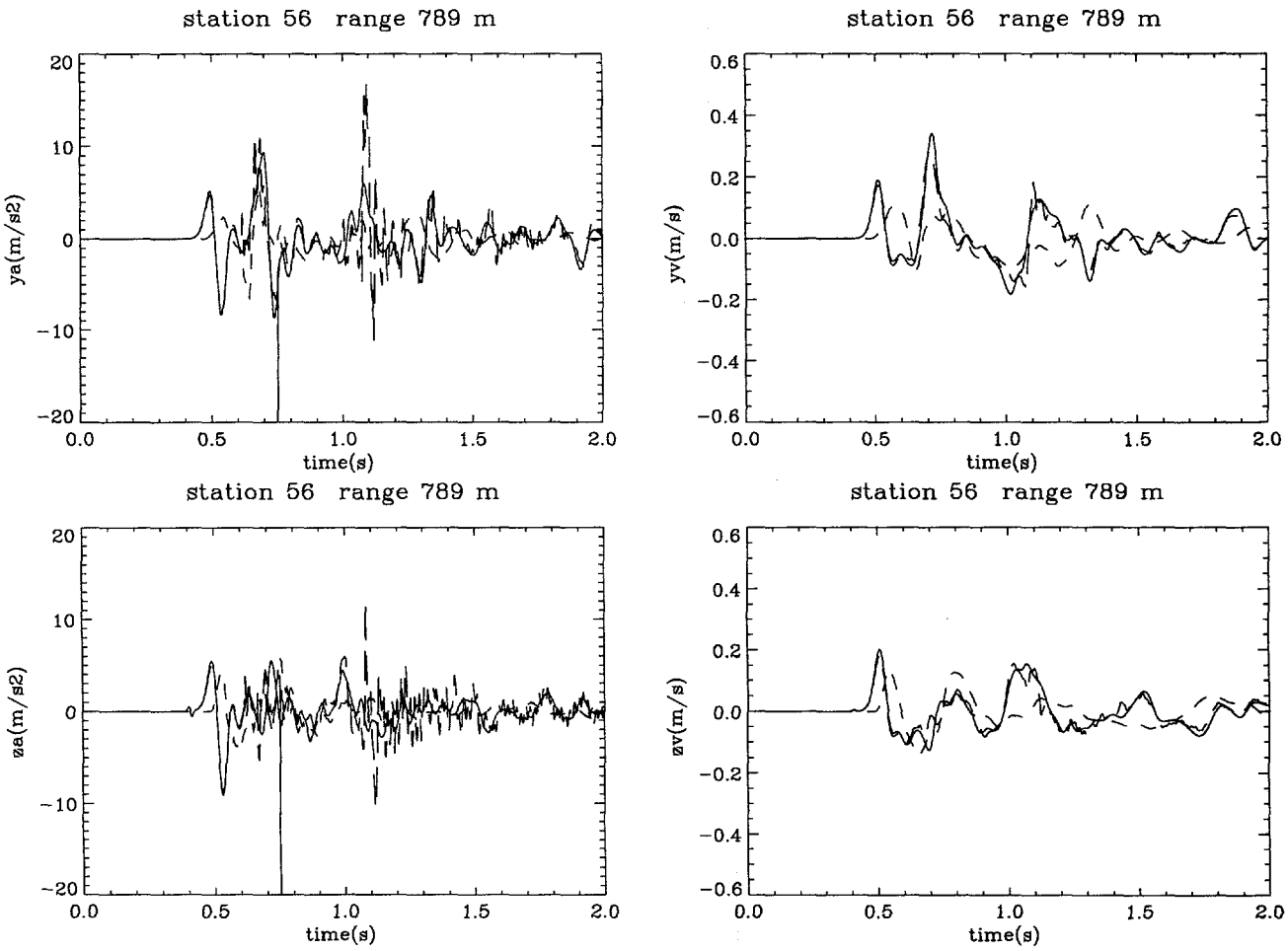

Figure 56: Experimental and computational free-surface results at 789 m. Shown are the radial acceleration (m/s^2), radial velocity (m/s), vertical acceleration (m/s^2), and vertical velocity (m/s) vs. time (s) at 789 m range from the NPE SGZ. The solid line denotes the CE simulation; the long dashed line represents the NE simulation; the short dashed line represents the NPE data collected by LANL [34], gage S6P.

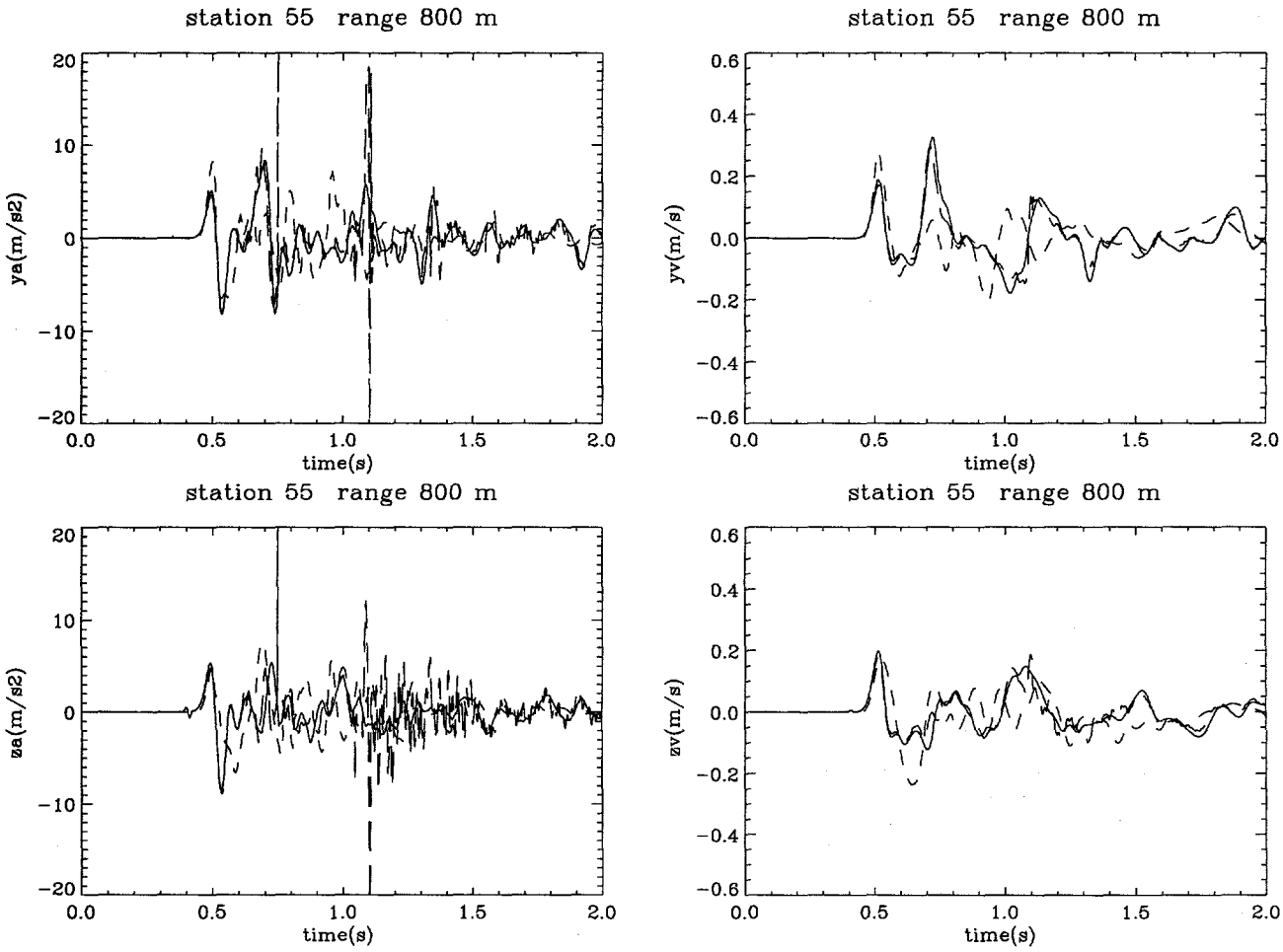

Figure 57: Experimental and computational free-surface results at 800 m. Shown are the radial acceleration (m/s^2), radial velocity (m/s), vertical acceleration (m/s^2), and vertical velocity (m/s) vs. time (s) at 800 m range from the NPE SGZ. The solid line denotes the CE simulation; the long dashed line represents the NE simulation; the short dashed line represents the NPE data collected by LANL [34], gage S10A.

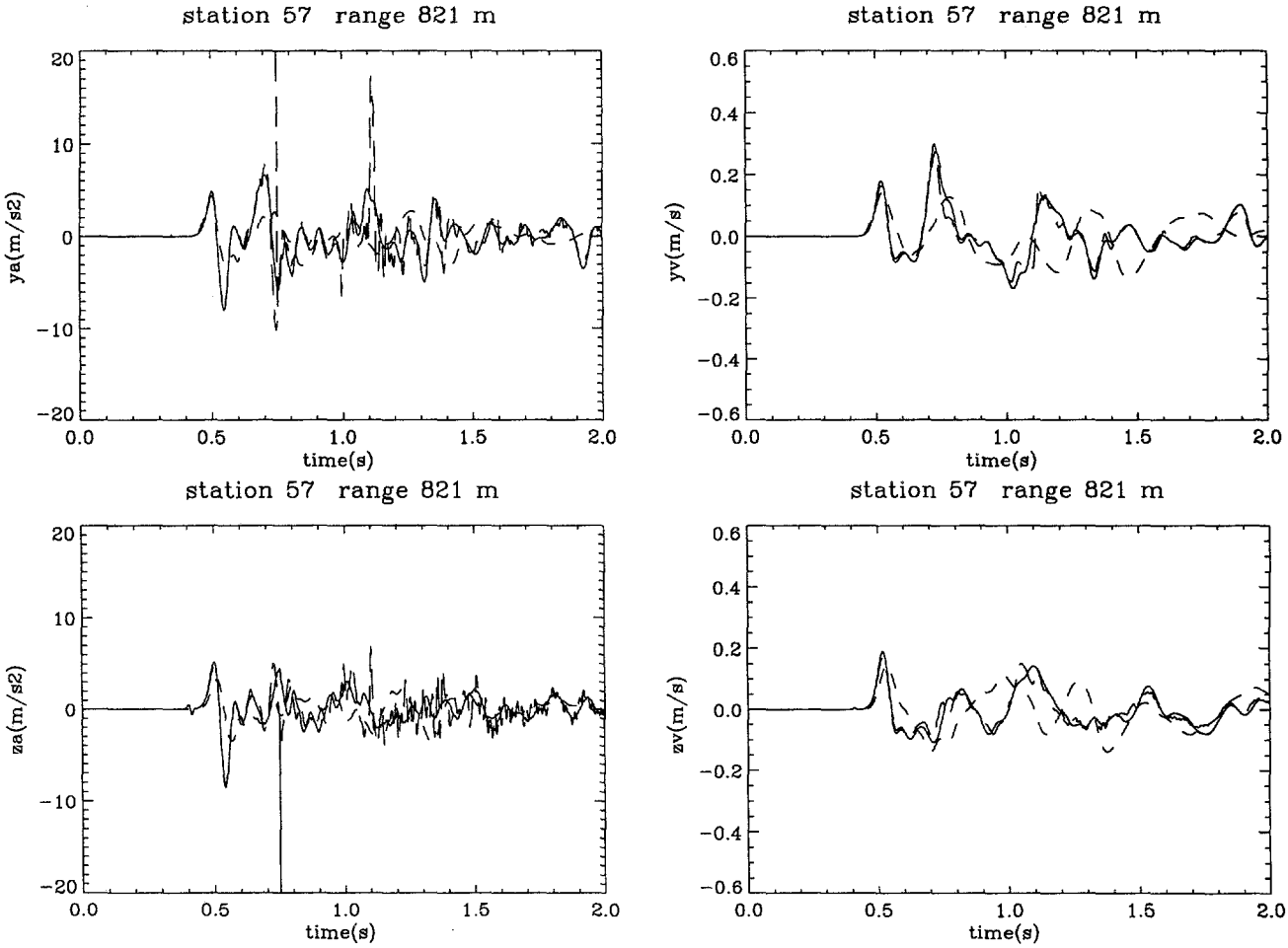

Figure 58: Experimental and computational free-surface results at 821 m. Shown are the radial acceleration (m/s^2), radial velocity (m/s), vertical acceleration (m/s^2), and vertical velocity (m/s) vs. time (s) at 821 m range from the NPE SGZ. The solid line denotes the CE simulation; the long dashed line represents the NE simulation; the short dashed line represents the NPE data collected by LLNL [33], gage Q3.

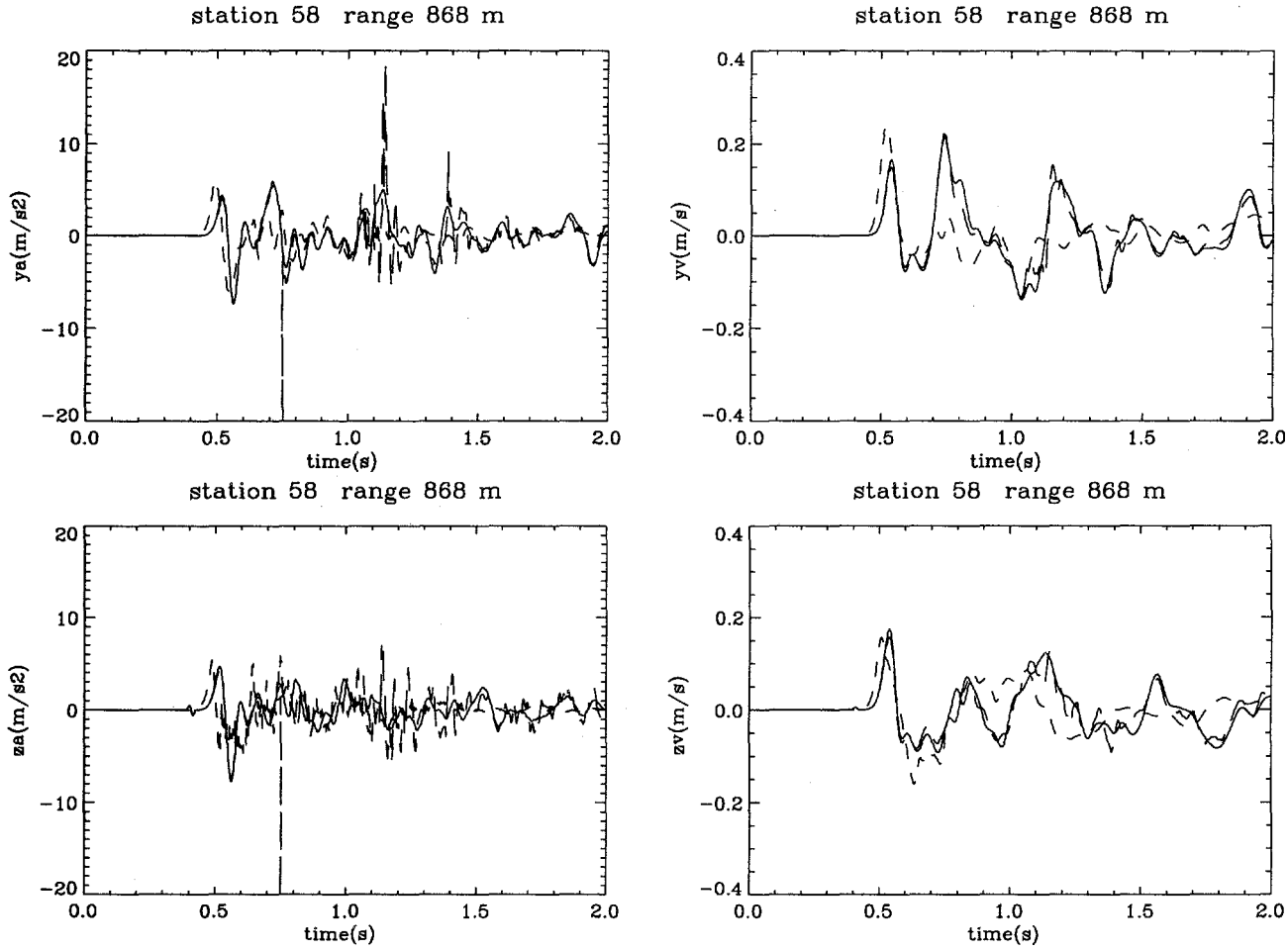

Figure 59: Experimental and computational free-surface results at 868 m. Shown are the radial acceleration (m/s^2), radial velocity (m/s), vertical acceleration (m/s^2), and vertical velocity (m/s) vs. time (s) at 868 m range from the NPE SGZ. The solid line denotes the CE simulation; the long dashed line represents the NE simulation; the short dashed line represents the NPE data collected by LANL [34], gage S4A.

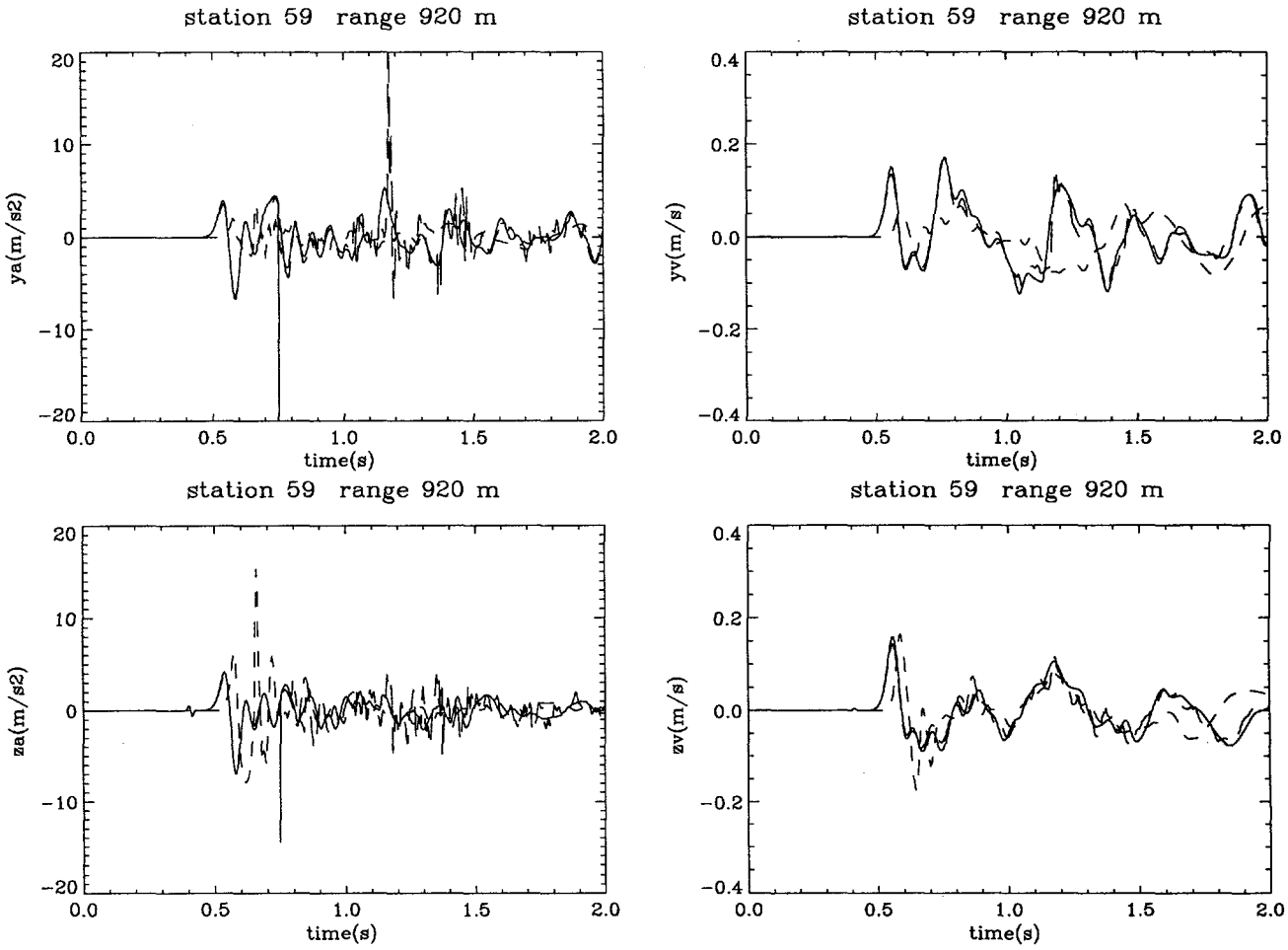

Figure 60: Experimental and computational free-surface results at 920 m. Shown are the radial acceleration (m/s^2), radial velocity (m/s), vertical acceleration (m/s^2), and vertical velocity (m/s) vs. time (s) at 920 m range from the NPE SGZ. The solid line denotes the CE simulation; the long dashed line represents the NE simulation; the short dashed line represents the NPE data collected by LANL [34], gage S12P.

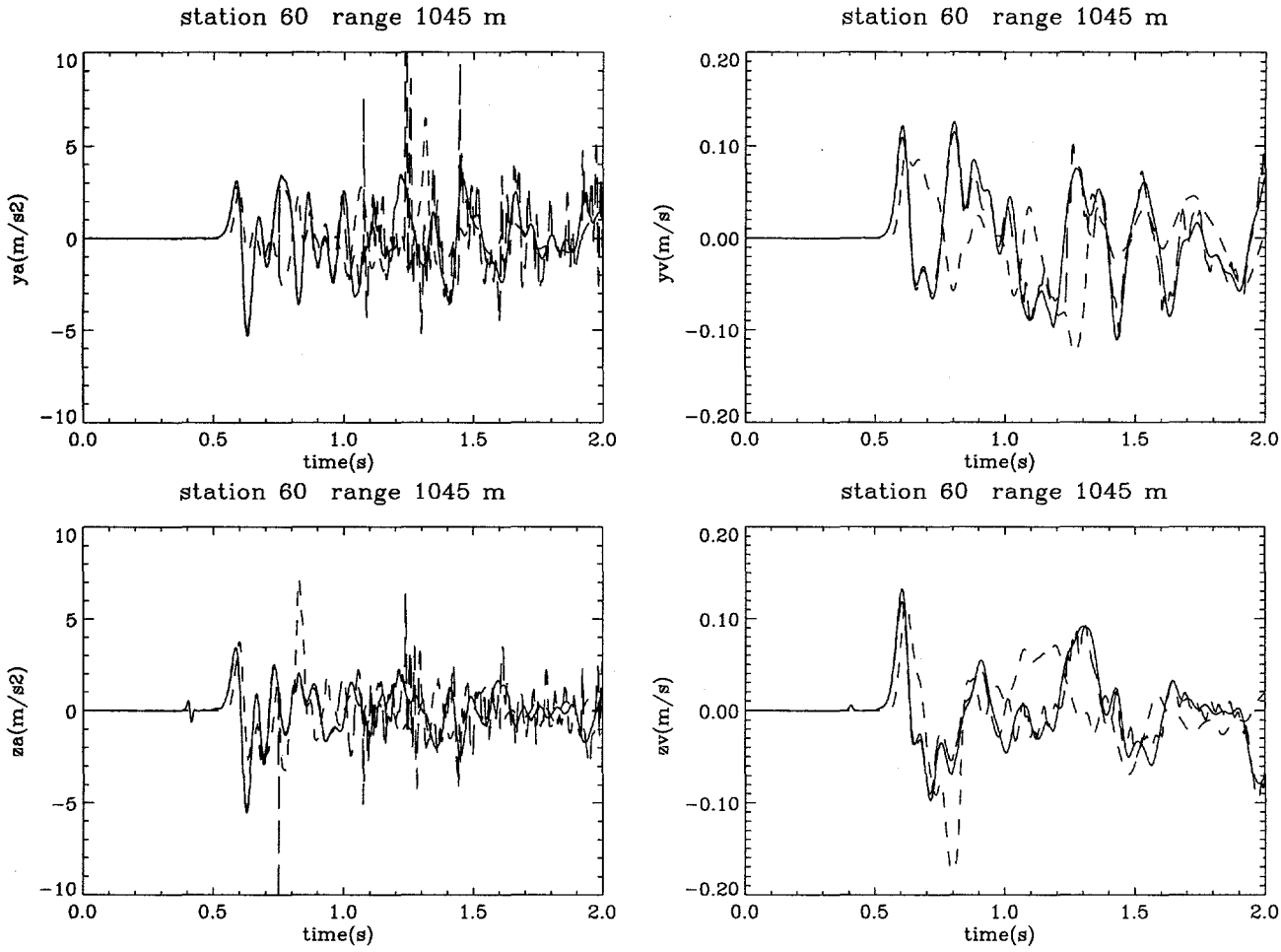

Figure 61: Experimental and computational free-surface results at 1045 m. Shown are the radial acceleration (m/s^2), radial velocity (m/s), vertical acceleration (m/s^2), and vertical velocity (m/s) vs. time (s) at 1045 m range from the NPE SGZ. The solid line denotes the CE simulation; the long dashed line represents the NE simulation; the short dashed line represents the NPE data collected by LANL [34], gage S4P.

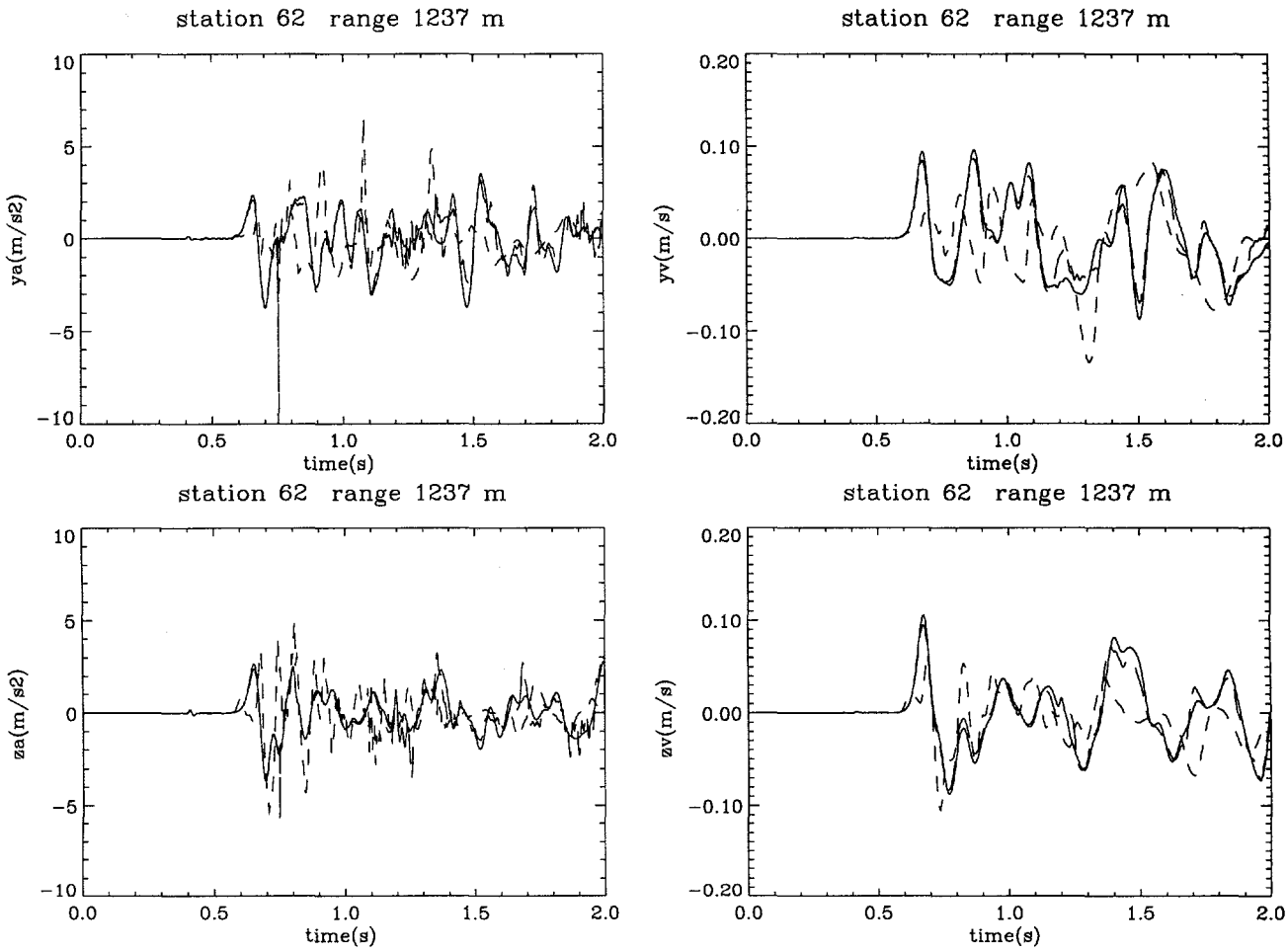

Figure 62: Experimental and computational free-surface results at 1237 m. Shown are the radial acceleration (m/s^2), radial velocity (m/s), vertical acceleration (m/s^2), and vertical velocity (m/s) vs. time (s) at 1237 m range from the NPE SGZ. The solid line denotes the CE simulation; the long dashed line represents the NE simulation; the short dashed line represents the NPE data collected by LANL [34], gage S8A.

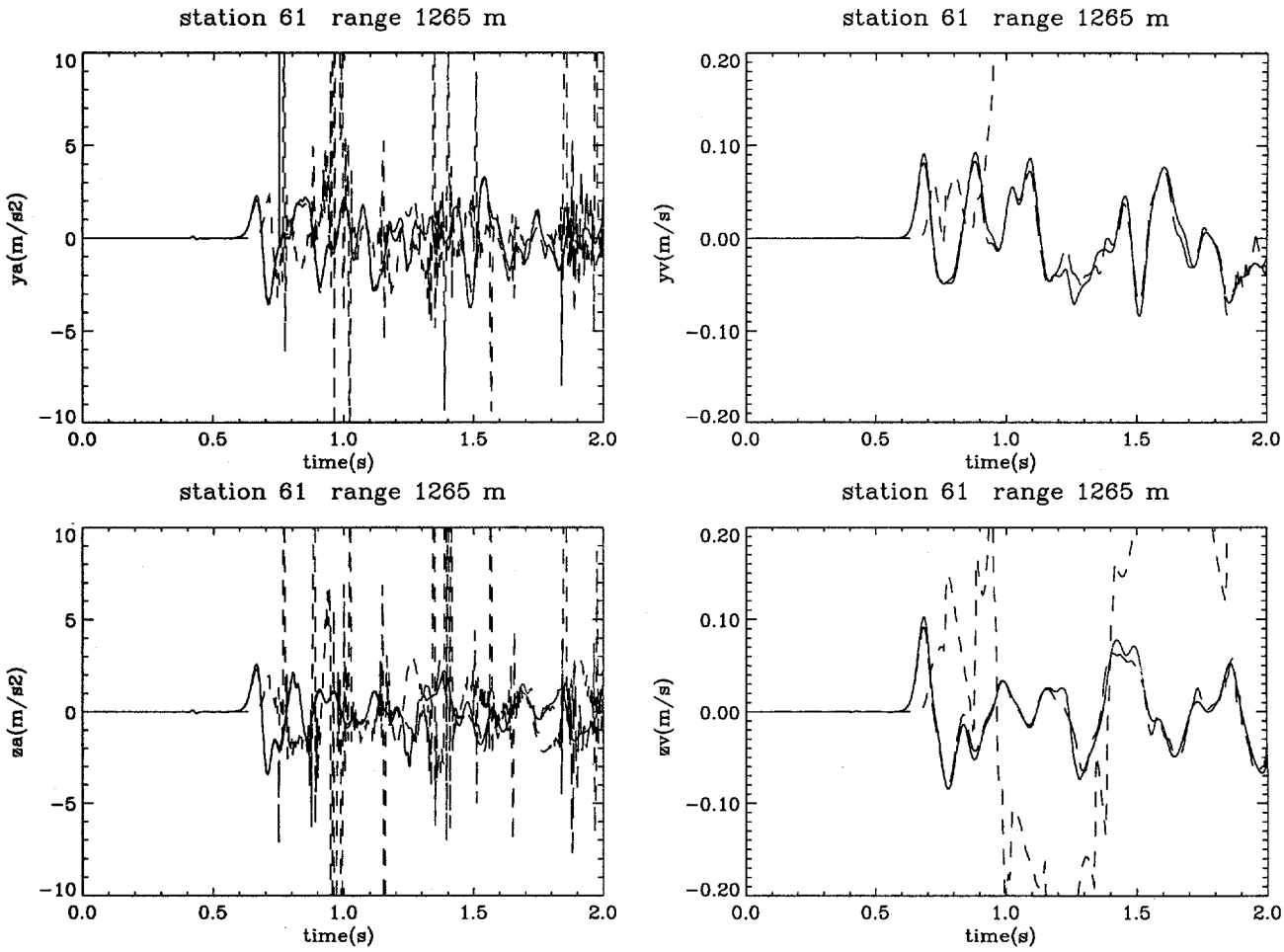

Figure 63: Experimental and computational free-surface results at 1265 m. Shown are the radial acceleration (m/s^2), radial velocity (m/s), vertical acceleration (m/s^2), and vertical velocity (m/s) vs. time (s) at 1265 m range from the NPE SGZ. The solid line denotes the CE simulation; the long dashed line represents the NE simulation; the short dashed line represents the NPE data collected by LANL [34], gage S2A. Although these gages obviously did not record the event correctly, we include this station for completeness.

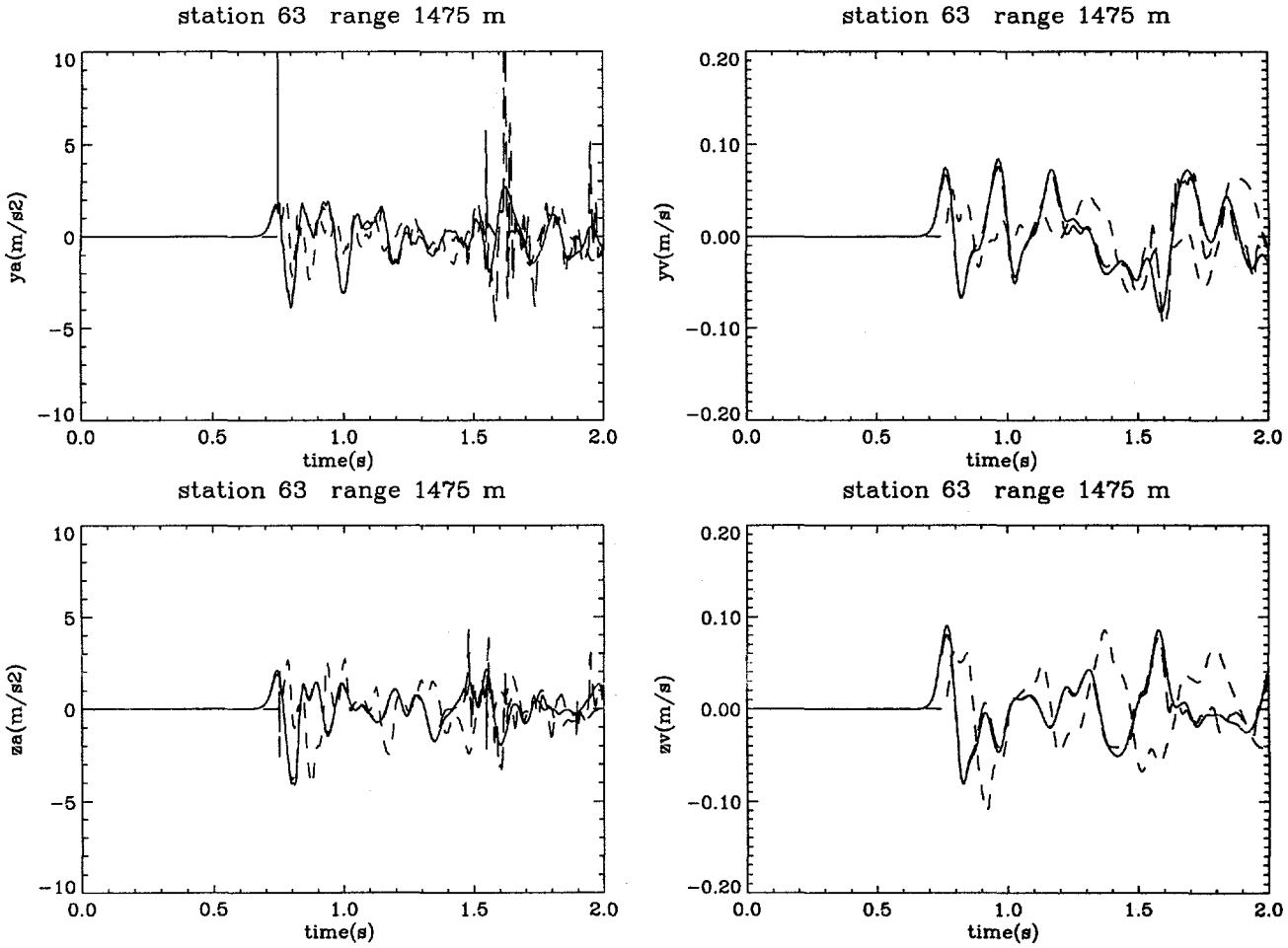

Figure 64: Experimental and computational free-surface results at 1475 m. Shown are the radial acceleration (m/s^2), radial velocity (m/s), vertical acceleration (m/s^2), and vertical velocity (m/s) vs. time (s) at 1475 m range from the NPE SGZ. The solid line denotes the CE simulation; the long dashed line represents the NE simulation; the short dashed line represents the NPE data collected by LANL [34], gage S2P.

Figure 65 is a record section plot of the free-surface vertical velocity as a function of time, in which the ordinate for *each* trace has been normalized (so that, e.g., only gross structure should be compared), with the solid lines representing computed waveforms and the dotted lines being the experimental data. In this figure, it is seen that the experimental data (1) display nonideal spall structure at SGZ, (2) exhibit coherent post-slapdown wave structure near SGZ (relative to the calculated results), and (3) demonstrate that the first arrival time for the experimental data is clearly *not* a linear function of range (as opposed to the computational results). The facts that the data exhibit nonideal spall structure and have first arrival times that are not exactly a linear function of range are presumably related to medium inhomogeneities, nonuniform subsurface structure, and scattering effects. The simple spall model and uniform layering assumed in the simulations produced idealized behavior in these regards. Figure 66 contains the same data, but the traces have *not* been normalized, thereby demonstrating the geometric effect on amplitudes.

The peak free-surface vertical velocity (m/s) vs. range (m) is shown in Figure 67, in which the values at the various experimental stations are indicated by $\otimes$ connected by the dotted line, the results of the CE simulation are shown as the solid line, and the results of the NE simulation are given by the dashed line and the values provided by the free-field peak radial velocity scaling relations of Perret & Bass [30] for wet tuff (dash-dot line). Both calculated and scaled results are somewhat greater than the experimental values; nonetheless, this plot suggests that the scaled results provide reasonable estimates of the peak free-surface vertical velocity despite the fact that the Perret & Bass relations are based on free-field radial velocity data.

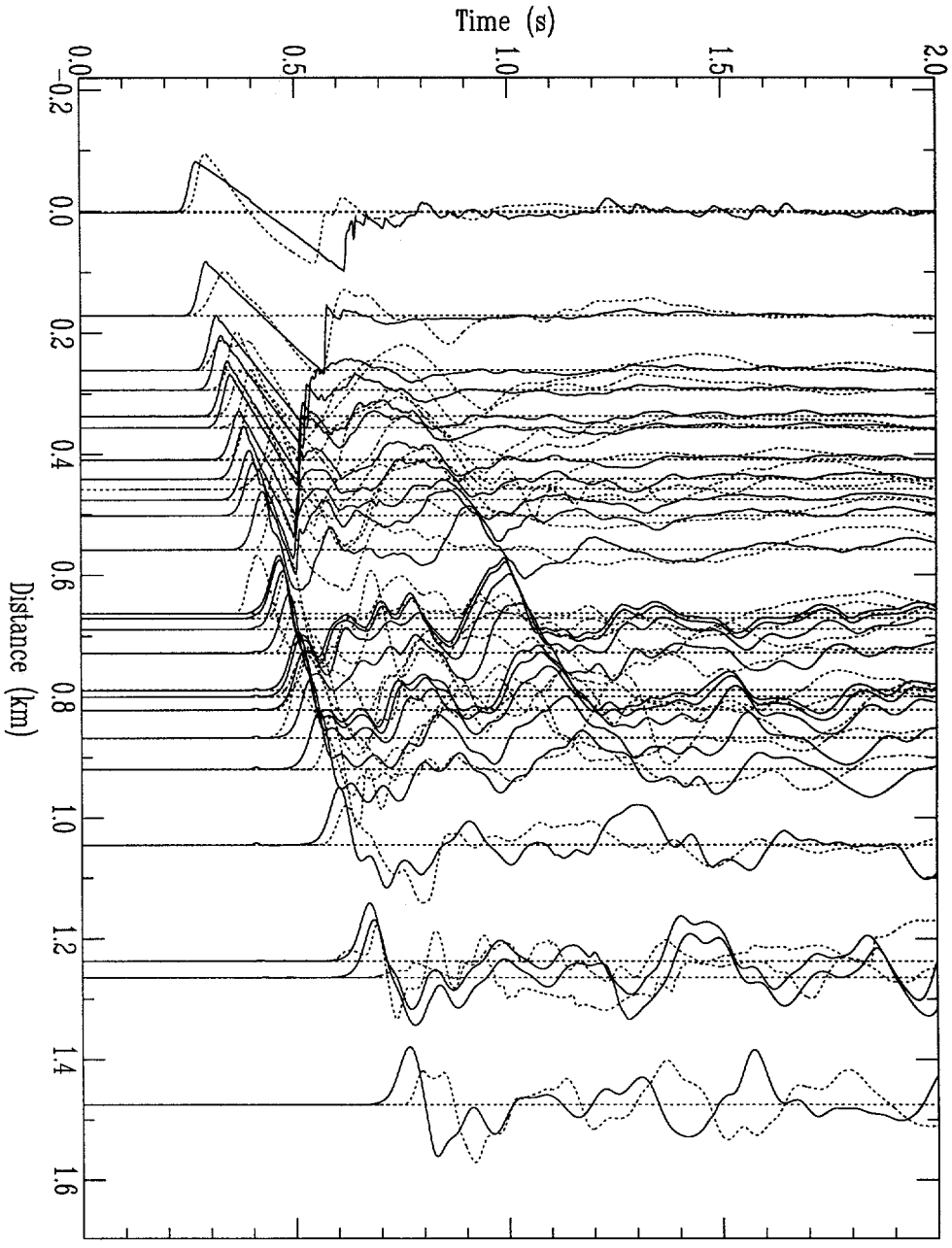

Figure 65: Record section plot of the normalized free-surface vertical velocity (m/s) vs. time (s) for the NPE. The solid lines denote the CE simulations and the dotted line represents the NPE data collected by LLNL [33] and LANL [34].

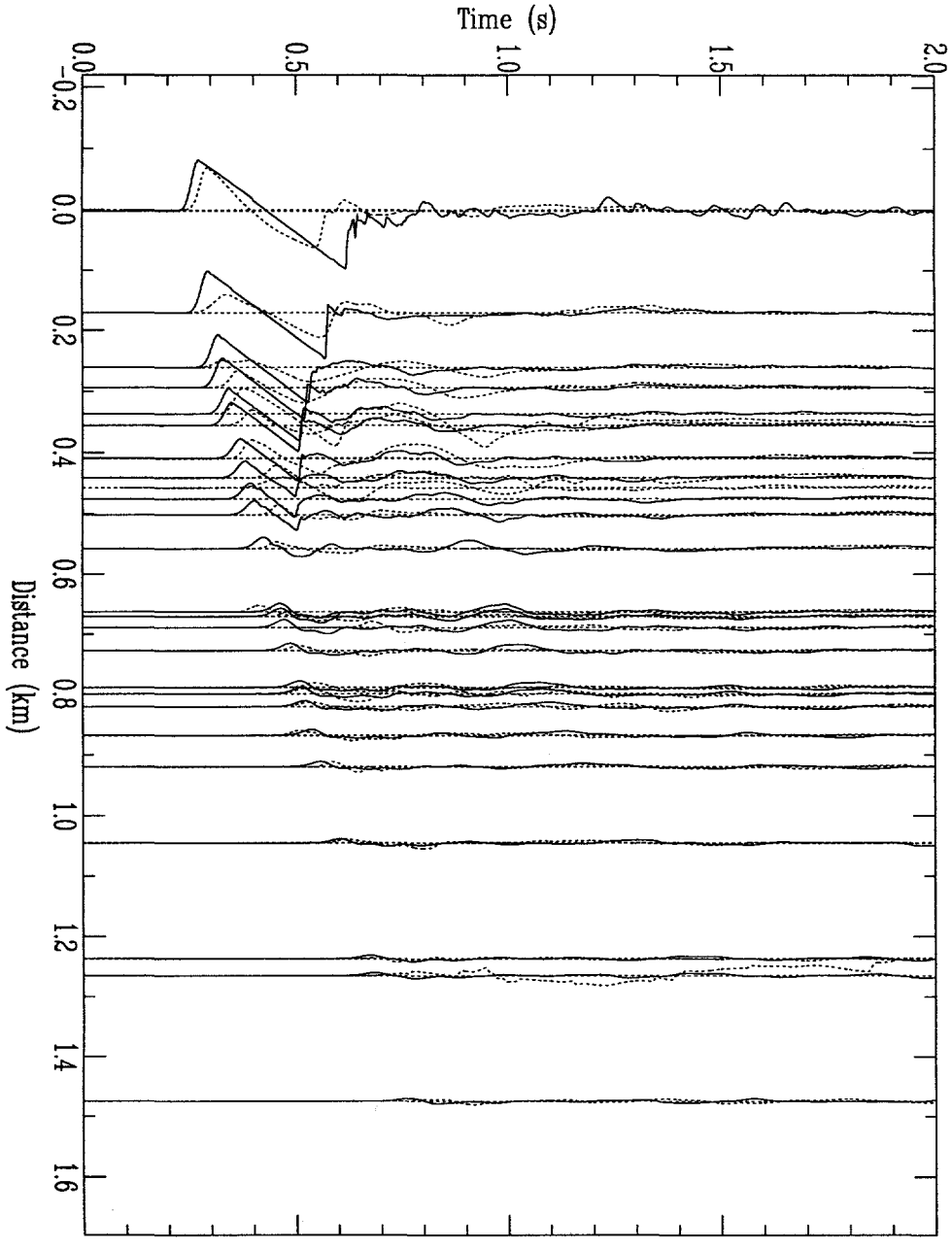

Figure 66: Record section plot of the unnormalized free-surface vertical velocity (m/s) vs. time (s) for the NPE. The solid lines denote the CE simulations and the dotted line represents the NPE data collected by LLNL [33] and LANL [34].

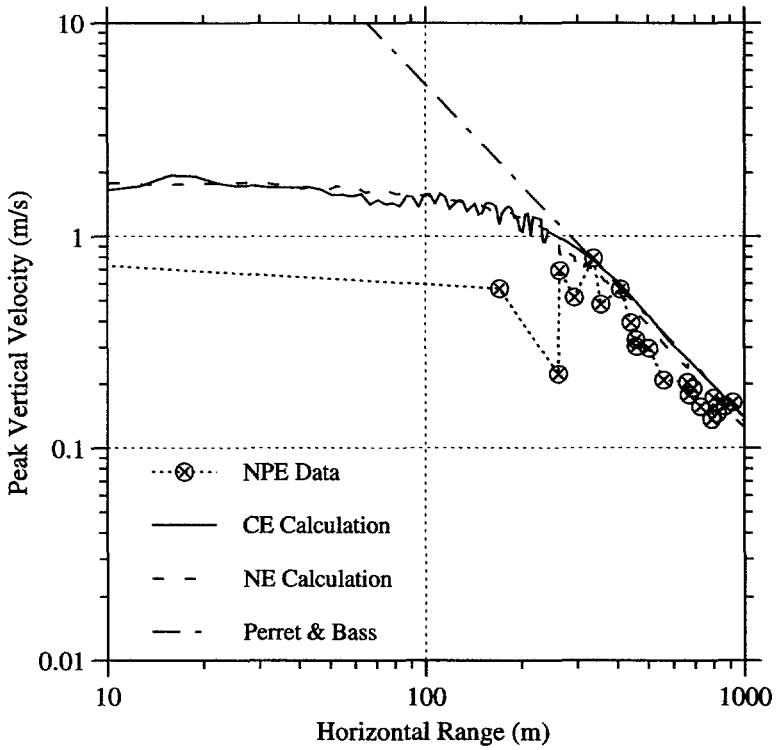

Figure 67: Peak free-surface vertical velocity (m/s) vs. horizontal range (m) from SGZ. The solid lines denote the CE simulation; the dashed lines represent the NE simulation; the ⊗ denotes LANL EES-3 [34] and LLNL values [33]; the dash-dot (– - –) line represents the Perret & Bass scaling relation [30] for wet tuff. This figure suggests that the scaled results provide reasonable estimates of the peak surface vertical velocity despite the fact that the Perret & Bass relations are based on free-field radial velocity data.

3.3 Chemical-Nuclear "Equivalence"

The relationship between underground chemical and nuclear explosions was a driving force behind the NPE. According to conventional wisdom, as observed in previous computational studies [3, 4], a single-point, tamped chemical explosion approximates a tamped nuclear source with about two times the yield of the chemical source; roughly speaking, "1 kt chemical $\approx$ 2 kt nuclear." In this section, we first compare some characteristics of tamped underground chemical and nuclear explosions, then consider other researchers' observations on this topic (both in general and for the NPE in particular), and finally discuss the implications of the present study.

An important element of this analysis is to examine if or how source differences affect the resulting computed waveforms for a given energy input. These factors are discussed, e.g., in [3, 4, 37, 38], and outlined below in Table 7. From the time scale of energy release, the signal associated with the more impulsive nuclear source contains relatively more high-frequency energy than the chemical source. Using the estimates [39] that vaporization occurs on unload from peak shock pressures of $\gtrsim$ 100 GPa for rock and $\gtrsim$ 10 GPa for water, vaporization and melt take place near a nuclear source but *not* in a chemical explosion. These processes act to dissipate a significant fraction of the high-frequency energy associated with the nuclear source. Additionally, inelastic processes in the surrounding geologic medium act to efficiently filter high frequency energy in both cases. The present calculations include modeling of the latter according to the material response models described in §2, as well as approximations of the former in the tuff EOS Sesame table used to simulate the very-early-time response to a nuclear source.

Glenn [37] discusses a theoretical mechanism relevant to this comparison. He shows that the value of the Grüneisen parameter (Γ) of the cavity gases (which are primarily detonation products for a chemical explosive, primarily vaporized

Selected Scales of Tamped Chemical and Nuclear Explosions

	Chemical	Nuclear
Energy density of explosive	$O(10^9$ J/m$^3)$	$O(10^{15}$ J/m$^3)$
Time scale of energy release	$O(1$ ms$)$	$O(1$ μs$)$
Maximum cavity pressure	$\sim$10 GPa	$O(100$ GPa$)$
Grüneisen parameter of cavity gases	$> \Gamma_{\text{nuclear}}$	$< \Gamma_{\text{chemical}}$
Heuristic "effective yield"	$\sim 2W_{\text{nuclear}}$	$\sim \frac{1}{2}W_{\text{chemical}}$

Table 7: Listed are order-of-magnitude estimates of the energy density, time scale of energy release, maximum cavity pressure, Grüneisen parameter, and heuristic "effective yield" for tamped chemical and nuclear explosions. The energy density cited for a nuclear source is only approximate; this quantity can vary by orders of magnitude from the value given. See, e.g., [3, 38, 40].

rock for a nuclear source) affects energy coupling and the final value of the RDP (i.e., ψ_∞). Specifically, the typically higher value of Γ for chemical explosive detonation products implies that the value of ψ_∞ for a chemical source will be greater than that for an equally energetic nuclear source. In the present simulations, the cavity gas response in the nuclear simulations is given by Sesame table data, while the expanded-state blasting agent behavior is dominated by the final term of the JWL EOS (see Eq. 5), viz., $P(V,E) \approx \omega E/V$, the sole parameter in which is $\omega \sim \rho_0 \Gamma$. We can estimate the value of Γ from the calculated values of pressure, density, and specific internal energy by assuming perfect gas behavior for the late-time cavity contents; we find that $\Gamma_{\rm NE} \sim 0.1$ while $\Gamma_{\rm CE} \sim 0.4$, values that are comparable to those cited by Glenn [37] for simulations of chemical and nuclear explosions in salt. It must be noted, however, that the expanded state behavior of chemical explosives detonation products is generally not well quantified; such unavoidable uncertainties in the modeling of the post-explosion (i.e., expanded state) cavity gas contribute directly to inaccuracies in the computed low-frequency material response. Despite this uncertainty, our result that $\psi_\infty^{\rm CE}/\psi_\infty^{\rm NE} \approx 1.25$ is qualitatively consistent with the trend suggested by Glenn.

Numerical simulations are equivocal on the subject of chemical-nuclear equivalency. Rimer *et al.* [2] performed a series of 1-D simulations of the NPE, using various source models as well as somewhat different values for the WP tuff properties. From these calculations, completed *before* the actual NPE shot, these authors conclude that "the [NPE] 1 kt HE source looks very much like a 1.5 kt nuclear source." That is, Rimer *et al.* claim the chemical-nuclear equivalency factor for the NPE is nominally 1.5 (this factor is somewhat higher for equivalency of peak stresses and peak displacements). Killian *et al.* [3] compare results of 1-D numerical simulations of a 1 kt *mass* TNT source and a 1 kt *energy* nuclear source in canonical wet or dry, weak or strong media. These researchers conclude that the free-field radial velocities induced by 0.8 kt (energy) TNT and 1 kt (energy) nuclear sources have a scaling factor of unity, i.e., are essentially identical, at ranges greater than two chemical source radii; they hedge the generality of this conclusion somewhat, however, with the observation the "differences [due to chemical and nuclear sources] are certainly not on the order of 2 but are at most 20% and are dependent on material." One caveat to this study is that only the early-time ($t_{\rm max} \sim 0.1$ s), near-source ($r_{\rm max} \sim 100$ m/kt$^{1/3}$) domain was considered. Burton *et al.* [4] consider the relationship of chemical and nuclear sources for cratering in saturated clay shale. These authors conclude from calculations that a "10-ton HE [nitromethane] event evidently provides about the same amount of kinetic energy to the medium as a nuclear event of twice the energy yield" and that "proper modeling of far-out seismic motion will be achieved through the use of the kinetic energy similitude criterion." That is, Burton *et al.* posit that the chemical-nuclear scaling factor is two, a conclusion that is born out in their 1-D free-field calculations (for scaled ranges of up to 250 m/kt$^{1/3}$) and 2-D numerical cratering simulations.

The results of our simulations fall between the findings of Rimer *et al.* and

Killian *et al.*, and do not support the conclusions of Burton *et al.*. For example, the free-field velocities we compute for equally energetic chemical and nuclear sources (Figs. 6-10 and 12-28) are effectively indistinguishable for times subsequent to the first arrival, although *peak* free-field radial velocity for the chemical source averages ~13% greater than that of the nuclear source at ranges greater than 20 m (see Fig. 36). The NPE WP tuff is similar to that used by Rimer *et al.*, not extremely dissimilar to the rock types considered by Killian *et al.*, yet may be quite different from the weak, saturated clay shale of the Burton *et al.* study. It is unclear whether the medium properties could affect the equivalency question so strongly (indeed, the Killian *et al.* study suggests this is not the case).

Experimental data for the NPE has also been compared with that of nearby nuclear events. Goldstein & Jarpe [29] compute scaled spectral amplitudes (i.e., RVP spectral amplitude divided by yield) using free-field data, and find that the scaled spectrum of the NPE is approximately a factor of two greater than that of "nearby nuclear explosions" at low scaled frequencies (i.e., $\tilde{f} \lesssim 1$ Hz·kt$^{1/3}$). Stump *et al.* [35] show that the mean spectral ratio of the nearby HUNTERS TROPHY event to the NPE, using all components of free-surface gages at ranges between 1 and 2 km, is approximately $0.96 \pm \left\{ {}^{0.46}_{0.23} \right\}$ for frequencies between 0.4 Hz and 1.0 Hz; the spectral ratio remains nearly flat at frequencies out to 10 Hz. Patton [28], using regional Rayleigh and Lg wave data as input to a seismogram-stacking technique, computes isotropic seismic moments from which he infers static RDP values; this procedure yields the ratio $\psi_\infty^{\mathrm{HT}}/\psi_\infty^{\mathrm{NPE}} \approx 1.4$.

To investigate the scaling aspect of chemical and nuclear sources, we performed one additional calculation using the identical geology but with a nuclear source of yield exactly twice that of the nuclear simulation heretofore discussed. Using computed velocity data at stations located between 300 m and 1100 m from the source, the zero-frequency RVP spectrum value for this case was calculated to be $\psi_\infty^{\mathrm{NE,2.1\ kt}} = 3340 \pm 450$ m^3. This value is ~2.1 times the value calculated for the 1.05 kt nuclear source simulation, and ~1.6 times the value computed for the 1.05 kt chemical source calculation (see Table 5). That is, we calculate that $\psi_\infty^{\mathrm{NE,2.1\ kt}}/\psi_\infty^{\mathrm{NPE}} \approx 1.6$.

The implication of these results on the chemical-nuclear equivalency problem for ψ_∞ is as follows. Our simulations of the NPE, which match the experimental waveforms in the free-field well imply an equivalency factor of 1.25, a value between that computed by others for hypothetical scenarios, and a value that we believe would would fall within the error budget of any experimental data analysis.

4 Conclusions

In this paper, we have considered 2-D simulations of the Non-Proliferation Experiment (NPE), an experiment in which 1.29×10^6 kg of ANFO-emulsion blasting agent (with the approximate energy equivalent of 1.1 kt) was detonated in NTS N-Tunnel tuff at a nominal depth of 389 m. In addition, we have performed numerical simulations of an equally energetic nuclear explosion in the identical (layered) geologic setting, and of an identical chemical source in a uniform geology. The main findings of this study are as follows.

- Comparisons of calculated waveforms for the NPE source with the experimental NPE data reveal:
  1. Free-field waveforms for the NPE simulation agree reasonably well with experimental data at ranges out to $\sim$1 km;
  2. Free-surface waveforms for the NPE simulation agree moderately well with experimental data at SGZ, and are in approximate qualitative agreement at greater ranges;
  3. To obtain this agreement, the working point material was assumed to be much weaker in shear than experimental data suggest.
- Comparisons of calculated waveforms for the NPE source with calculated waveforms for nuclear sources show:
  1. Peak waveform amplitudes for the chemical source are slightly ($\lesssim 10\%$) greater than those for the equally energetic nuclear source;
  2. Close-in ($r \lesssim 1$ km/kt$^{1/3}$) seismic source function parameters are essentially indistinguishable between equally energetic chemical and nuclear sources, with the exception of the seismic moment, which is $\sim$25% greater for the chemical source.
- Comparisons of calculated waveforms for the NPE source in layered geology with waveforms calculated in the uniform WP medium indicate:
  1. Peak radial amplitudes are slightly greater for the uniform medium than for the layered geology, but radial and vertical waveforms of the latter exhibit much more layering-induced structure out to late time;
  2. Close-in ($r \lesssim 1$ km/kt$^{1/3}$) seismic source function parameters are similar for both layered and uniform geologies, with the exception of the RVP spectrum overshoot, which is significantly greater for the layered geology.

This study leaves unanswered the question of *why* the chemical-nuclear equivalence factor is found to vary between the values of one and two, as discussed in §3.3, with this study suggesting a factor of 1.25. The calculations we

have presented match the data well for the chemical explosive, and use proven techniques for the nuclear source simulations; consequently, we place credence in the equivalency they imply. Futhermore, there is nontrivial disparity in seismic source function properties obtained from the experimental NPE data by various researchers; those results would imply attendant variation in equivalency factors. Hence, we strongly suspect that our results would fall within the error budget incurred in experimental data analyses.

Based on the above observations, we conclude that monolithic, tamped chemical and nuclear sources are functionally indistinguishable. We further posit that there is no single chemical-nuclear equivalence factor; rather, this value varies between one and two, depending upon the property being compared (e.g., ψ_∞ vs. peak velocity), emplacement medium (e.g., dry tuff vs. wet clay vs. granite), chemical source (e.g., ANFO vs. C-4), as well as the experimental data being compared and the techniques by which those data are analyzed.

In this study we have concentrated on near-source phenomena related to the NPE; further analysis of other aspects of this experiment are warranted. It would be of interest to continue the present calculations to later times (to investigate low-frequency phenomena) and greater distances (to compare, both directly and statistically, with more distant experimental stations). Comparison of the computed results and the experimental NPE data presented herein with data and simulations of nearby nuclear events could lead to increased understanding of the relationship between similar-scale chemical and nuclear explosions. Additionally, computed waveforms could be propagated out to regional distances, by, e.g., the methods discussed by Taylor & App [41]; those results could be compared with regional seismic data from nearby events. Better understanding of scale effects may develop from analysis of simulations of the NPE calibration shot, which was a small high explosive charge (300 lb C-4) detonated at the NPE working point several months prior to the NPE. Clearly, the NPE provides a wealth of information about explosion phenomenology; the full value of this experiment remains to be realized.

Acknowledgments

The authors thank C. W. Smith (SNLA), H. D. Garbin (SNLA), P. Goldstein (LLNL), K. H. Olsen (LANL), A. L. Peratt (LANL), D. C. Pearson (LANL), B. W. Stump (LANL) and their colleagues for kindly sharing their data. The authors also express their gratitude to F. N. App (LANL) and T. N. Dey (LANL) for many helpful and illuminating technical discussions. The constructive reviews by F. N. App and S. R. Taylor are gratefully acknowledged, as are the editorial comments of F. Harp.

References

[1] M. D. Denny, ed., *Proceedings of the Symposium on the Non-Proliferation Experiment: Results and Implications for Test Ban Treaties, April 19–21, Rockville, MD*, Lawrence Livermore National Laboratory Report CONF-9404100 (1994).

[2] N. Rimer, W. Proffer, E. Halda & R. Nilson, *Containment Related Phenomenology from Chemical Kiloton*, Defense Nuclear Agency Technical Report DNA-TR-94-21 (1994).

[3] B. G. Killian, J. R. Rocco & E. J. Rinehart, *Comparisons of Nuclear-TNT Equivalencies and Effects Environments in Different Geologic Media*, Defense Nuclear Agency Technical Report DNA-TR-87-152 (1987).

[4] D. E. Burton, C. M. Snell & J. B. Bryon, Computer Design of High-Explosive Experiments to Simulate Subsurface Nuclear Detonations, *Nuclear Technology* **26**, pp. 6587 (1975).

[5] T. N. Dey & J. R. Kamm, *User's Guide to SMC-123*, Los Alamos National Laboratory, unpublished report (1994).

[6] M. J. Baldwin, R. P. Bradford, S. P. Hopkins, D. R. Townsend & B. L. Harris-West, Geology, Geophysics, and Physical Properties of the U12n.25 Non-Proliferation Experiment Site, in *Proceedings of the Symposium on the Non-Proliferation Experiment: Results and Implications for Test Ban Treaties, April 19–21, Rockville, MD*, ed. M. D. Denny., Lawrence Livermore National Laboratory Report CONF-9404100 (1994).

[7] F. N. App & W. M. Brunish, *Stress Wave Calculations of Four Selected Underground Nuclear Tests: MERLIN, HEARTS, PRESIDIO, MISTY ECHO*, Los Alamos National Laboratory Internal Report EES-NTC-91-03 (1991).

[8] F. N. App, W. M. Brunish & C. L. Edwards, Modelling of the HEARTS Event, in *Proceedings of the Fifth Symposium on Containment of Underground Nuclear Explosions*, C. A. Olsen & J. A. Carter, eds., Lawrence Livermore National Laboratory Report CONF-8909163 (1989).

[9] T. R. Butkovich, *A Technique for Generating Pressure-Volume Relationships and Failure Envelopes for Rocks*, Lawrence Livermore National Laboratory Report UCRL-51441 (1973).

[10] J. Abdallah, Jr., G. I. Kerley, B. I. Bennett, J. D. Johnson, R. C. Albers & W. F. Huebner, *HYDSES: A Subroutine Package for Using Sesame in Hydrodynamic Codes*, Los Alamos National Laboratory Report LA-8209, Los Alamos, NM (1980).

[11] P. C. Souers, D. B. Larson & C. M. Carver, Performance Calculations on the ANFO Explosive RX-HD, in *Proceedings of the Symposium on the Non-Proliferation Experiment: Results and Implications for Test Ban Treaties, April 19–21, Rockville, MD*, ed. M. D. Denny., Lawrence Livermore National Laboratory Report CONF-9404100. (1994).

[12] E. L. Lee, H. C. Hornig & J. W. Kury, *Adiabatic Expansion of High Explosive Detonation Products*, Lawrence Livermore National Laboratory Report UCRL-50422 (1968).

[13] J. D. Johnson, Los Alamos National Laboratory, personal communication.

[14] T. O. McKown, *Explosive Performance on the Non-Proliferation Experiment*, Los Alamos National Laboratory Report LA-12748-MS (1994).

[15] T. R. Butkovich, *Rock Melt from an Underground Nuclear Explosion*, Lawrence Livermore National Laboratory Report UCRL-51554 (1974).

[16] F. N. App & T. W. Tunnell, *User Manual for the NTS Ground Motion Data Base Retrieval Program ntsgm*, Los Alamos National Laboratory Report LA-UR-94-1538 (1994).

[17] B. L. Wright, K. R. Alrick & J. N. Fritz, *Axisymmetric Magnetic Gauges*, Los Alamos National Laboratory Report LA-UR-94-1191 (1994).

[18] C. W. Smith, NPE – Close-In Stress and Motion Measurements, in *Proceedings of the Symposium on the Non-Proliferation Experiment: Results and Implications for Test Ban Treaties, April 19–21, Rockville, MD*, ed. M. D. Denny., Lawrence Livermore National Laboratory Report CONF-9404100 (1995).

[19] C. W. Smith, Sandia National Laboratory, personal communication (1994).

[20] D. Patch, Science Applications International Corp., personal communication (1994).

[21] A. L. Peratt & K. H. Olsen, *Tri-Axial Free-Field Accelerometer Measurements for the Non-Proliferation Experiment, HUNTERS TROPHY, MINERAL QUARRY, and MISTY ECHO events at NTS*, Los Alamos National Laboratory Report LA-UR-95-700 (1995).

[22] H. D. Garbin, Free-Field Seismic Ground Motion on the Non-Proliferation Experiment, in *Proceedings of the Symposium on the Non-Proliferation Experiment: Results and Implications for Test Ban Treaties, April 19–21, Rockville, MD*, ed. M. D. Denny., Lawrence Livermore National Laboratory Report CONF-9404100 (1994).

[23] K. H. Olsen & A. L. Peratt, Free-Field Ground Motions for the Nonproliferation Experiment: Preliminary Comparisons with Nearby Nuclear Events, in *Proceedings of the Symposium on the Non-Proliferation Experiment: Results and Implications for Test Ban Treaties, April 19–21, Rockville, MD*, ed. M. D. Denny., Lawrence Livermore National Laboratory Report CONF-9404100 (1994).

[24] M. D. Denny & L. R. Johnson, The Explosion Seismic Source Function: Models and Scaling Laws Reviewed, in *Explosion Source Phenomenology*, eds. S. R. Taylor, H. J. Patton & P. G. Richards, Geophysical Monograph 65, Americal Geophysical Union, Washington, DC (1991).

[25] F. N. App, *Sensitivity of the Close-In Seismic Source Function to Rock Properties*, Los Alamos National Laboratory Report LA-UR-93-1884 (1993).

[26] J. T. Cherry, N. Rimer & W. O. Wray, *Seismic Coupling from a Nuclear Explosion: The Dependence of the Reduced Displacement Potential on the Nonlinear Behavior of the Near Source Rock Environment*, Systems, Science and Software Technical Report SSS-R-76-7242 (1975).

[27] E. M. Jones, Los Alamos National Laboratory, personal communication (1995).

[28] H. J. Patton, Investigations of the Low Frequency Seismic Waves Recorded at Near-Regional Distances from the Non-Proliferation Experiment, in *Proceedings of the Symposium on the Non-Proliferation Experiment: Results and Implications for Test Ban Treaties, April 19–21, Rockville, MD*, ed. M. D. Denny., Lawrence Livermore National Laboratory Report CONF-9404100 (1994).

[29] P. Goldstein & S. P. Jarpe, Comparison of Chemical and Nuclear Explosion Source Spectra from Close-in, Local, and Regional Seismic Data, in *Proceedings of the Symposium on the Non-Proliferation Experiment: Results and Implications for Test Ban Treaties, April 19–21, Rockville, MD*, ed. M. D. Denny., Lawrence Livermore National Laboratory Report CONF-9404100 (1994).

[30] W. R. Perret & R. C. Bass, *Free-Field Ground Motion Induced by Underground Explosions*, Sandia Laboratories Report SAND 74-0252 (1975).

[31] J. R. Murphy, Free-Field Seismic Observations from Underground Nuclear Explosions, in *Explosion Source Phenomenology*, eds. S. R. Taylor, H. J. Patton & P. G. Richards, Geophysical Monograph 65, Americal Geophysical Union, Washington, DC (1991).

[32] U.S. Congress, Office of Technology Assessment, *The Containment of Underground Nuclear Explosions*, OTA-ISC-414, Washington, DC, U.S. Government Printing Office (1989).

[33] P. Goldstein, Lawrence Livermore National Laboratory, personal communication (1994).

[34] B. W. Stump & D. C. Pearson, Los Alamos National Laboratory, personal communication (1994).

[35] B. W. Stump, D. C. Pearson & R. E. Reinke, *Source Comparisons Between Nuclear and Chemical Explosions Detonated at Rainier Mesa, Nevada Test Site*, Los Alamos National Laboratory Report LA-UR-94-4073 (1994).

[36] E. M. Jones, F. N. App & R. W. Whitaker, *Ground Motions and the Infrasound Signal: A New Model and the Discovery of a Significant Cavity Rebound Signal*, Los Alamos National Laboratory Report LA-UR-93-861 (1993).

[37] L. A. Glenn, *Differences in Coupling Between Chemical and Nuclear Explosions*, Lawrence Livermore National Laboratory Report UCRL-JC-109448 (1992).

[38] L. A. Glenn, Modeling the Explosion-Source Region: An Overview, in *Proceedings of the Numerical Modeling for Underground Nuclear Test Monitoring Symposium*, eds. S. R. Taylor & J. R. Kamm, Los Alamos National Laboratory Report LA-UR-93-3839 (1993).

[39] T. R. Butkovich, B. Moran & D. E. Burton, *A Model for Calculating Shock Loading and Release Paths for Multicomponent Geologic Media*, Lawrence Livermore National Laboratory Report UCRL-53178 (1981).

[40] S. Glasstone & P. J. Dolan, *The Effects of Nuclear Weapons*, U.S. Government Printing Office (1977).

[41] S. R. Taylor & F. N. App, *Representation Theorem Coupling of Numerical and Wave Propagation Codes for the Generation of Synthetic Seismograms*, Los Alamos National Laboratory Report LA-UR-94-2194 (1994).

* U.S. GOVERNMENT PRINTING OFFICE 1995-673-029/7090